UNIVERSITY OF CALIFORNIA,
IRVINE

Spatio-Temporal Structured Laser Fields and Enabling Technology for Next Generation Ultrahigh-Intensity Lasers

DISSERTATION

submitted in partial satisfaction of the requirements
for the degree of

DOCTOR OF PHILOSOPHY

in Physics

by

Kyle Daane Chesnut

Dissertation Committee:
Professor C.P.J. Barty, Chair
Professor Franklin Dollar
Professor Howard Lee

2024

DEDICATION

To my parents for their endless support, without which this would not have been possible,
to my brother and sister for their constant companionship,
to my friends for the continuous motivation.

In memory of Eric Alexiev, a true scholar of life.

TABLE OF CONTENTS

LIST OF FIGURES

LIST OF TABLES

ACKNOWLEDGMENTS

Firstly, I would like to thank my advisor, Prof. C. P. J. Barty, for the mentorship and support during my time as a Ph.D. student at UC Irvine. Beyond laser science and research, I have learned a great deal from him on entrepreneurship, how to effectively communicate my ideas to others, and, perhaps most importantly, on how to tackle problems with a solution oriented mindset. If the Barty Group has a mantra it is surely "It's not a problem it's a feature."

I would also like to thank every single group member in the Barty Lab for the countless hours of discussion, idea spitballing, and comradery during my time here. In particular I would like to thank Eric Nelson who suffered along my side as we built a modelocked Ti:sapphire oscillator.

Permission has been grated to include previously published work in this thesis from the journal Optical Express. This permission is granted to the author on the Copyright Transfer and Licensing Information page of the Optics Express website.

VITA

Kyle Daane Chesnut

EDUCATION

Doctor of Philosophy in Physics **2024**
University of California - Irvine *Irvine, California*

Master of Science in Applied Physics **2017**
University of Oregon *Eugene, Oregon*

Bachelor of Science in Engineering Physics **2012**
University of California - Berkeley *Berkeley, California*

RESEARCH EXPERIENCE

Graduate Research Associate **2018–2024**
University of California, Irvine *Irvine, California*

Graduate Intern **2017–2018**
Lawrence Livermore National Lab *Livermore, California*

R&D Engineering Intern **2017**
nLight *Vancouver, Washington*

Graduate Research Assistant **2016**
University of Oregon *Eugene, Oregon*

Undergraduate Research Assistant **2010–2011**
University of California, Berkeley *Berkeley, California*

TEACHING EXPERIENCE

Teaching Assistant **2018**
University of California, Irvine *Irvine, California*

REFEREED JOURNAL PUBLICATIONS

Entirely reflective slit spatial filter for high energy laser systems **2019**
Optics Express

Ideal spatio-temporal pulse distribution for exawatt-scale lasers based on simultaneous chirped beam and chirped pulse amplification **2023**
Optics Express

Method for producing identical spectral copies of ultra-broadband arbitrary light fields **2024**
Optics Express

Analysis of an exawatt-class laser architecture based on chirp pulse juxtaposed with beam amplification **2024**
In Submission

REFEREED CONFERENCE PUBLICATIONS

Analysis of Chirped Pulse Juxtaposed with Beam Amplification (CPJBA): A Nd:Glass Laser Architecture for Exawatt-class Peak-Power Pulses **Jan 2022**
High Intensity Lasers and High Field Phenomena

Spatially and Temporally Chirped Beams: The Single Aperture Path to Exawatt Peak-Power Lasers **Jan 2023**
Ultrafast Optics

Amplitude Neutral Temporal Electric-field Autocorrelator with Exquisite Resolution (ANTEATER) **Jan 2023**
Ultrafast Optics

ABSTRACT OF THE DISSERTATION

Spatio-Temporal Structured Laser Fields and Enabling Technology for Next Generation Ultrahigh-Intensity Lasers

By

Kyle Daane Chesnut

Doctor of Philosophy in Physics

University of California, Irvine, 2024

Professor C.P.J. Barty, Chair

This dissertation seeks to show that the spatio-temporal couplings of ultrafast lasers can be exploited to bypass the current technology bottlenecks on achieving next-generation ultrahigh-intensity lasers. First, the design of a novel six-grating compressor is presented and analyzed with a ray-tracing code and custom post-processing software, where the use of chirped-beam grating pairs was found to increase group delay dispersion (GDD) removal over 425% greater than a traditional grating pair. The higher-order dispersion effects, that come from using high-dispersion gratings with a large induced GDD, on the temporally stretched pulse were examined with strategies proposed on how to mitigate them. A custom 2D amplification code was used to model the amplification of a spatially and temporally chirped beam-pulse in a large-aperture, Nd:glass amplifier that are commonly used as high-energy inertial confinement fusion lasers. Unique pulse distortion effects from this novel amplification scheme were uncovered, leading to a design strategy based on 2D sculpting of the spatio-temporal input pulse and shaping of the transverse gain profile in the amplifier. With these, a 40-J, 20-ns chirped beam pulse with a 2x spatial chirp, and spectral bandwidth capable of supporting a 100-fs compressed pulse duration, was shown to be amplified to excess of 25-kJ with a B-integral less than 5. This would enable the creation of an exawatt-class laser system. A novel stretcher design capable of producing a 20-ns stretched pulse and a

multi-beam focusing arrangement based on a multi-segment tiled parabolic mirror are presented with a performance analysis, along with other technology advancements useful for ultrahigh-intensity laser systems.

Chapter 1

Introduction

"A laser is a solution seeking a problem."

-Dr. Theodore Maiman

In 1960 the invention of the laser [1], with its rapid advancement in peak-power to gigawatt levels following the discovery of Q-switching [2] and mode-locking [3, 4, 5, 6], unlocked sufficient electric field strengths to observe nonlinear optics [7] and multiphoton physics [8]. Over two decades later, chirped pulse amplification (CPA) [9] allowed high-peak-power lasers to break through to the multi-terawatt regime [10, 11] with focused intensities exceeding 10^{15} W/cm^2. At these intensities, the laser field strength exceeds the electron binding energy enabling a host of new laser-plasma applications [12, 13, 14]. Since the creation of the Nova PW laser in 1999 [15], ultra-high intensity laser systems based on CPA technology have grown in both number [16] and peak-power with several multi-petawatt facilities already operating [17, 18, 19, 20]. In 2021, CoReLs in South Korea, a 4-PW Ti:Sapphire laser, achieved the new world record intensity of 10^{23} W/cm^2 opening the door to new experiments in strong field quantum electrodynamics (SF-QED) [21]. Recently, the Multi-Petawatt Physics Prioritization Workshop determined that the next generation of SF-QED experiments, laser-driven

nuclear reactions, and advanced photon and particle sources require lasers with peak-power on the order of hundreds of petawatts and focused intensity greater than 10^{24} W/cm^2 [22]. Laser facilities are currently operating in the 10-PW peak-power class, ELI-NP-HLPS in Romania has demonstrated 10-PW [17] and SULF in China has the necessary power and bandwidth [23], along with several currently under construction [24, 25, 26, 27]. The extension of CPA-based, high-peak-power lasers to exawatt-class, however, presents significant technological hurdles.

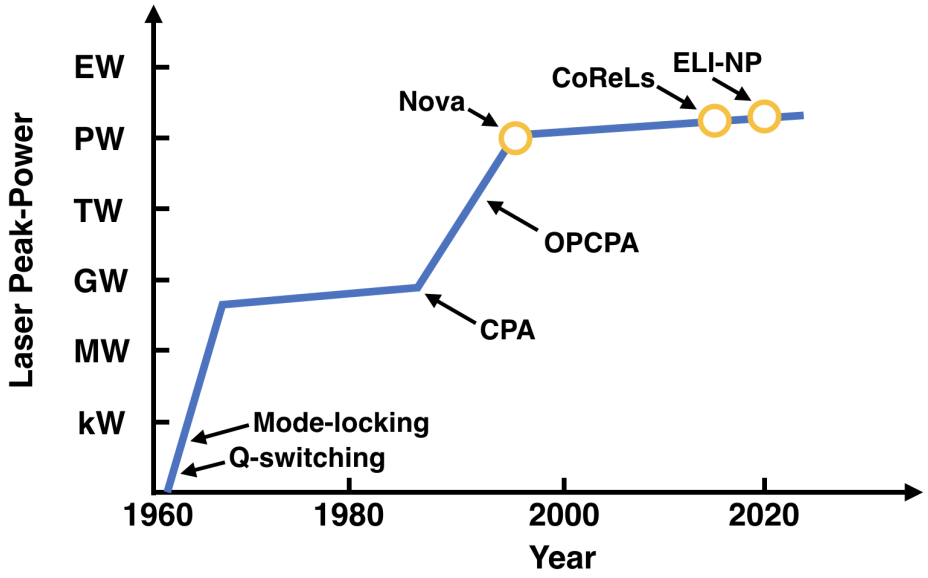

Figure 1.1: Trendline of highest achieved laser peak-power over time. Advents of new laser techniques allow for an initial rapid increase in laser peak-power followed by a period of more moderate increase as the technology matures. Figure recreated from [28].

CPA mitigates optical damage due to small-scale, self-focusing in a laser amplifier by temporally stretching the pulse prior to amplification, which lowers the pulse intensity in the gain media thereby decreasing the B-integral accumulation (a metric of nonlinear phase accumulation related to pulse intensity). This has enabled laser peak-power to increase by several orders-of-magnitude but effectively pushed the damage problem from the amplifier and onto the final optics. In particular, the final compressor grating, and all downstream optics, where the pulse duration is the shortest and intensity the highest become the limiting components for high-peak-power operation. For damage mechanisms in the femtosecond

regime, if these optics are operated at above $\sim 10^{13}$ W/cm^2, the field strength of the laser will exceed the binding potential of electrons in the optic and the optic will be damaged. This damage mechanism presents a hard limit on pulse intensity within the laser system. To further increase peak-power beyond current state-of-art, the pulse intensity on the final optics must be reduced by increasing the beam aperture either directly, with beam expansion and larger optics, or indirectly, by coherently combining multiple beam apertures. Thus, most designs for new laser systems that can go beyond the current 10-PW limit center via one of four schemes: (i) multiple amplifier beamlines that are coherently beam combined (CBC) post-compression [29, 30], (ii) a single exawatt-class amplifier beamline that is compressed by a large, tiled grating assembly [31, 32], (iii) a single exawatt-class amplifier beamline that is compressed with plasma optics [33], and (iv) a single exawatt-class amplifier beamline that is split into multiple identical beamlets prior to final compression [34, 35]. It is the peak-focused-intensity, rather than peak-power, that enables novel laser applications and the discovery of new science. CoReLs, while not the highest peak-power laser, was able to achieve record intensity through careful management of wavefront errors on their 4-PW beamline to minimize the focal spot area [21]. Extending this to multiple, individual amplifier beamlines that are coherently combined is very challenging. Each amplifier will have a different prompt wavefront distortion shot-to-shot, ultimately limiting the maximum focused intensity achievable. In the tiled grating compressor scheme, the void between gratings imparts a mosaic error onto the near-field of the beam that negatively affects the focal spot distribution lowering the intensity [36, 37, 38]. Furthermore, each tiled grating has five degrees-of-freedom that must be aligned with nanometer level precision for the gratings to be coherently tiled together [38, 39]. This becomes prohibitively expensive and complicated as the laser scales in size.

To achieve the highest-intensity possible with a fixed laser power, it is desirable to have a single, exawatt-class amplifier beamline split into multiple identical beamlets that are compressed separately. There are amplifier architectures capable of this, though they are

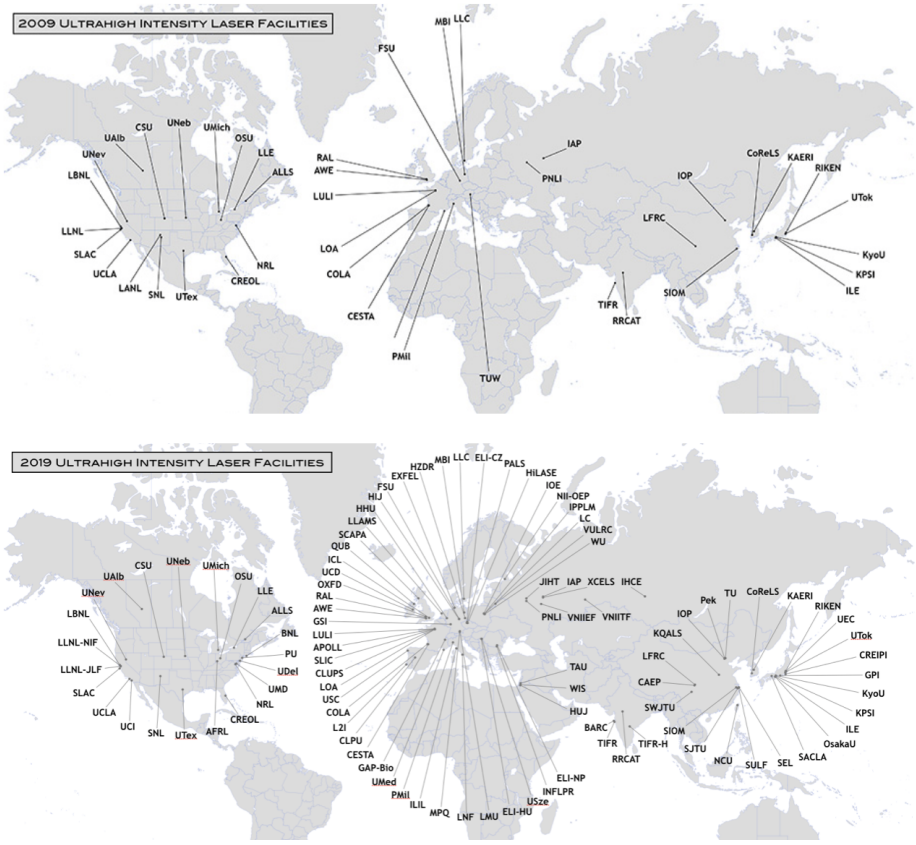

Figure 1.2: World map of ultrahigh intensity laser facilities from (top) 2009 and (bottom) 2020 [16].

few. Ti:Sapphire amplifiers are limited in energy by the maximum crystal size possible and parasitic amplified spontaneous emission (ASE) [40, 41, 42]; barring new techniques to drastically reduce the pulse duration in these systems, it is unlikely a single Ti:Sapphire amplifier will produce greater than 10 PW. Recently, Y. Liu et al. presented a method to tile four Ti:sapphire amplifiers together in a 2x2 array seeded from a common front end to scale beyond 10-PW to 40-PW [43]. While this showed improvements over CBC, there are challenges in scaling further to the exawatt-class. In 2021, Z. Li et al. published a scheme called wide-angle non-collinear optical parametric chirped-pulse amplification (WNOPCPA) that could potentially produce a ∼0.12-EW beamline prior to thin-plate post-compression and ∼0.59-EW with thin-plate post-compression [44]. However, this scheme does not have a design for the compressor system and is predicated on a multi-kJ pump laser as well as

meter-scale chirped mirrors.

Large-aperture, Nd:glass lasers, leveraging decades of research and implementation as the highest energy laser systems produced [45, 46, 47, 48], are a prime candidate for a single amplifier exawatt-class beamline. They continue to be used as the platform for new high-intensity lasers when high-energy is desired [24, 49] with further progress allowing for repetition rates up to 10-Hz [50]. One can safely extract ∼25-kJ from a single amplifier of the National Ignition Facility (NIF) laser if the amplified pulse is stretched to greater than 20-ns [51]. It has been shown that a large aperture Nd:Glass amplifier, composed of mixed silicate- and phosphate-glass amplifier slabs, when combined with an appropriate front end based on a Ti:Sapphire seed laser and OPCPA pre-amplifier can support the amplified bandwidth necessary to produce 100-fs Fourier transform limited (FTL) pulses [52]. This has the potential to be a single amplifier beamline capable of producing 0.2-EW pulses. If this were to be done in a typical CPA setup using a four-grating Tracey compressor [53] with the existing Advanced Radiographic Capability (ARC) laser grating design [54], gratings two and three would require a width of 6 meters for sufficient optical path length difference between the red and blue components to temporally recompress the pulse. These gratings are estimated to have a damage threshold of approximately 1-J/cm2 when scaled to 100-fs pulse durations [55, 56], to drop the fluence below this value requires expanding the beam and grating height to ∼5.5 meters. The production of 6-m x 5.5-m gratings is well beyond the capabilities of any existing, large-scale grating fabrication system.

Chirped pulse juxtaposed with beam amplification (CPJBA), patented in 2004 [34] and first presented at the International Committee on Ultra-High Intensity Lasers Conference 2014, is a technique to produce an ultrahigh intensity laser by extracting the full energy from a high saturation fluence laser system using a highly stretched chirped beam-pulse and recompressing with a six-grating compressor system. To avoid final optic damage the pulse is split into 36 copies using a dispersion and amplitude-balanced splitting arrangement prior

to total compression by the final grating pair of the six-grating compressor. This distributes the pulse over many grating pairs producing multiple identical beamlets at the output, which inherently allows a variety of multi-beam focusing arrangements such as dipole focusing [57] and other multi-beam applications [58]. When applied to a single NIF-like beam line this system is expected to produce an exawatt-class peak-power laser, which we will refer to as the Nexawatt [35]. All the fundamental components of the Nexawatt are based on existing technology that have been implemented in current high-intensity lasers and large-scale optical systems. However, this novel laser architecture does present unique challenges, they are the following:

- Seed Pulse Generation - Creation of a 20-ns stretched, chirped-beam, seed pulse.
- Chirped Beam Amplification - Management of the pulse distortions that occur during amplification due to the unique chirped beam-pulse structure.
- Long-duration Pulse Compression – Compression of the 20-ns stretched pulse to its 100-fs FTL using gratings based on existing technology.
- Management of Final Optics Damage – Generation of identical, lower-peak-power beams prior to final pulse compression.
- Multi-beamlet Focusing - Focusing and phasing of multiple, identical output beams.

This dissertation presents the design and simulation of the various sub-systems required to create, amplify, compress, and, finally, focus the chirped beam-pulse. This architecture potentially enables the production of an 0.2-EW peak power laser pulses and subsequent focused intensities of 10^{25} W/cm^2, or two orders-of-magnitude beyond the current record.

Chapter 2 provides a cursory overview of the background material needed to understand the theory of ultrahigh-intensity lasers and the basics of CPA. The basis of CPJBA as a long-duration pulse compression scheme for ultrahigh-intensity lasers and its solution to the

current peak-power bottleneck in CPA lasers is discussed in Chapter 3. This includes the theory of a chirped beam-pulse grating pair and an analysis of the six-grating compressor for CPJBA. In Chapter 4, chirped beam amplification is addressed. First, the energetics modeling code, based on a discretized Frantz-Nodvik solution, is discussed showing how it has been expanded to model the amplification of arbitrary spatio-temporal pulse shapes. It is then applied to the primary amplifier of the Nexawatt system to demonstrate the unique spatio-temporal and spatio-spectral distortions that arise from amplifying a simultaneously spatially and temporally chirped beam. Finally, a method of modeling the reverse amplification of a pulse is described. This produces the ideal sculpted spatio-temporal input pulse and initial spatial distribution of stored energy in the amplifier slabs that will give the desired amplified 25-kJ spatio-temporal output pulse. Techniques for 2D pulse sculpting to achieve the ideal input spatio-temporal pulse are discussed. Chapter 5 covers the design and modeling of various sub-systems required for the full Nexawatt laser system. The design of a novel multi-pass regenerative stretcher, capable of producing stretched pulses greater than 20-ns with moderate size gratings and optics, is discussed in detail. The details and error analysis of a segmented parabolic focusing mirror, similar to those used on large-aperture telescopes [59], is shown to coherently phase together the identical beamlets in a manner that would produce a focused intensity exceeding 10^{25} W/cm^2. Design of a novel ultra-broadband beam splitter arrangement is presented in the context of being used in a Michelson interferometer setup to produce a non-distorted, 2D measurement of the spatio-spectral pulse via Fourier transform spectroscopy. Accurate knowledge of the spatio-spectral pulse distribution is critical for chirped beam amplification. The conclusion, Chapter 6, reviews the advantages of the CPJBA for exawatt-class peak-power lasers and discusses further applications of this laser architecture.

Chapter 2

Background

2.1 Electromagnetic Radiation

The nature of light has been a question that captivated early physics for centuries. The theory of light as a wave was first introduced by Dutch physicist Christiaan Huygens in 1678, and later expand most prominently by Augustin-Jean Fresnel in the early 1800's who described light as a transverse wave propagating in a medium. Later, in 1845, Michael Faraday's experiments showing that a magnetic field applied to linearly polarized light propagating through a dielectric medium could rotate the angle of polarization suggested that light was a form of electromagnetic radiation. This led to the work of James Clerk Maxwell, who in the 1860's synthesized the various laws of electromagnetism, formed over decades of experimental and theoretical work by various scientists, into a coherent mathematical formalism.

The textbook *Lasers* by A.E. Siegman [60] was used to prepare this section.

2.1.1 Maxwell's Equations

Maxwell's equations define a mathematical relationship between the electric field $\mathbf{E}$ and magnetic field $\mathbf{B}$,

$$\nabla \cdot \mathbf{E} = \frac{\rho}{\epsilon_0} \tag{2.1}$$

$$\nabla \cdot \mathbf{B} = 0 \tag{2.2}$$

$$\nabla \times \mathbf{E} = -\frac{\partial \mathbf{B}}{\partial t} \tag{2.3}$$

$$\nabla \times \mathbf{B} = \mu_0 \left(\mathbf{J} + \epsilon_0 \frac{\partial \mathbf{E}}{\partial t} \right) \tag{2.4}$$

Where ρ is the electric charge density, ϵ_0 is the vacuum permittivity, μ_0 is the vacuum permeability, and $\mathbf{J}$ is the current density. Bold faced variables represent vector quantities. When light propagates through a dielectric medium these relationships are modified.

2.1.2 Electromagnetic wave equation

The wave equation, ubiquitous in physics, is a second-order partial differential equation to describe the movement of waves in a medium. For light propagating in a linear, source-free, homogeneous material (i.e. $\mathbf{J} = 0$ and $\rho = 0$), the electromagnetic wave equation can be found by applying the curl of the curl to (2.3) and (2.4) and using a vector identity,

$$\nabla \times \nabla \times \mathbf{E} = \nabla(\nabla \cdot \mathbf{E}) - \nabla^2 \mathbf{E} = \nabla \times \left(-\frac{\partial \mathbf{B}}{\partial t} \right) = -\frac{\partial}{\partial t}(\nabla \times \mathbf{B}) \tag{2.5}$$

$$\nabla \times \nabla \times \mathbf{B} = \nabla(\nabla \cdot \mathbf{B}) - \nabla^2 \mathbf{B} = \nabla \times \left(\mu_0 \epsilon_0 \frac{\partial \mathbf{E}}{\partial t} \right) = \mu_0 \epsilon_0 \frac{\partial}{\partial t}(\nabla \times \mathbf{E}) \tag{2.6}$$

Substituting in (2.1) and (2.2) we obtain,

$$\frac{1}{\mu_0\epsilon_0}\frac{\partial^2\mathbf{E}}{\partial t^2} - \nabla^2\mathbf{E} = 0 \tag{2.7}$$

$$\frac{1}{\mu_0\epsilon_0}\frac{\partial^2\mathbf{B}}{\partial t^2} - \nabla^2\mathbf{B} = 0 \tag{2.8}$$

which are the wave equations for the electric field and magnetic field, respectively, in free space.

Laser light is generally characterized from other light sources by its property of coherence. Here, spatial coherence describes the equivalence of the electric field properties of the light at different spatial locations across the beam profile, while temporal coherence describes the equivalence of the electric field properties at one point in space for various times. With this, the special case where the field varies in only one direction, here taken as the z direction, is a good descriptor of the electromagnetic wave propagation of laser light. With this (2.8) can be reduced to,

$$\frac{1}{\mu_0\epsilon_0}\frac{\partial^2\mathbf{E}}{\partial t^2} - \frac{\partial^2\mathbf{E}}{\partial z^2} = 0 \tag{2.9}$$

$$\frac{1}{\mu_0\epsilon_0}\frac{\partial^2\mathbf{B}}{\partial t^2} - \frac{\partial^2\mathbf{B}}{\partial z^2} = 0 \tag{2.10}$$

Solutions to this equation are waves traveling with a velocity $v = 1/\sqrt{\mu_0\epsilon_0}$, which defines the speed of light, c, in the vacuum. The values of the permittivity and permeability, and hence the speed of light, change inside a dielectric material compared to those in the vacuum, the ratio of which, ϵ/ϵ_0, defines a unit-less parameter, n, called the index of refraction. One general solution to the electromagnetic wave equation is the sinusoidal plane-wave equation, of the form,

$$\mathbf{E}(z,t) = Re\left\{\tilde{\mathbf{E}}_\mathbf{0}\exp[i(\omega t - kz + \phi)]\right\} \tag{2.11}$$

where $\tilde{\mathbf{E}}_\mathbf{0}$ is the complex vector of the electric field, ω is the angular frequency representing the temporal oscillation, ϕ is a phase term, and k is the propagation constant or wavenumber, defined by,

$$k = \frac{\omega n}{c} \tag{2.12}$$

This determines the spatial oscillation frequency of the electromagnetic wave in a medium and is more commonly denoted by its reciprocal, $\lambda = 2\pi/k$, the wavelength of spatial oscillation.

2.2 Optical beams and resonators

Laser light is distinguished from other light sources by its spatial and temporal coherence. It is the spatial coherence that gives rise to the beam nature of the laser that it is so commonly associated with. Lasers are created by inserting a gain medium inside an optical resonator. The resonator traps the optical radiation emitted by the gain medium, providing feedback loop enabling exponential gain of the circulating light field. The field will increase in strength until the gain and losses in the resonator reach parity and stead-state operation is achieved. This is the basis of the laser oscillator, which will be discussed in more detail later.

The optical resonator defines the longitudinal and transverse modes of the laser field. The longitudinal modes define the oscillation frequency of the laser light and are set by length of the optical cavity. The transverse modes define the spatial distribution of the laser field in the direction transverse to propagation. The configuration and alignment of the optical resonator determines the transverse modes it can support.

The textbooks *Lasers* by A.E. Siegman [60] and *Ultrashort Laser Pulse Phenomena* by J-C Diels and W. Rudolph [61] were used to prepare this section.

2.2.1 Optical beams

Now considering the spatial characteristics of the light field we must move away from the simple plane wave description. Expanding on this we again consider the propagation of a monochromatic light field in the z-direction,

$$E(x, y, z, t) = \tilde{u}(x, y, z) \exp[i(\omega t - k_z z) + \phi] \tag{2.13}$$

where the complex vector of the electric field, $\tilde{\mathbf{E}}_\mathbf{0}$, in (2.11) has been replaced with the complex scalar $\tilde{u}(x, y, z)$ to define the transverse beam profile. Inserting this into the wave equation (2.8) gives,

$$\frac{\partial^2 \tilde{u}}{\partial x^2} + \frac{\partial^2 \tilde{u}}{\partial y^2} + \frac{\partial^2 \tilde{u}}{\partial z^2} - 2ik_z \frac{\partial \tilde{u}}{\partial z} = 0 \tag{2.14}$$

The variation of the beam with respect to z-direction is slow compared to the rapid oscillations caused by $\exp(-ik_z z)$, as well as the transverse variations across the beam in the x- and y-directions–this is called the paraxial approximation. With this the wave equation (2.14) becomes the paraxial wave equation,

$$\left(\frac{\partial^2}{\partial x^2} + \frac{\partial^2}{\partial y^2} - 2ik_z \frac{\partial}{\partial z} \right) \tilde{u}(x, y, z) = 0 \tag{2.15}$$

The paraxial wave equation defines the set of functional forms that $\tilde{u}(x, y, z)$ can take to form an optical beam. The most frequently used solution to the paraxial wave equation is the Gaussian beam. This solution takes the form,

$$\tilde{u}(x, y, z) = \frac{1}{\tilde{q}(z)} \exp\left[-ik \frac{x^2 + y^2}{2\tilde{q}(z)} \right] \equiv \frac{1}{\tilde{q}(z)} \exp\left[-ik \frac{x^2 + y^2}{2R(z)} - \frac{x^2 + y^2}{w^2(z)} \right] \tag{2.16}$$

where $\tilde{q}(z)$ is known as the complex beam parameter that describes the propagation characteristics of the Gaussian beam. It is defined as,

$$\frac{1}{\tilde{q}(z)} \equiv \frac{1}{R(z)} - i\frac{\lambda}{\pi w^2(z)} \tag{2.17}$$

where $R(z)$ is the radius of curvature of the constant phase fronts and $w(z)$ is the transverse width of the Gaussian beam. The z-axis origin ($z = 0$) is the location where the width of the Gaussian beam is the smallest, which is defined as the beam waist w_0. At the beam waist, and at $z = \pm\infty$, the radius of curvature of the phase fronts, $R(z)$, is infinity indicating a flat phase front. As the beam propagate away from the waist the phase fronts develop a curvature and the transverse width of the Gaussian beam increases–this is the diffraction effect of the light wave. As the beam propagates the complex beam parameter evolves according to,

$$\tilde{q}(z) = \tilde{q}_0 + z = z + iz_R \tag{2.18}$$

where the initial value at the z-axis origin is,

$$\tilde{q}_0 = i\frac{\pi w_0^2}{\lambda} = iz_R \tag{2.19}$$

Here, z_R is introduced as a convenient parameter to describe the beam propagation and is called the Rayleigh length.

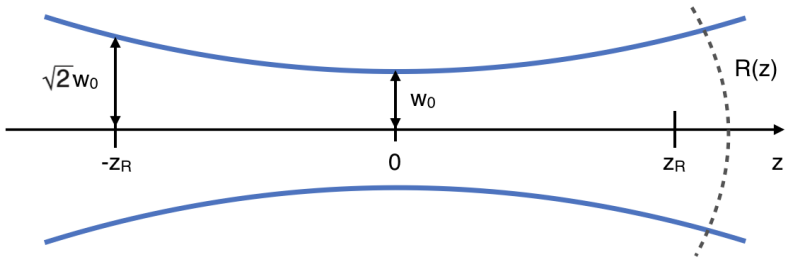

Figure 2.1: Diagram of a Gaussian beam caustic along the z-axis of propagation.

Using z_R one is able to define the critical parameters of the Gaussian beam along its axis of

propagation. Namely,

$$w(z) = w_0\sqrt{1 + (\frac{z}{z_R})^2} \tag{2.20}$$

$$R(z) = z + \frac{z_R^2}{z} \tag{2.21}$$

2.2.2 Optical resonators

Optical resonators are formed by mirrors that act to trap the optical radiation. The essential property of an optical resonator is a mirror configuration that causes the light field to exactly reproduce its spatial form after a round trip. This enables the regenerative growth of the light field when a gain medium is present inside the optical resonator. For this to occur the wavefront curvature, $R(z)$, must match the radius of curvature of the mirror it is interacting with. Thus, the configuration of the mirrors determines the stability of the optical resonator and the transverse modes it will support.

Analysis of optical resonators is usually done using the ABCD ray matrix formalism. Here, the response of each optical element is represented by a 2x2 matrix that acts on the 1x2 ray vector that describes the optical beam. The rays of the optical beam are orthogonal to the wavefront curvature of the beam and defined by a distance, x, and angle, θ from the optical axis. Any ray interacting with an optical element will have its ray vector according to,

$$\begin{bmatrix} x' \\ \theta' \end{bmatrix} = \begin{bmatrix} A & B \\ C & D \end{bmatrix} \begin{bmatrix} x \\ \theta \end{bmatrix} \tag{2.22}$$

The optical elements act in sequence allowing for the creation of a total resonator ABCD

matrix that is the product of all elements within the cavity,

$$\mathbf{M}_T = \prod_{i=0}^{i=N} \mathbf{M}_i \tag{2.23}$$

The Gaussian mode that is supported by the cavity can be determined using the total round trip ABCD matrix of the resonator. Since the beam parameter changes as it propagates through the resonator a starting and ending point must be defined when calculating the total round trip ABCD matrix. The complex beam parameter at this location is given by,

$$\frac{1}{\tilde{q}} = -\frac{A-D}{2B} - i\frac{\sqrt{1-(A+D)^2/4}}{|B|} \tag{2.24}$$

From this we can find the beam width and radius of curvature,

$$\frac{\pi w^2}{\lambda} = \frac{|B|}{\sqrt{1-(A+D)^2/4}} \tag{2.25}$$

$$R = -\frac{2B}{A-D} \tag{2.26}$$

The stability of the cavity as an optical resonator can also be determined by the round trip ABCD matrix. Since the cavity round trip must recreate the original ray vector (2.22) can be recast as an eigenvalue equation,

$$\lambda^2 - (A+D)\lambda + 1 = 0 \tag{2.27}$$

where λ here is the eigenvalue of the resonator ABCD matrix with solution,

$$\lambda = m \pm \sqrt{m^2-1}, \quad m \equiv \frac{A+D}{2} \tag{2.28}$$

This suggests that the optical cavity is stable when $|m| \leq 1$, setting the requirements for a

stable resonator to have a total round trip ABCD matrix where,

$$-1 \leq \frac{A+D}{2} \leq 1 \tag{2.29}$$

The simplest optical resonator configuration is a two mirror cavity. Here we can specify a different method for assessing cavity stability using the resonator g parameters, g_1 and g_2, given by,

$$g_1 \equiv 1 - \frac{L}{R_1} \tag{2.30}$$

$$g_w \equiv 1 - \frac{L}{R_2} \tag{2.31}$$

where R_1 and R_2 are the radii of the two mirrors M_1 and M_2, respectively, and L is the separation between the two mirrors. These define the two mirror resonator stability criterion,

$$0 \leq g_1 g_2 \leq 1 \tag{2.32}$$

The common two-mirror configurations that constitute a stable resonator include:

- Plane-parallel - Also known as the Fabry-Pérot cavity. Formed by two flat mirrors resulting in a stability parameter of 1. In practice, this cavity configuration is very sensitive to misalignment and is difficult to achieve as it only supports a mode with nearly flat wavefronts at the mirrors. Since the radii of curvature of the two mirrors are infinity, technically any spacing L supports a stable resonator. However, increasing the mirror spacing also increases its sensitivity to misalignment.

- Concentric - Created by two concave mirrors of equal radius of curvature equal to exactly one-half the spacing of the mirrors ($R_1 = R_2 = L/2$). This configuration also exists at the edge of the stability limit with each g parameter equal to -1 and

is relatively sensitive to alignment. The beam mode it supports creates a diffraction-limited spot at the cavity center, making it suitable for laser cavities where high-gain is needed, and a large mode area on the end mirrors.

- Confocal - Similar to the concentric cavity but with the two concave mirrors having a radius of curvature equal to the full spacing between the mirrors ($R_1 = R_2 = L$). With both g parameters being zero it sits in the middle of the stability zone and is rather robust to minor misalignments. For a set mirror separation this cavity configuration supports the smallest mode size on the end mirrors and is especially useful when high mode quality is desired.

- Hemispherical cavity - This cavity is formed by one flat mirror and one concave mirror with radius of curvature equal to the mirror spacing ($R_1 = L$ and $R_2 = \infty$). Like the confocal arrangement this design also is relatively insensitive to misalignment and has a low diffraction loss owing to the small mode size on the flat mirror.

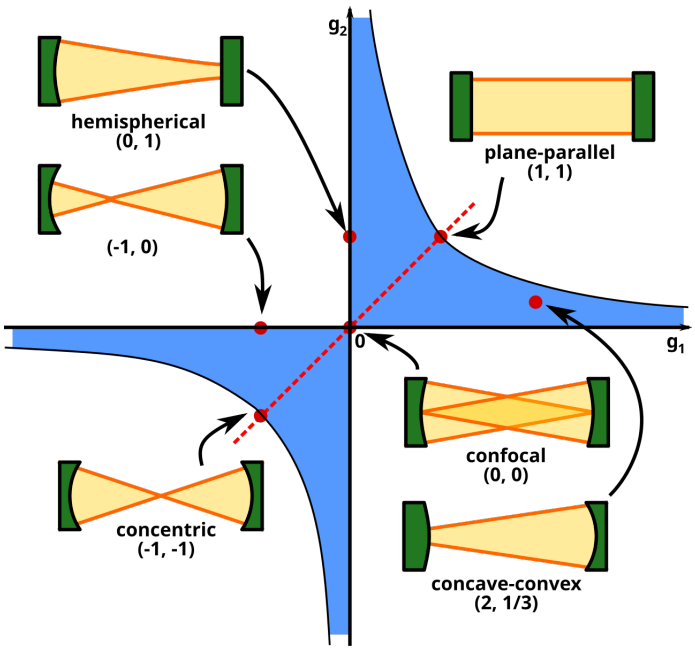

Figure 2.2: Two-mirror resonator g parameter stability diagram showing the position of some common optical resonator arrangements [62].

2.3 Direct amplification of lasers

A laser, as its acronym name suggests, is an optical device that causes light amplification by the stimulated emission of radiation. Since its invention in 1960 [1], various other methods of optical gain have been discovered, such as optical parametric amplification, so we use the term direct amplification to distinguish it here. This section briefly covers the theory behind the growth of a laser field as it is propagates through a gain medium.

The textbooks *Lasers* by A.E. Siegman [60] and *Solid State Laser Engineering* by W. Koechner [63] have been used to prepare this section.

2.3.1 Stimulated emission and rate equations

Atomic systems have well defined, discrete energy levels that electrons can populate. In certain systems the energy levels are separated by a few eV, which is comparable to the energy of an optical photon. The absorption of a photon with the bandgap energy of an atomic system will promote an electron to a higher energy level. The de-excitation of an electron from a higher level to a lower will emit a photon with exactly the bandgap energy with a frequency given by Planck's Law. Promotion of a large number of electrons to a higher energy state in an atomic system by absorption of an optical field is colloquially termed *pumping* in laser physics. Since all systems rest state is their energy minimum, these promoted electrons will decay down to the lower energy state, with a characteristic rate, emitting photons in a process called *spontaneous emission*. There is a third process, where the passage of a photon through an excited atomic system causes the de-excitation of an electron where it emits another photon that is both spatially and temporally coherent with the original–this is called *stimulated emission*.

Absorption and stimulated emission are competing processes that are dictated by the relative

difference in the number of electrons in the upper energy level, N_2, versus the lower energy level, N_1. The growth or attenuation of the electric field of frequency ω as it passes a distance z through an atomic system is given by,

$$E(z) = E_0 \exp[\alpha(\omega)z] \tag{2.33}$$

$$\alpha(\omega) = \frac{\lambda^2 \gamma_{rad}}{4\pi\Delta\omega_a} \frac{N_2 - N_1}{1 + [2(\omega - \omega_{21})/\Delta\omega_a]^2} \tag{2.34}$$

where λ is the transition wavelength, γ_{rad} is the spontaneous decay rate, ω_{21} is the characteristic frequency of the bandgap, and $\Delta\omega_a$ is the transition linewidth. It should be noted here that while the energy levels in atomic systems are discrete there are various processes that act to broaden the energy level into a band. Clearly, when there are more electrons in the upper level than lower, $N_2 > N_1$ $\alpha(\omega)$ is positive and the field grows, but when there are more in the lower than upper, $N_2 < N_1$, $\alpha(\omega)$ is negative and the field attenuates. The condition of $N_2 > N_1$ is called *population inversion*.

Population inversion cannot be achieved in a two-level energy system. All lasers operate under either a three-level or four-level energy system, and we will restrict ourselves here to four-level systems. Four-level systems are characterized by an upper-most energy level, E_3, that has a very fast spontaneous decay rate. Electrons are pumped from the ground state level, E_0, to E_3 where they rapidly decay to energy level E_2. This process generally involves the emission of phonons, quantized vibrations of the host atomic lattice, rather than photons. The energy level E_2 has a slow decay rate, enabling the electrons to stay there until an optical signal arrives to initiate the stimulated emission down to energy level E_1. Energy level E_1 also has a fast decay rate, enabling the electrons to quickly fall back down to the ground state to maintain the population inversion between levels E_2 and E_1.

The population density of the energy levels can be modeled with a set of coupled equations called the *rate equations*, which are used to find the time-dependent population inversion

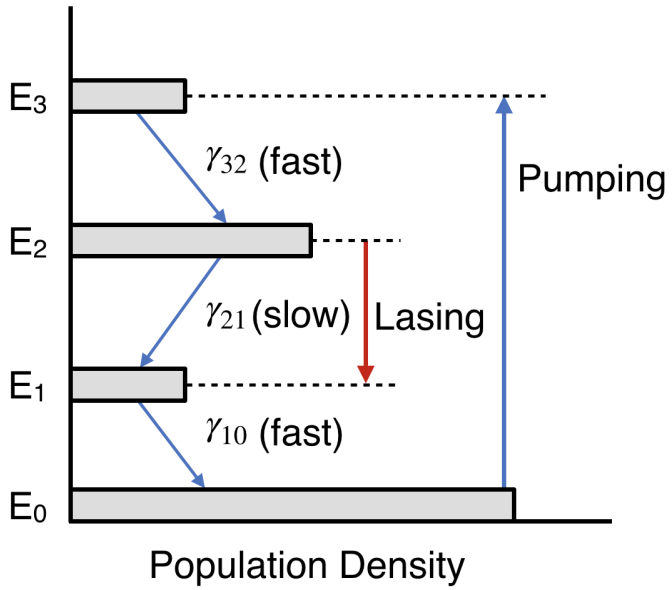

Figure 2.3: Energy level diagram of a four-level system.

Δ. Here an incident electric field has a photon density ϕ and the stimulated emission cross section for the laser level is σ, which is a probability of transition. It is assumed that the decay rate from E_3 to E_2 is so fast that the population of E_3 is zero. We will also assume that here is no degeneracy of the energy levels. Our set of equations is,

$$\frac{dN_2}{dt} = W_p N_0 - (N_2 - N_1)\sigma\phi c - (\gamma_{21} N_2 + \gamma_{20} N_2) \tag{2.35}$$

$$\frac{dN_1}{dt} = (N_2 - N_1)\sigma\phi c + \gamma_{21} N_2 - \gamma_{10} N_1 \tag{2.36}$$

$$N = N_0 + N_1 + N_2 \tag{2.37}$$

where W_p is the rate of pumping and γ is still the decay rate with subscript representing the energy level it is decaying from and to. Solving this system of equations gives the time-dependent rate equation for the population inversion, Δ,

$$\frac{\partial \Delta}{\partial t} = -N_2\sigma\phi c - \gamma_2 N_2 + W_p N_0 \tag{2.38}$$

where γ_2 is the total decay rate from N_2. The photon density of the optical signal interacting

with the gain media change according to,

$$\frac{\partial \phi}{\partial t} = c\phi\sigma\Delta \tag{2.39}$$

2.3.2 Gain and gain saturation

The intensity of an optical signal passing through a gain media of length l will increase by a factor called the small-signal gain,

$$G = \exp(\Delta\sigma l) = \exp(gl) \tag{2.40}$$

where g is the gain coefficient equal to the emission cross section multiplied by the population inversion. If the optical signal is strong enough it will begin to significantly alter the population inversion and reduce the gain as it propagates. This process is called *gain saturation*. Now describing the optical signal in terms of power density I, where $I = c\phi\hbar\omega$, the population inversion will saturate with the form,

$$\Delta = \frac{\Delta_0}{1 + I/I_{sat}} \tag{2.41}$$

where Δ_0 is the unsaturated population inversion. This in turn will reduce the small-signal gain coefficient. The saturation intensity, I_{sat}, is the intensity at which the small-signal gain coefficient is reduced half of its original value,

$$I_{sat} \equiv \frac{\hbar\omega}{\sigma\tau_{eff}} \tag{2.42}$$

where τ_{eff} is the effective lifetime of the upper laser level.

2.3.3 Pulse amplification

Consider the time-dependent population inversion equation, Eq. (2.38), where both the pumping and spontaneous decay happen on time scales much slower than an optical pulse traveling through the amplifier medium and can be neglected. As the pulse travels through the amplifier it grows according to the photon-transport equation,

$$\frac{\partial \phi}{\partial t} = c\Delta\sigma\phi - \frac{\partial \phi}{\partial z}c \tag{2.43}$$

The amplification of the pulse is determined by solving the coupled differential equations, Eq. (2.38) and (2.43), for Δ and ϕ. Solutions to this were found by L.M. Frantz and J.S. Nodvik in 1963 [64]. Of particular interest is the solution for a square shaped pulse. For a pulse with duration τ_p and initial photon density ϕ_0 propagating through an amplifier of length l,

$$\frac{\phi(z,t)}{\phi_0} = \left\{1 - [1 - \exp(-\Delta\sigma z)]\exp[-\sigma\phi_0 c\left(t - \frac{z}{c}\right)]\right\}^{-1} \tag{2.44}$$

The total energy gain is found by setting $z = l$ and integrating over all time,

$$G = \frac{1}{c\sigma\phi_0\tau_p}\ln\left\{1 + [\exp(\sigma\phi_0\tau_p c) - 1]e^{\Delta\sigma l}\right\} \tag{2.45}$$

This can be recasted using more familiar terms,

$$G = \frac{E_{sat}}{E_{in}}\ln\left\{1 + \left[\exp\left(\frac{E_{in}}{E_{sat}}\right) - 1\right]G_0\right\} \tag{2.46}$$

where E_{sat} is the saturation fluence, E_{in} in the input pulse fluence, and G_0 is the small-signal gain.

2.4 Ultrafast laser pulses

Ultrahigh-intensity lasers are created by optical pulses with moderate energy, typically J to kJ range, that exist for ultrashort durations in time, on the order of ps to fs. At this time scale, these systems are generally referred to as ultrafast lasers. Since the power of the optical pulse is the energy divided by time duration ultrafast even modest pulse energies results in very high peak-power pulses. The description of ultrafast laser pulses, their creation, and modification due to dispersion are discussed here.

The textbooks *Lasers* by A.E. Siegman [60], *Ultrashort Laser Pulse Phenomena* by J-C Diels and W. Rudolph [61], *Ultrafast Lasers* b y U. Keller [65], and *Frequency-Resolved Optical Gating: The Measurement of Ultrashort Laser Pulses* by R. Trebino [66] were used to prepare this section.

2.4.1 Time-frequency description of pulses

Ultrashort duration laser pulses are coherent electromagnetic wave packets that are expressed by the vector electric field in time and space. Taking a fixed point in space, the electric field is fully described in time by,

$$E(t) = Re\{\sqrt{I(t)}\exp[i(\omega_0 t - \phi(t))]\} \tag{2.47}$$

Here, I(t) is the temporal intensity, ω_0 is the carrier frequency, and $\phi(t)$ is the temporal phase. Examining each of these parts in succession elucidates the role each plays in the electromagnetic wave packet.

Temporal domain

Ultrashort pulses are described as having an intensity profile that is very short in the time domain, generally defined as having a full-width half max (FWHM) in the picosecond to femtosecond range or shorter. With real laser systems this profile will have an arbitrary shape, but we generally concern ourselves, and try to achieve in practice, with a few pulse profiles that have an easy analytical solution. These include, but are not limited to: Gaussian pulse, super-Gaussian pulse, sech^2 pulse, and Lorentzian pulse. Here, we will look at a Gaussian temporal pulse written as,

$$I(t) = I_0 \exp\left(\frac{-t^2}{\sigma^2}\right) \tag{2.48}$$

where I_0 is the amplitude of the pulse and σ is the width parameter that defines the pulse's duration in time. Generally, it is the intensity of a pulse, as opposed to the electric field amplitude, that that is the real, measurable quantity in the lab. This value is purely positive while the electric field amplitude that can have positive and negative values. It is important to note that the amplitude of the electric field will be the square root of the intensity value and will have a larger FWHM. Below, a is a 20-fs FWHM Gaussian pulse,

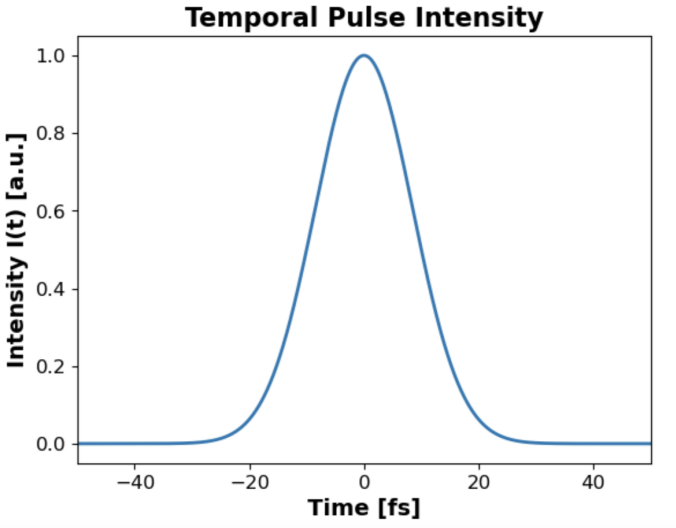

Figure 2.4: Plot of the temporal intensity a 20-fs FHWM Gaussian pulse.

The carrier frequency, ω_0, is the central angular frequency of the wave packet and is responsible for the oscillation of the electric field. It is related to the wavelength by equation (2.12). Generally, the carrier frequency of a laser will be listed as the characteristic wavelength of the amplifier material, which is the wavelength that corresponds to the peak of the emission cross-section. Applying the carrier frequency to our electric field equation we have,

$$E(t) = Re\{\sqrt{I(t)}\exp(i\omega_0 t)\} \tag{2.49}$$

The graph of a 20-fs pulse with center angular frequency at 2.355e15-Hz, corresponding to a central wavelength of 800-nm that is the characteristic wavelength of Ti:Sapphire, appears as,

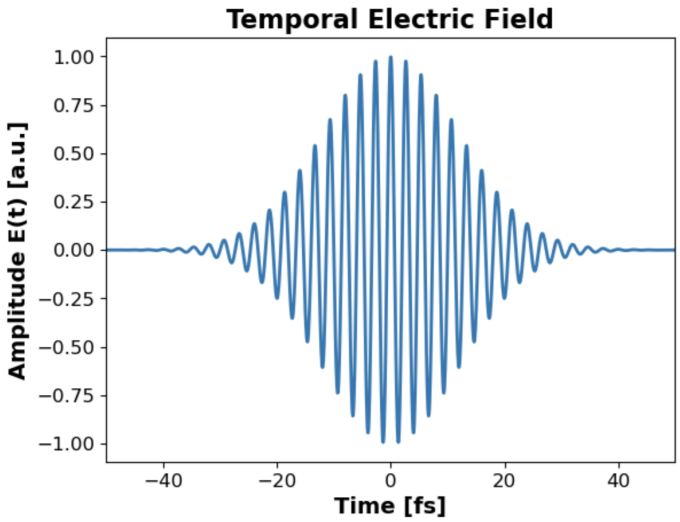

Figure 2.5: Plot of the temporal electric field of a 20-fs FHWM Gaussian pulse with a carrier angular frequency of 2.355e15-Hz.

The phase term, ϕ(t), tells us how the frequency, or color, of the pulse changes with time. The instantaneous angular frequency is the time-dependent oscillation frequency of the laser pulse electric field, and is defined by the carrier angular frequency, ω_0, and the temporal phase, $\phi(t)$, as,

$$\omega_{inst} \equiv \omega_0 - \frac{d\phi(t)}{dt} \tag{2.50}$$

This metric is useful when dealing with broadband, temporally-chirped optical pulses. If the phase term has a linear dependence on time, then this just alters the carrier frequency, where ω_0t-ϕt becomes (ω_0-ϕ)t. However, once we have a phase term with a higher-order power dependence on time, this introduces dispersion into the pulse causing the instantaneous angular frequency to vary with time. Further details on this are discussed in Section 2.5 on Dispersion.

Frequency domain

An equally valid way to represent an ultrashort pulse is in the frequency domain. An ultrashort pulse is formed by a polychromatic collection of electromagnetic waves with a fixed phase relation to one another. As such, the spectral electric field is expressed in a similar form to the temporal electric field,

$$\tilde{E}(\omega) = \sqrt{S(\omega)}exp[-i\varphi(\omega)] \tag{2.51}$$

where instead of intensity the amplitude of the spectral electric field is the square root of the power spectrum, S(ω), and we now have a spectral phase $\phi(\omega)$. In addition to the FHWM temporal duration, an ultrafast laser pulse is often characterized by its power spectrum. Like the temporal intensity, the power spectrum is the physical parameter of the frequency description of the ultrafast pulse measured in lab.

2.4.2 Fourier transform relation

The Fourier transform is a mathematical function that maps signals from the time-domain representation to the frequency-domain representation, and vice-versa. In essence, a Fourier transform breaks down any arbitrary temporal function into a sum series of weighted fre-

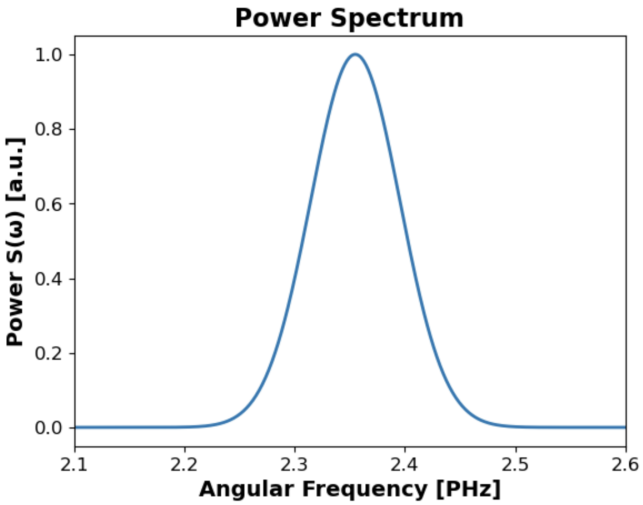

Figure 2.6: Plot of the power spectrum of a 20-fs FHWM Gaussian pulse with a carrier angular frequency of 2.355e15-Hz.

quency components. The inverse Fourier transform, as its name implies, synthesizes a temporal function from an arbitrary frequency function. This tool enables us to switch between the time-domain and frequency-domain description of ultrafast laser pulses. The Fourier transform is an integral transform and is commonly expressed as,

$$\tilde{E}(\omega) = FT\left\{E(t)\right\} = \int_{-\infty}^{\infty} E(t)e^{-i\omega t}dt \tag{2.52}$$

$$E(t) = FT^{-1}\left\{E(\omega)\right\} = \frac{1}{2\pi}\int_{-\infty}^{\infty} \tilde{E}(\omega)e^{+i\omega t}d\omega \tag{2.53}$$

Here, FT is the Fourier transform with acts on the temporal electric field to give the frequency representation, while FT^{-1} is the inverse Fourier transform acting on the spectral electric field to give the temporal representation. The factor of $1/2\pi$ is a normalization factor. There are certain functions whose Fourier transform is also an analytic function, these are described as Fourier pairs. Each of the pulse profile shapes previously mentioned have a Fourier pair; Gaussian pulse shapes are nice to work with because the Fourier conjugate of a Gaussian is another Gaussian. Table 2.1 below shows some common Fourier transform pairs encountered in ultrafast laser pulses.

$E(t)$	$\tilde{E}(\omega)$
1	$2\pi\delta(\omega)$
$\delta(t)$	1
$e^{i\omega_0 t}$	$2\pi\delta(\omega-\omega_0)$
e^{-at^2}	$\frac{1}{\sqrt{2a}}e^{-\frac{\omega^2}{4a}}$
$e^{-a\lvert t\rvert}, a>0$	$\sqrt{\frac{2}{\pi}}\frac{a}{a^2+\omega^2}$
e^{iat^2}	$\frac{1}{\sqrt{2a}}e^{-i(\frac{\omega^2}{4a}-\frac{\pi}{r})}$
$rect(at)$	$\frac{1}{\sqrt{2\pi a^2}}sinc(\frac{\omega}{2\pi a})$
$sinc(at)$	$\frac{1}{\sqrt{2\pi a^2}}rect(\frac{\omega}{2\pi a})$

Table 2.1: Commonly used Fourier transform pairs.

2.4.3 Time-Bandwidth product

Examining the Fourier transform pairs in Table 2.1, we see that there is a reciprocal relationship between the duration of the temporal function and the bandwidth of the frequency function. Namely, a shorter duration temporal pulse requires a broader bandwidth of the frequency spectrum. To achieve the shortest duration temporal pulse for a given bandwidth there must be a constant phase for all frequencies in the spectrum. Typically the temporal duration of a laser pulse, τ_p, is defined by the FWHM of its temporal intensity, $I(t)$. Likewise, the bandwidth of a laser pulse, $\Delta\nu_p$, is defined as the FWHM of the power spectrum, $S(\omega)$. When a constant phase across all frequencies is achieved the pulse is said to be bandwidth limited or Fourier transform limited (FTL). Different spectral pulse shapes can achieve a different FTL pulse duration, which is given by the time-bandwidth product (TBP) for that

particular function,

$$TBP = \tau_p \times \Delta\nu_p \tag{2.54}$$

To illustrate the inverse relation between bandwidth and pulse duration, plotted below are

Function	TBP
Gaussian	0.4413
Hyperbolic secant	0.3148
Lorentzian	0.2206
Rectangle	0.8859

Table 2.2: Time-bandwidth product for various pulse shapes.

two Gaussian pulses. The first pulse has a FWHM pulse duration of 20-fs and a corresponding frequency bandwidth of 0.022065-PHz. The second pulse has a FWHM pusle duration of 10-fs and as a consequence a larger frequency bandwidth of 0.04413-PHz. The time-bandwidth product for both is 0.4413 as they are both Gaussian functions.

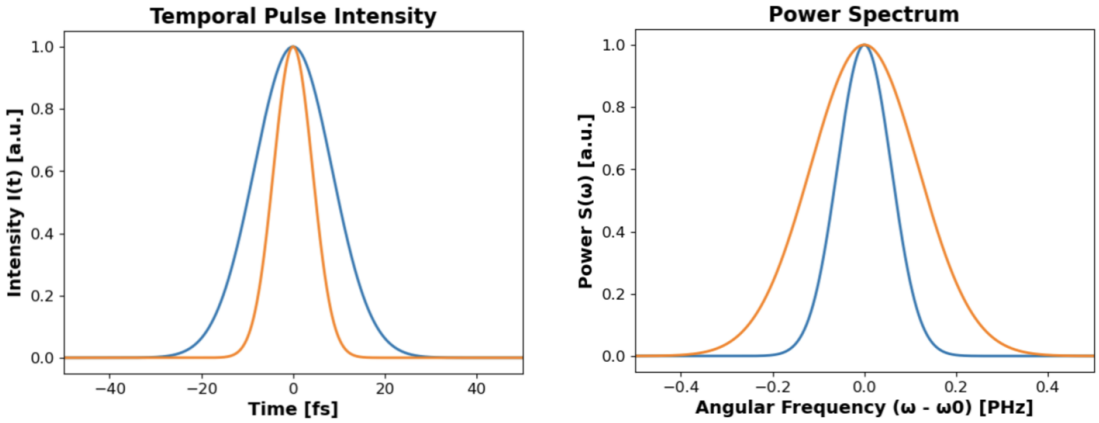

Figure 2.7: Plot of two ultrafast pulses with a Gaussian envelope and their corresponding power spectra.

2.4.4 Modelocking

Simply having spectral bandwidth is not sufficient for the creation of an ultrafast laser pulse. To achieve pulse formation the spectral components must have a fixed phase relationship to one another. The temporal electric field of an ultrafast pulse can be described as the sum of monochromatic plane waves,

$$E(t) = \sum_n E_n Re\left\{\exp[i(\omega_n t + \phi_n)]\right\} \tag{2.55}$$

To form the ultrafast pulse the monochromatic plane waves must constructively interfere at a single point in time. If we take ϕ_n to be zero for all spectral components each of the monochromatic plane waves will have its maximum located at $t = 0$, constructively adding together. Due to the different temporal frequency of the various monochromatic plane waves, as we move away from $t = 0$ the maxima of the sinusoidal oscillations are no longer coinciding and the monochromatic plane waves begin to destructively interfere with one another. This is best seen in the temporal intensity of the pulse. This is illustrated below by plotting the temporal electric field amplitude of five different evenly-spaced, monochromatic plane waves and the temporal intensity distribution created by summing the fields together.

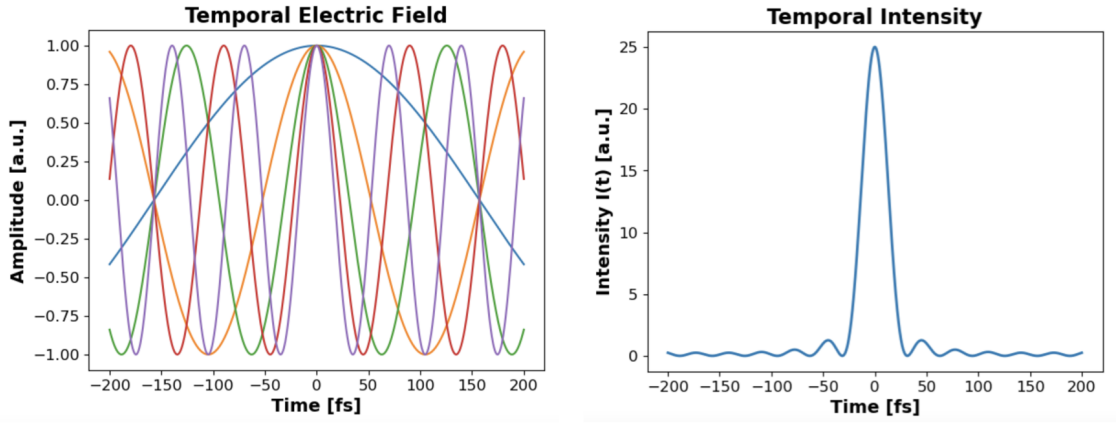

Figure 2.8: Temporal electric field amplitude of five different evenly frequency-spaced, monochromatic plane waves and the temporal intensity distribution created by summing the fields together.

Modelocked lasers produce a chain of temporal pulses periodically spaced in time, normally with a repetiton rate equal to the inverse of the round-trip transit time in the laser's optical cavity. Methods to achieve modelocking are generally divided into two broad categories– active and passive. In each of these categories there are a number of different techniques, which are briefly describe here.

Active modelocking

In active modelocking an externally controlled device is periodically triggered to modulate either the amplitude or phase of a pulse in an optical cavity. Typically the frequency of the modulation is the round-trip time of the pulse to transverse the optical cavity. The most common techniques employ an optical device that provides a sinusoidal loss, such as an acousto-optic or electro-optic modulator. Intracavity losses are minimized when a pulse circulates in the optical cavity with the correct timing. This pulse will outcompete pulses that are not correctly timed to the external modulator. Active modelocking is limited in its shortest achievable pulse duration to the picosecond range.

Passive modelocking

In passive modelocking the modulation is provided by the optical field itself by the inclusion of a saturable absorber, which allows for the generation of shorter pulses down to the femtosecond range. Saturable absorbers produce a high loss on low intensity optical signals and a much lower loss on high intensity signals. This leads to an effect called self-amplitude modulation (SAM). Noise fluctuations in the optical cavity impart a random phase to the various frequency components causing random intensity spikes. When a noise spike is formed it experiences less loss from the saturable absorber, saturating the gain in the optical cavity and continuing to propagate forming a stable pulse train.

The most common physical saturable absorber is the semiconductor saturable absorber (SESAM). This device is a Bragg mirror formed by alternating layers of different semiconductor material. When interacting with an optical signal electrons will be promoted from the valence band into the conduction band as light is absorbed. However, due to the finite occupancy number of the conduction band, the absorption is reduced if the promotion to the conduction band happens on a timescale faster than the relaxation of the electrons back to the valence band. High intensity, short duration pulses will quickly saturate the SESAM experiencing less loss compared to low intensity, continuous wave radiation.

2.4.5 Kerr lens modelocking

Another passive modelocking technique uses an artificial saturable absorber by exploiting the change in a material's index of refraction when interacting with high intensity light. The polarization density, $\mathbf{P}$, of a dielectric material expresses the volumetric density of electric dipoles formed in the material when subjected to an electric field, which in turn affects the electric field itself. In linear dielectric materials it is expressed as,

$$\mathbf{P} = \epsilon_0 \chi_e \mathbf{E} \tag{2.56}$$

where ϵ_0 is the permittivity of free space as seen in Maxwell's equations, χ_e is the electric susceptibility, and $\mathbf{E}$ is the applied electric field. The electric susceptibility is material dependent and expresses the degree to which electric dipoles will form in the dielectric material per unit of electric field strength and is derived from the permittivity, ϵ, of the dielectric material,

$$\chi_e = \epsilon_r - 1 = \frac{\epsilon}{\epsilon_0} \tag{2.57}$$

As mentioned in Section 2.1.2, the ratio of a dielectric materials permittivity to the permittivity in free space determines the speed of light in the media and is expressed as the index of refraction for that material,

$$n = \sqrt{\frac{\epsilon}{\epsilon_0}} = \sqrt{1 + \chi_e} = \frac{c}{v} \tag{2.58}$$

As the electric field strength increases the polarizability of a material begins to saturate and the polarization density deviates away from this linear treatment. This can be described by expanding the polarizability with a Taylor expansion to define the nonlinear susceptibility of a dielectric material,

$$\mathbf{P} = \epsilon_0 \chi_e^{(1)} \mathbf{E} + \epsilon_0 \chi_e^{(2)} \mathbf{E}^2 + \epsilon_0 \chi_e^{(3)} \mathbf{E}^3 + \cdots \tag{2.59}$$

The higher order terms of the electric susceptibility become appreciable at high electric field strengths. The net result of this is a modification to the index of refraction of a dielectric material when interacting with a high strength electric field, also known as the optical Kerr effect. The index of refraction is in the presence of an intense field is written as,

$$n = n_0 + n_2 I(t) \tag{2.60}$$

where n_0 is the linear index of refraction, n_2 is the nonlinear refractive index, and $I(t)$ is the pulse intensity. A Gaussian beam has its highest intensity at the center and decreases radially outward. When the beam has sufficient field strength and propagates through a dielectric material it experiences a radially varying index of refraction due to the optical Kerr effect. This causes a radially varying nonlinear phase shift on the beam as it passes through the medium of length L,

$$\Delta\phi(r,t) = -\frac{\omega}{c} n_2 I(r,t) L = -\frac{2\pi}{\lambda} n_2 I(r,t) L \tag{2.61}$$

where ω is the frequency of the signal, c is the speed of light, and λ is the wavelength of the signal. A radially varying phase acts exactly as a lens does. Thus, the optical Kerr effect produces a positive lens in the dielectric material as a high intensity pulse travels through it and focuses the beam.

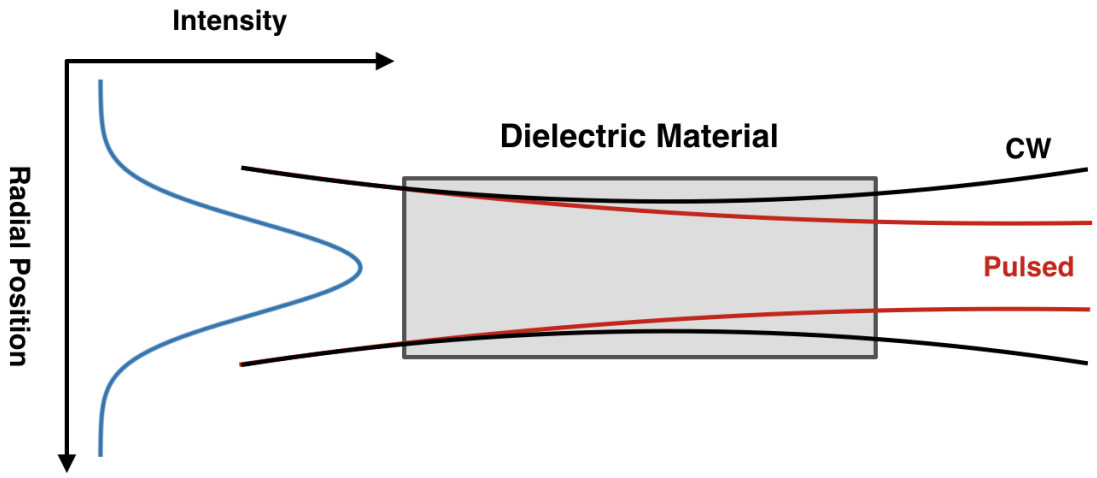

Figure 2.9: Diagram of the Kerr lens effect focusing a Gaussian beam in a dielectric material.

When included in an optical resonator, the Kerr lens modifies the round trip cavity stability matrix. This can be exploited so that only a high intensity pulse is supported in the optical cavity.

2.5 Dispersion

In the temporal representation of the ultrafast pulse, Eq.(2.47), it was discussed that the temporal phase, $\phi(t)$, along with the center angular frequency, ω_0, describes the instantaneous angular frequency of the electric field given by Eq.(2.50). When dealing with polychromatic light sources, such as ultrafast pulses, it is convenient to use the frequency representation as seen in Eq. (2.51). Here, the spectral phase, $\varphi(\omega)$ provides information about the time vs. frequency of the ultrafast pulse. Typically the spectral phase is expressed in terms of its

Taylor series expansion,

$$\varphi(\omega) = \varphi(\omega_0) + \frac{\partial\varphi}{\partial\omega}(\omega - \omega_0) + \frac{1}{2}\frac{\partial^2\varphi}{\partial\omega^2}(\omega - \omega_0)^2 + \frac{1}{6}\frac{\partial^3\varphi}{\partial\omega^3}(\omega - \omega_0)^3 + \cdots \tag{2.62}$$

It is important to note here that the spectral phase can be expressed in terms of frequency or wavelength by using the mapping $\varphi_\lambda(\lambda) = \varphi_\omega(2\pi c/\lambda)$. Examining each of the terms in this series provides valuable insight into how the structure of the ultrafast pulse evolves as it propagates and interacts with various optical elements.

The zeroth-order term in the Taylor series, $\varphi(\omega_0)$, is just a constant phase offset on the spectral electric field. Since it is a constant term, under a Fourier transform to the temporal domain it is the same (i.e. $\varphi_0 = \phi_0$). It has no effect on the temporal pulse envelope, but does shift the relative position of temporal electric field oscillation within the temporal intensity envelope. This term is not very important until dealing with near single-cycle pulses where it is referred to as the carrier envelope phase.

The linear term, $\partial\varphi/\partial\omega$, is generally called the group delay (GD) or τ_g. When the spectral phase contains only this first-order term (i.e. $\varphi(\omega) = \tau_g\omega$) the Fourier transform on the spectral electric field follows the Fourier Shift Theorem and manifests as a time shift on the temporal electric field (i.e. $E(t - \tau_g)$). As the pulse propagates a distance L in free space it will accumulate a spectral phase of $\varphi = \omega L/c = 2\pi L/\lambda$, generating a group delay of $\tau_g = d/c$. Like the carrier envelope phase the group delay does not affect the envelope of the temporal pulse.

The introduction of the second-order spectral phase term, $\partial^2\varphi/\partial\omega^2$, begins to alter the shape of the temporal pulse envelope and is referred to as the group delay dispersion (GDD). Physically it represents the spectral component having linearly varying different group delay, typically manifesting as the different spectral components separating from each other in time. Consider a Gaussian spectral pulse with purely second-order spectral phase. The following

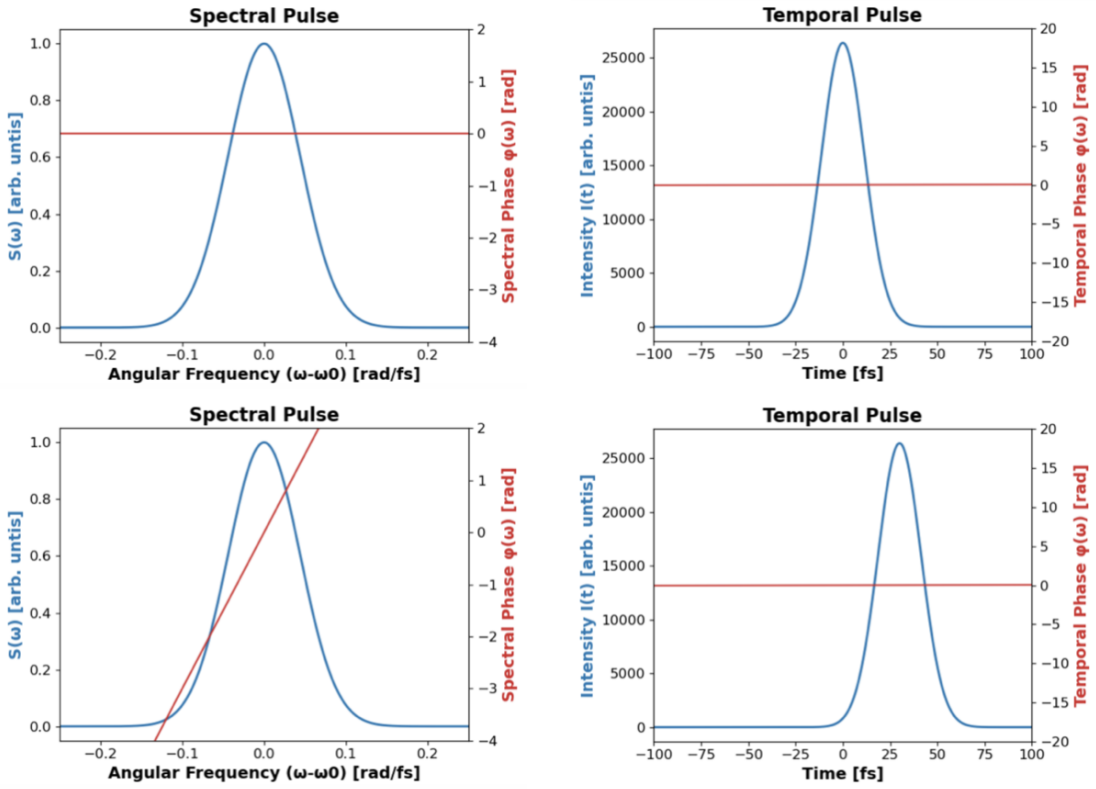

Figure 2.10: Example of the group delay effect on an ultrafast pulse. On the top row the spectral phase is zero and the corresponding temporal pulse is centered at 0-fs. On the bottom row a linear spectral phase of 30-fs shifts the corresponding temporal pulse by 30-fs.

derivation comes from a non-archived paper titled "Fourier Transform of a Linearly-Chirped Gaussian Pulse" by David J. Gibson from 2006. Since it cannot be cited it has been included in the Appendix. For clarity in the final answer the power spectrum is defined as,

$$S(\omega) = \frac{1}{2\sqrt{a^2+b^2}} E_0^2 \exp\left[\frac{-a\omega^2}{2(a^2+b^2)}\right] \tag{2.63}$$

which has a spectral electric field of the form,

$$\tilde{E}(\omega) = \frac{1}{\sqrt{2(a+ib)}} E_0 \exp\left[-\frac{\omega^2}{4(a+ib)}\right] \tag{2.64}$$

Isolating the imaginary term in the exponent gives a spectral phase of,

$$\varphi(\omega) = \frac{b}{a^2 + b^2}\omega^2 \tag{2.65}$$

The temporal electric field found from the Fourier transform of this spectral electric field is,

$$E(t) = E_0 \exp[-at^2] \exp[-i\omega(t)t] \tag{2.66}$$

Multiplying the temporal electric field by its complex conjugate gives us the temporal intensity of this Gaussian spectral pulse with second-order dispersion,

$$I(t) = E_0^2 \exp[-2at^2] \tag{2.67}$$

The temporal pulse is another Gaussian, with a width parameter that is inversely proportional to the magnitude of the second-order spectral phase. As group delay dispersion accumulates on the spectral pulse it acts to broaden the temporal pulse in time.

The third-order term, $\partial^3\varphi/\partial\omega^3$, is often simply referred to as third-order dispersion (TOD). This results in a quadratic variation of spectral component's group delay. Here the spectral wings of the pulse are clumped to one side of the central frequency in temporal space resulting in an asymmetric temporal pulse profile. The higher-order phase terms beyond the third-order really only come into effect for very large bandwidth spectral pulses, where the temporal pulse is on the order of a few optical cycles, or in optical systems that induce a large amount of dispersion.

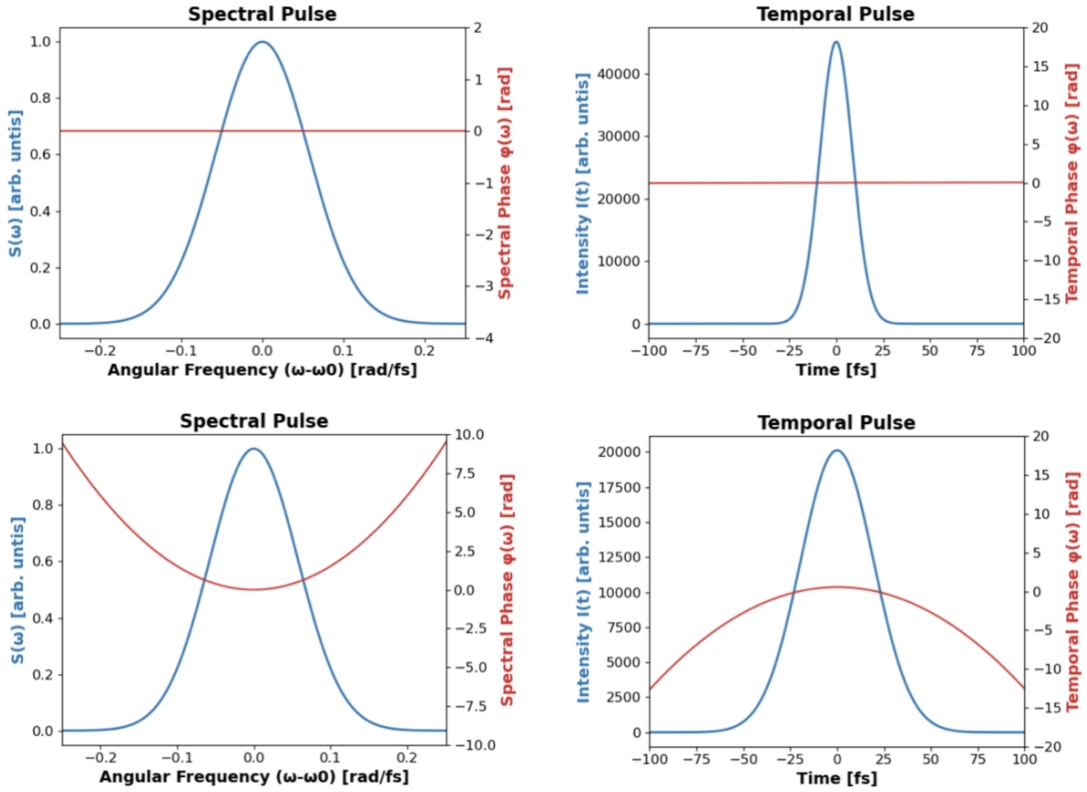

Figure 2.11: On the top row a Gaussian spectral pulse, with zero spectral phase, with the appropriate bandwidth that produces a 20 fs FWHM temporal pulse. On the bottom row a Gaussian pulse with the same spectral bandwidth but a GDD of 6000 fs^2, which broadens the temporal pulse FWHM to 46 fs.

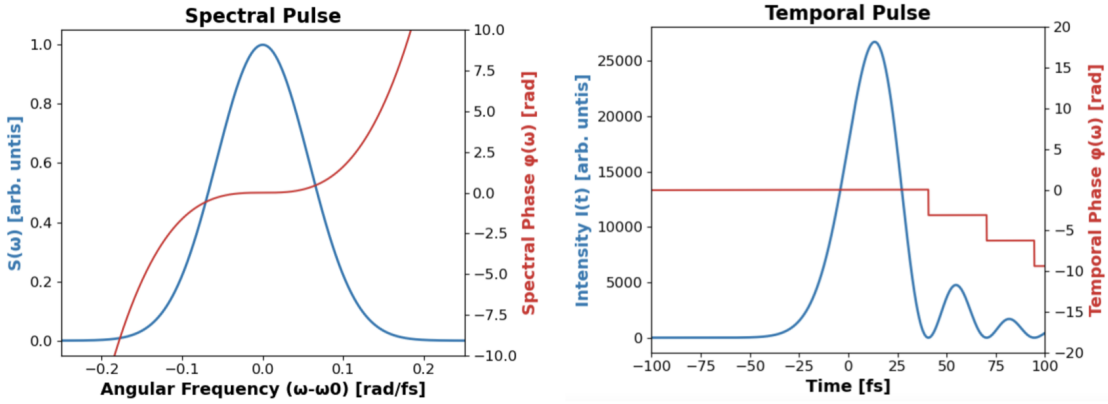

Figure 2.12: A Gaussian spectral pulse with a TOD of 4E+5 fs^3 resulting in the temporal intensity plot. The staircase temporal phase is a numerical artifact of the phase unwrapping algorithm and is immaterial.

2.5.1 Material dispersion

As previously discussed, when a pulse propagates through free space it accumulates a linear spectral phase, resulting in a group delay but maintaining the pulse envelope shape. However, this is not the case when a pulse travels through a dielectric medium. A pulse traveling a length L through a dielectric medium of refractive index n will accumulate a spectral phase of,

$$\varphi(\omega) = \frac{\omega L n(\omega)}{c} \tag{2.68}$$

However, the refractive index of a material is frequency dependent and the derivative of the spectral phase gives a frequency dependent group delay. The term Ln is commonly referred to as the optical path length (OPL). The spectral response of the refractive index is generally shown in terms of wavelength, λ, and modeled by the Sellmeier equation of the form,

$$n^2(\lambda) = 1 + \sum_i \frac{B_i \lambda^2}{\lambda^2 - C_i} \tag{2.69}$$

Most materials are described with two or three summation terms where B_i and C_i are called the Sellmeier coefficients. These coefficients are experimentally measured using techniques such as white light interferometry. The material dispersion of a medium imparts a non-linear spectral phase as the pulse travels through it distorting the pulse envelope. This is best written in terms of wavenumber, k, and wavelength,

$$\varphi_{OPL}(k) = kLn \tag{2.70}$$

$$\frac{\partial \varphi(k)}{\partial k} = -\frac{\lambda^2}{2\pi}\frac{\partial \varphi(\lambda)}{\partial \lambda} \tag{2.71}$$

$$\frac{\partial \varphi(\lambda)}{\partial \lambda} = -\frac{\lambda^2}{2\pi}\frac{\partial}{\partial \lambda}\left[\frac{2\pi L n(\lambda)}{\lambda}\right] = Ln(\lambda) - \lambda L \frac{\partial}{\partial \lambda}\left(\sqrt{1 + \sum_i \frac{B_i \lambda^2}{\lambda^2 - C_i}}\right) \tag{2.72}$$

2.5.2 Angular dispersion

While material dispersion can be thought of as acting purely along the time-axis of a pulse (i.e., the longitudinal spatial-axis of co-propagation) to temporally spread the spectral components, angular dispersion works by distributing the spectral components across the transverse spatial dimension. This, in turn, enables the management of the spectral phase by controlling the path length, and thus group delay, of the various spectral components. Angular dispersion is created by an optical element that induces a frequency dependent change to the direction of propagation (i.e. $\partial\theta/\partial\omega \neq 0$).

The simplest case of this is polychromatic light incident at a dielectric interface at an oblique angle. Here, the light is refracted at the dielectric interface at an angle according to Snell's law,

$$\theta_2(\omega) = \arcsin\left[\frac{n_1(\omega)}{n_2(\omega)}\sin(\theta_1)\right] \tag{2.73}$$

where the frequency dependence of the angle of refraction leads to angular dispersion. In normally dispersive materials, the refractive index is higher for higher frequency, lower wavelength, spectral components causing them to be refracted stronger.

Another angularly dispersive device is the diffraction grating. A diffraction grating is is formed by a periodically spaced groove structure on a surface, with groove spacing on the order of the wavelength of light, that acts to coherently scatter light incident on the surface. Each groove scatters the incident light in a spherically emanating wave as if it was a point source. Where these spherical waves overlap with a constant phase front determines the angle at which the light is diffracted off the surface. These phase fronts often produce harmonics that enable multiple orders of diffraction, producing multiple diffracted beams from a single

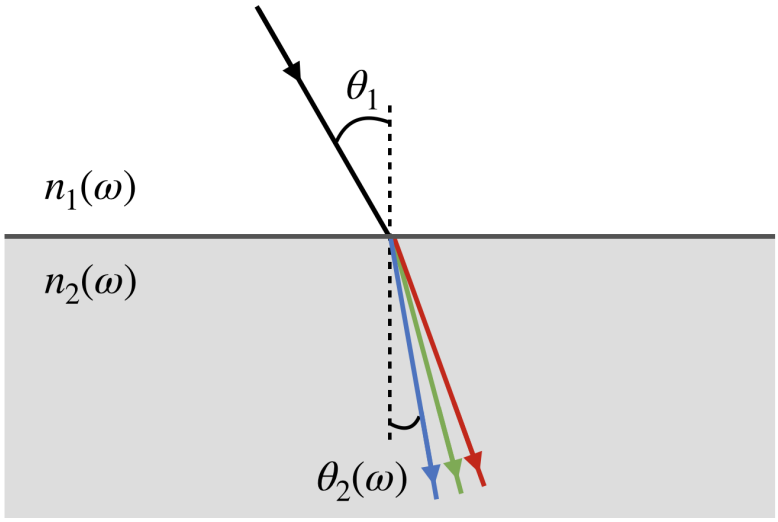

Figure 2.13: A polychromatic light source where all frequencies are incident on a dielectric interface with angle θ_1 and refracting at different angles given by Snell's law.

incident beam. The angle of diffraction is described by the grating equation,

$$\theta_m = \arcsin\left(\sin(\theta_i) + \frac{m\lambda}{d}\right) \tag{2.74}$$

Where θ_i is the incident angle of the light, m is the diffraction order, λ is the wavelength of light, and d is the groove spacing of the diffraction grating. It is important to note that groups will use different sign convention for the diffraction order based on how the define the diffraction angle. The wavelength dependence of the angle of diffraction is the basis for the angular dispersion produced by a diffraction grating, which is given by,

$$\frac{\partial\theta_m}{\partial\lambda} = \frac{m}{d\sqrt{1 + [\sin(\theta_i) + \frac{m\lambda}{d}]^2}} \tag{2.75}$$

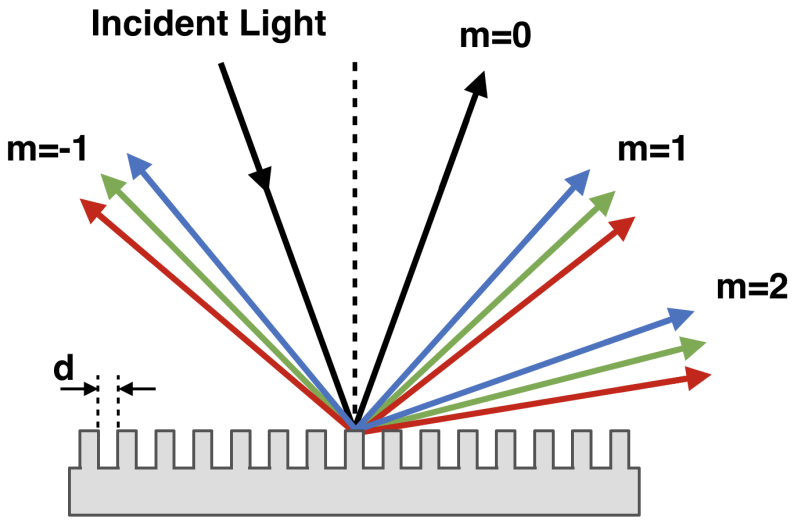

Figure 2.14: A polychromatic light source where all frequencies are incident on a dielectric grating, of groove spacing d, with angle θ_1 and diffracting into multiple diffraction orders with an angle given by the grating equation.

2.5.3 Temporal chirp

It was previously shown how a second-order spectral phase, or GDD, produces a temporal phase with a quadratic functional form. This produces an instantaneous frequency that varies linearly with time, which is often called a linear temporal chirp. From the equation for instantaneous frequency, Eq. (2.50), and the temporal electric field found from a spectral pulse with GDD, Eq. (2.66), we see,

$$E(t) = E_0 \exp[-at^2] \exp[-i(\omega_0 + bt)t] \tag{2.76}$$

$$\omega_{inst}(t) = \omega_0 - \frac{d\phi(t)}{dt} = \omega_0 + bt \tag{2.77}$$

The connection between linear temporal chirp and GDD highlights how one can achieve temporal pulse broadening by causing the different frequency components of a pulse to arrive at a location at different times. Positive temporal chirp refers to a pulse whose instantaneous frequency increases with time, while negative temporal chirp is the inverse where the instantaneous frequency decreases with time. Materials with normal dispersion

cause positive chirp, where the “red” light will travel faster through the material than the “blue” light. In a non-dispersive medium, temporal chirp can be induced by forcing the different frequencies to take a different path length, which is often accomplished using angular dispersion.

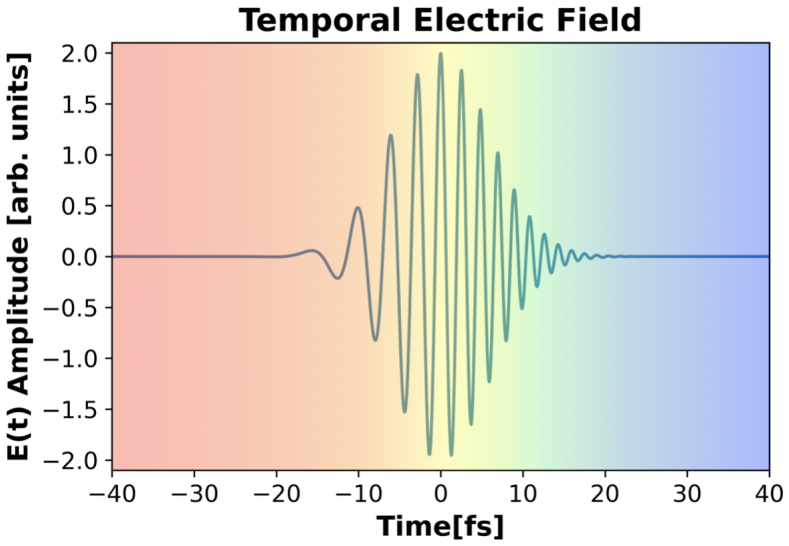

Figure 2.15: Temporal electric field with positive chirp showing the lower, ”red”, frequency components arriving earlier in time than the higher, ”blue”, frequency compnents.

2.5.4 Spatial chirp

Analogous to how temporal chirp distributes the frequency components along the temporal (longitudinal) axis, spatial chirp distributes the pulse contents in the spatial axis transverse to the direction of propagation and is created by optical elements that induce angular dispersion on the pulse. A formalism for spatial chirp in ultrafast optics was put forward by X. Gu, S. Akturk, and R. Trebino in 2004 [67]. Since spatial chirp is necessarily a spatio-spectral effect it can be defined in either space or frequency. In the frequency domain, examining the central angular frequency, ω_0, at each spatial position along an axis transverse to pulse propagation, here taken to be the x-direction, will give a function $\omega_0(x)$. The variation of this function with respect to the spatial dimension, $\nu \equiv d\omega_0/dx$, is called the frequency gradient. In the

spatial domain, each frequency can be considered as its own spatial beamlet, individual from the rest in the pulse, centered at x_0. Collecting this for all frequencies in the pulse results in the function $x_0(\omega)$, and its variation with respect to frequency, $\zeta \equiv dx_0/d\omega$, is called the spatial dispersion.

Consider a Gaussian pulse in the frequency domain, Eq. (2.51), that now has a Gaussian spatial distribution. Without spatial chirp this spatio-spectral pulse is written as,

$$\tilde{E}(x,\omega) = A_x(x)A_\omega(\omega)\exp[-i\varphi(\omega)] \tag{2.78}$$

$$\tilde{E}(x,\omega) = E_0 \exp\left[-\left(\frac{x}{\Delta x}\right)^2\right] \exp\left[-\left(\frac{\omega}{\Delta\omega}\right)^2\right] \exp[-i\varphi(\omega)] \tag{2.79}$$

where $A_\omega(\omega) = \sqrt{S(\omega)}$. Here the spatial envelope and the spectral envelope are separable. However, with the presence of spatial chirp on the pulse the envelopes become functions of both variables, where the frequency gradient, ν, acts on the frequency envelope, A_ω, and the spatial dispersion, ζ, acts on the spatial envelope, A_x. When numerically modeling spatio-spectral pulse propagation we have found it much more convenient to use the spatial dispersion description of spatial chirp. Restricting ourselves to that definition, the spatio-spectral pulse with spatial chirp is written as,

$$\tilde{E}(x,\omega) = E_0 \exp\left[-\left(\frac{x-\zeta\omega}{\Delta x}\right)^2\right] \exp\left[-\left(\frac{\omega}{\Delta\omega}\right)^2\right] \exp[-i\varphi(\omega)] \tag{2.80}$$

In practice, the spatial dispersion is almost never linear as the angular dispersion always has higher-order terms that distribute the frequency components in a non-linear manner. When numerically modeling spatio-temporal pulse propagation a function for $x_0(\omega)$, based off the angular dispersion, is written and used in place of $\zeta\omega$. When using spatial chirp in ultrafast optics it is generally desired to remove the angular dispersion, if this is not done the spatial chirp will continue to change as the pulse propagates. Applying the opposite amount of angular dispersion, using the same optical element that generated it, will cancel out the

angular dispersion but leave the pulse spatially chirped. In a slab of dielectric material with parallel faces the angular dispersion generated at the first interface is naturally undone when the pulse travels out through the second interface. Parallel prism pairs, which are often used as intracavity cavity elements in oscillators to manage dispersion, are essentially dielectric slabs that have been cut into two identical triangle prisms with an air gap between them. Consequentially, the parallel prism pair spatially chirps an ultrafast laser pulse in the same manner as a dielectric slab. With gratings, spatial chirp is generated by aligning the gratings in a parallel-facing pair. In this way, all frequencies diffracting off of the first grating will now have an angle of incidence on the second grating equal to their the diffraction angle from the first. Each frequency component is then diffracted off at the original angle of incidence to the first grating but the pulse packet is spatially chirped.

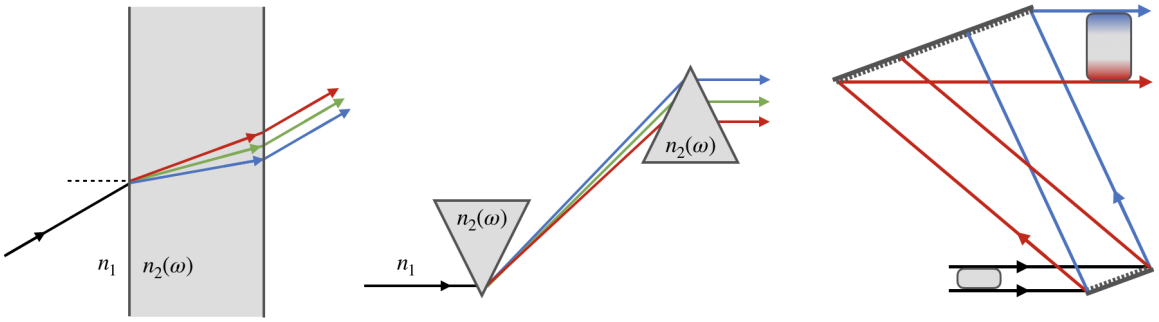

Figure 2.16: Spatial chirp generated by a light incident at an oblique angle on a dielectric slab, (left) and by a parallel grating pair (right).

2.6 Chirped pulse amplification (CPA)

In the early years of lasers, pulse peak-power was limited by optical damage inside the solid-state gain material. In 1985 Mourou and Strickland, inspired by high-power radar techniques, realized that temporally stretching a pulse prior to amplification reduces the pulse intensity in the gain medium, avoiding optical damage and enabling higher energy extraction [9]. When the pulse is temporally recompressed after amplification this resulted in laser peak-

powers previously unachievable. This technique, called chirped pulse amplification (CPA), lead to a rapid increase in laser peak-power from the gigawatt to petawatt level.

High-intensity CPA lasers systems are built using the master oscillator power amplifier (MOPA) architecture, which had been ubiquitous in high-energy laser systems prior to CPA. Here, a seed pulse originates as a low energy, typically ∼nJ level, ultrafast pulse from a laser oscillator. The ultrafast seed pulse is then temporally stretched, on the order of picoseconds to nanoseconds, prior to entering a chain of laser amplifiers. This chain generally consists of, in order, a regenerative amplifier, multi-pass amplifier, and finally a power amplifier. In between each amplification stage the beam is expanded to maintain a similar pulse fluence in each amplifier. After amplification the now high-energy pulse is temporally recompressed to an ultrafast pulse with high peak-power. It is then focused down to a small spot, $\sim \mu$m diameter, where the reduction in beam size produces an ultrahigh-intensity pulse.

2.6.1 Pulse compressors

The pulse compressors used in ultrahigh-intensity lasers are almost always grating based compressors. Their operation is more intuitive to understand than the pulse stretcher, so it is helpful to start with their description. Section 2.5.2 and 2.5.4 discussed how the interaction of a polychromatic pulse with a parallel grating pair will result in a spatial chirp on the output chirp due to the angular dispersion of the gratings. In addition to the spatial chirp, the angular dispersion also induces a large negative GDD on the pulse [53]. As the frequency components travel from the first grating to the second, the angular dispersion causes a frequency dependent path length.

Consider a monochromatic beam of frequency ω entering a parallel grating pair with grating normal separation L and groove spacing d, giving a groove frequency f. To find the group delay of the spectral component ω we must determine the total phase accumulated as it

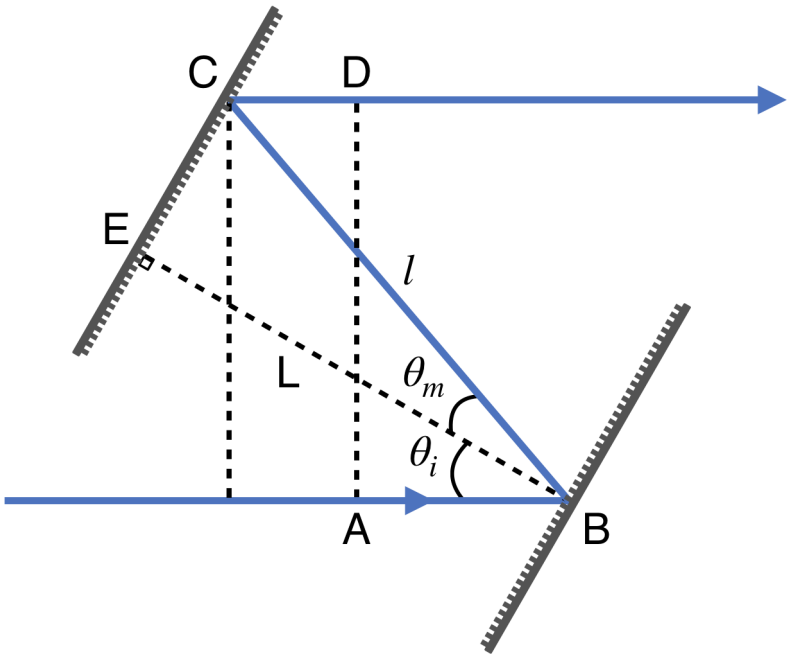

Figure 2.17: Diagram of the path traveled by monochromatic light between a parallel grating pair.

travels through the grating pair. First arbitrarily define two points, A and D, that form a plane perpendicular to the incoming and outgoing ray. The path length traveled along $\overline{ABCD}$ is,

$$\overline{ABCD} = l + l\cos[\theta_i + \theta_m(\omega)] \tag{2.81}$$

$$\overline{ABCD} = \frac{L}{\cos[\theta_m(\omega)]}\{1 + \cos[\theta_i + \theta_m(\omega)]\} \equiv p(\omega) \tag{2.82}$$

Where θ_m is taken as the first order diffraction found by the diffraction equation Eq. (2.74). In Section 2.5.2 it was mentioned that the diffracted rays are defined by the constant wavefronts created by spherical waves originating as each grating groove. To find the total phase accumulated by the spectral component ω we must take into account the 2π phase shift that occurs between each groove. The number of grooves the ray transverses between the first and second grating is the distance $\overline{CE}$ times the groove density f, resulting in a phase

accumulation of,

$$g(\omega) = 2\pi f L \tan[\theta_m(\omega)] \tag{2.83}$$

Now the group delay is found by taking the derivative of the spectral phase with respect to frequency,

$$\tau_g(\omega) = \frac{\partial \varphi(\omega)}{\partial \omega} = \frac{\partial}{\partial \omega}\left[\frac{\omega p(\omega)}{c} + g(\omega)\right] = \frac{p(\omega)}{c} + \left[\frac{\omega}{c}\frac{\partial p(\omega)}{\partial \omega} + \frac{\partial g(\omega)}{\partial \omega}\right] = \frac{p(\omega)}{c} \tag{2.84}$$

Interestingly, the two terms in the brackets exactly cancel and the group delay is simply $p(\omega)/c$. In 1988, S.D. Brorson and H.A. Haus showed that this results from Fermat's principle, which states that light takes a path that minimizes its travel time [68]. From this we can easily find the GDD and TOD of the grating pair, where it is generally express in terms of wavelength,

$$GDD = -\frac{m^2\lambda^3 L}{\pi c^2 d^2}\left[1 - \left(-m\frac{\lambda}{d} - \sin\theta_i\right)^2\right]^{-3/2} \tag{2.85}$$

$$TOD = -\frac{3\lambda}{2\pi c}\frac{1 + \frac{\lambda}{d}\sin\theta_i - \sin^2\theta_i}{1 - \left(\frac{\lambda}{d} - \sin\theta_i\right)^2} \cdot GDD \tag{2.86}$$

The grating pair always generates a negative GDD, that is proportional to the grating normal separation L, due to the "red" components diffracting at a larger angle than the "blue" components forcing them to take a longer path length. To eliminate the spatial chirp that is generated by the grating pair, compressors are generally operated in a four-grating or double-pass arrangement.

2.6.2 Pulse stretchers

In the first implementations of CPA, pulse stretching was done by sending the pulse into an optical fiber where the material dispersion would generate a positive temporal chirp on the pulse. However, the higher-order dispersion terms from the material dispersion are not exactly canceled out by the higher-order terms of a grating compressor limiting the final pulse duration achievable. In 1987, O. Martinez found that placing a telescope between two anti-parallel gratings generates the opposite dispersion of the parallel grating pair [69].

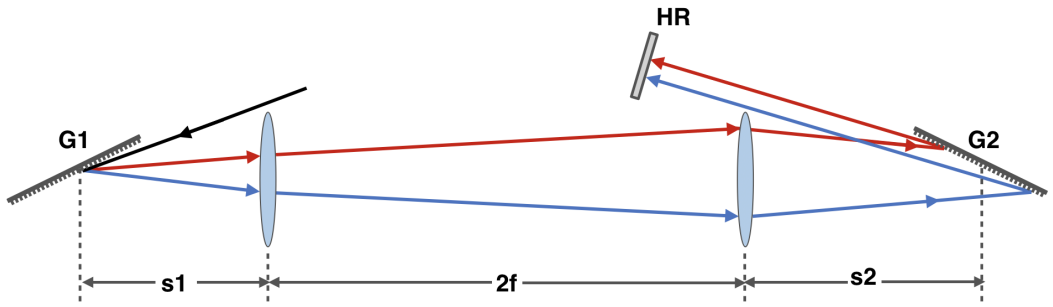

Figure 2.18: Diagram of a Martinez stretcher.

Here, the two lenses, of focal length f, are separated a distance exactly $2f$ away from one another. Each of the gratings is a distance $s_1, s_2 < f$ from the nearest lens. This acts to create a virtual image of the beam hitting the first grating a distance $2f - s_1 - s_2$ behind the second grating. This arrangement acts as the inverse of the grating pair generating a positive GDD on the spectral pulse with $L = 2f - s_1 - s_2$.

The first stretchers were built using lenses as the telescope focusing optics in a $4f$ arrangement. However, this design suffered from the chromatic abberation of the refractive optics making it difficult to achieve TFL pulse durations sub-100 fs after compression. Later designs used all reflective optics for the telescope allowing for TFL pulse durations down to 20 fs [70]. However, the $4f$ telescope still suffered from an astigmatism, which lead to a stretcher design using an Offner telescope formed by two concave and one convex mirrors [71].

2.6.3 Amplification effects in CPA

Amplification of a temporally stretched, broadband pulse presents some unique gain characteristics compared to narrowband amplification.

Gain narrowing

In Section 2.3.1 a formalism of the energy level linewidth was shown in Eq. (2.34) that shows the is not a discrete delta function but has a Lorentzian shape. In solid-state gain media interaction of the lasing ion with the host medium broadens this line. This in turn has an effect on the shape of the emission cross section. For any particular solid-state gain medium there is generally a primary emission cross section peak where lasing occurs that can be fitted with a Lorentzian or Gaussian function. The frequency that is associated with this peak will experience higher gain than the frequency sidebands. As the pulse is amplified this acts to effectively narrows the FWHM of the pulse spectrum, and in doing so increases the duration of the FTL temporal pulse. In ultrafast lasers this is countered by sculpting the spectrum so the input pulse has higher spectral content on the wings than on center.

Gain saturation

The concept of gain saturation in narrowband lasers was discussed in Section 2.3.2. In broadband pulse amplification gain saturation will result in a pulse distortion if left uncompensated. For a broadband pulse amplifying near the saturation fluence of the gain material, the early time components of the pulse will deplete the population inversion, thus lowering the gain, before the later time components arrive. This effect is also dealt with by appropriately sculpting the spectrum prior to amplification. Alternatively, one could shift the center frequency of the spectral pulse so the earlier time component frequencies that see the largest

population inversion also have a lower cross section balancing out the process.

Chapter 3

Chirped pulse juxtaposed with beam amplification (CPJBA)

This chapter has been adapted from a version of record manuscript published in Optics Express with permission under Optica Publishing Group's Open Access Publishing Agreement.

K. D. Chesnut and C. P. J. Barty, "Ideal spatio-temporal pulse distribution for exawatt-sclae lasers based on simultaneous chirped beam and chirped pulse amplification," Optics Express **31**(4), 5687-5698 (2023). https://doi.org/10.1364/OE.480302

3.1 Chirped beam grating pair

In CPA a laser pulse is temporally stretched to reduce the pulse intensity in the amplifier medium. Post amplification, the temporally chirped pulse is compressed with two grating pairs in a traditional four-grating compressor arrangement that induce a negative GDD on the pulse, which is linearly proportional to the normal separation of the two gratings that compose the grating pair [53]. The amount of GDD that can be removed by a grating pair

is limited, in part, by the maximum available grating aperture. In developing the ARC PW laser, LLNL produced high-efficiency, high-damage-threshold multi-layer dielectric (MLD) gratings with a groove density of 1780 lines/mm and angle-of-incidence of 76.5 degrees [54]. Current ARC gratings are ∼0.9 m wide [72], but it is believed the grating manufacturing equipment, used by Plymouth Grating Laboratory and Lawrence Livermore National Lab, can be scaled up to produce two-meter-wide gratings [73]. Horiba France has produced 0.575 m x 1.015 m gratings currently used on the ELI-NP HPLS compressor [17] and 0.66 m x 1.41 m gratings that have undergone experimental demonstration at SIOM [74]. In this paper we presume the availability of 2 m wide by 40 cm tall gratings; however, the argument that follows is valid for any fixed maximum grating aperture size. For large beams, the CPA scheme effectively utilizes only a small fraction of the grating aperture for temporal pulse compression. As illustrated in Fig. 1 below, the grating aperture size, along with the spatial and spectral width of the temporally chirped pulse, are the limiting factors in the maximum normal separation distance between two gratings of a grating pair. The maximum normal separation is given by,

$$L_{max} = \frac{G - \frac{w}{\cos\gamma}}{\tan\theta_r - \tan\theta_b} \tag{3.1}$$

where G is the width of the second grating, w is the input beam width, γ is the input angle to the first grating, and θ_b and θ_r are the diffracted angles of representative blue and red portions of the pulse spectrum respectively. High saturation fluence gain materials, for example Nd:Glass and Yb:Glass, require a highly stretched temporal pulse to extract the full stored energy while avoiding optical damage from B-integral accumulation. Extensive experimental work on high-energy Nd:Glass laser systems has suggested a phenomenological B-integral limit of 3 with an upper limit of 5-6 [75, 76, 77]. The greater amount of stored energy in the amplifier the longer stretched pulse duration required—this is one of the primary reasons high-energy, Nd:Glass laser systems operate at a small portion, around 10%, of their total

stored energy. NIF has shown that a stretched pulse of 23-ns is able to safely extract the full 26-kJ of stored energy in a single amplifier beamline [51]. However, as the stretched pulse duration extends into the nanosecond regime a practical problem emerges; the gratings must be large enough to handle a nanosecond-scale delay between the red and blue components of the spectrum. A delay of 1-ns equates to approximately 30-cm of path difference, and when projected onto a grating at its operating angle-of-incidence (AOI) requires meter-scale grating apertures. For exawatt-class peak-power production, and to utilize the full bandwidth of a Nd:Mixed-glass amplifier, this 20 ns stretched pulse must be compressed to 100 fs. Given the ARC grating design, with a maximum aperture of two meters, and a 37 cm beam width, as is commonly found on large-aperture Nd:Glass lasers [48, 78], a standard four grating compressor can compress, at maximum, a 3.34 ns stretched pulse down to a 100 fs FTL. To accomplish the full compression factor with a standard four grating Tracey compressor and the ARC grating design would require a grating aperture of 5.4-m (height) x 1.6-m (wide) for gratings 1 and 4, and 5.4-m (height) x 6.14-m (wide) for gratings 2 and 3. Supposing a maximum grating aperture of 0.5-m (height) x 2-m (wide), to drop the fluence below the 1 J/cm^2 the tiled grating approach would need 11 x 1 tiled gratings for gratings 1 and 4 and 11 x 4 tiled gratings for gratings 2 and 3—a total of 110, 2-m wide gratings. Each of these gratings has 5 degrees-of-freedom that require nm-scale alignment precision to properly maintain the pulse structure [36, 37, 38].

The compressive effect of a maximum-aperture-limited grating pair can be extended by employing spatial chirp on the input beam. Spatial chirp, as it is commonly defined, is a spatio-temporal distortion that results in the different frequency components of a pulse spatially separated transverse to the direction of propagation [67]. Here, each frequency can be thought of as its own beamlet whose center is determined by the degree of spatial chirp, which yields a function, $x_0(\omega)$, whose derivative with respect to frequency is called the spatial dispersion. Generally, this is created by optics that induce angular dispersion. For example, in Fig. 3.1 above the pulse enters the first grating with all the frequency

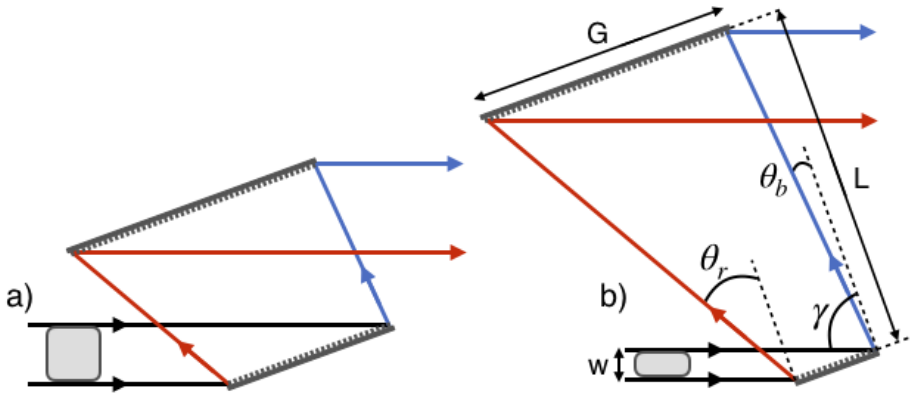

Figure 3.1: Diagrams showing the maximum grating pair separation for a fixed grating aperture for a) a full-width pulse without spatial chirp and b) a half-width pulse without spatial chirp.

components overlapped in space; the first grating imparts angular dispersion to the pulse causing the frequency components to spatially separate, the second grating removes the angular dispersion yet the frequency components remain spatially separated. Consider a grating pair with the half-width beam, shown in Fig. 1b, and separate the two gratings further until the input beam has recovered its original full-width. With the correct direction of input spatial chirp, the red beamlet and blue beamlet will undergo an image inversion as they travel from the first to the second grating, shown below in Fig. 3.2. This enables a larger grating separation for a fixed size of the second grating with a maximum grating separation of,

$$L_{max} = \frac{G - \frac{w(2-\chi)}{\cos(\gamma)}}{\tan\theta_r - \tan\theta_b} \tag{3.2}$$

To normalize the spatial chirp to the beamlet size we introduce the spatial chirp parameter χ that characterizes the total beam width expansion factor. A χ of two represents a spatial chip resulting in a beam width twice the original width (i.e. the centers of the red beamlet and blue beamlet are separated by the original beam width, $x_0(\omega_r) - x_0(\omega_b) = w$. For this spatial chirp the maximum separation of the grating pair is not limited by the input beam width but only by the size of the second grating aperture and the spectral bandwidth of the

pulse. This allows for larger negative GDD to be generated by the grating pair for a fixed second grating aperture. For example, we consider grating pair with maximum aperture of 2 m, a groove density of 1780 lines per mm, and an input beam at an AOI of 76.5 degrees. With a blue wavelength of 1040-nm and red wavelength of 1080-nm, a 37-cm wide non-spatially chirped beam will generate a GDD of -3.49e7-fs^2 in this grating pair. Meanwhile, a 18.5-cm beam that is spatially chirped with a χ of two (i.e. a total beam width of 37-cm) can generate -1.83E8-fs^2 in the same grating pair—a 425% increase in GDD removed for a single grating pair.

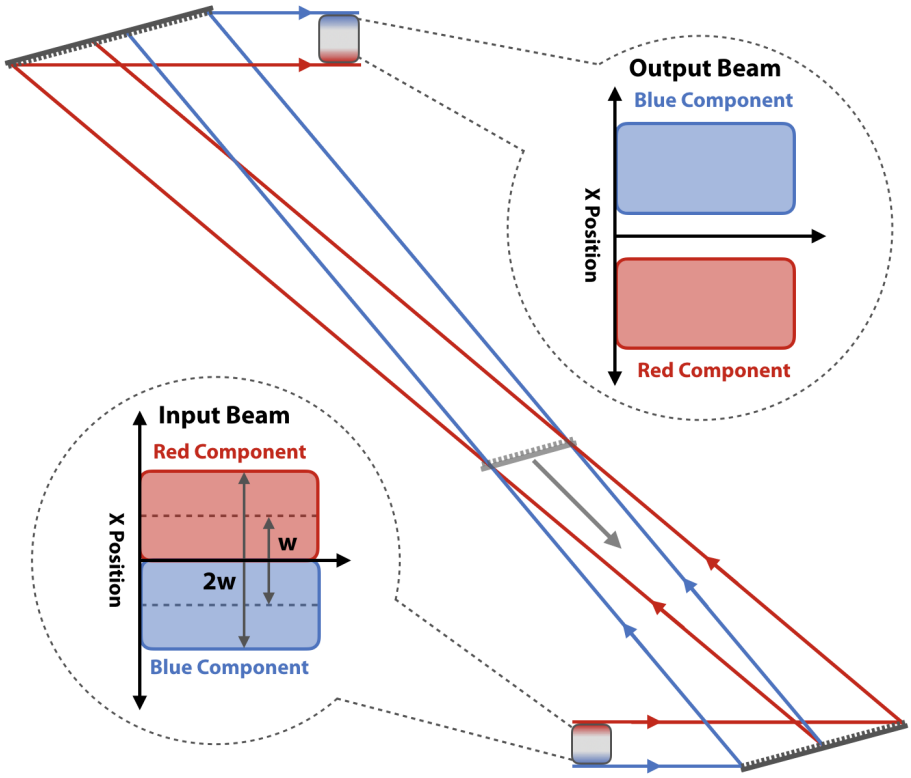

Figure 3.2: Illustration of a chirped beam grating pair created with a a spatially chirped pulse with a χ of two and full-width composed of half-width beamlets

3.2 Six-grating compressor

CPJBA allows for highly efficient temporal compression of large-aperture beams with a novel six-grating compressor shown below in Fig. 3.3. Here, two chirped beam-pulse grating pairs perform a majority of the temporal compression but leave the spatial chirp unchanged. The chirped beam-pulse then enters a final grating pair that removes the spatial chirp and performs the remaining amount of temporal compression. In this way, one can compress a 20-ns stretched pulse down to its 100-fs FTL using ARC gratings with a maximum aperture of two meters. As mentioned previously, the final grating has a finite damage threshold, of approximately 1-J/cm^2 at 100-fs [55, 56], and cannot handle the full power. Instead, through a careful arrangement of beam splitters, the chirped beam-pulse is split into multiple identical beamlet copies prior to total temporal compression by as many final grating pairs—this effectively increases the aperture of the final grating reducing the fluence seen on the final optic. Since the beamlets all originate from the same amplifier there is a single wavefront distortion to correct for, and all beamlets will be identical as far as the beam splitters and final gratings can be made identical. In contrast to the tiled grating approach, the CPJBA six-grating compressor involves only two, 2-m aperture gratings as most of the gratings are 1.6-m or 0.8-m wide, has lower complexity alignment, and does not require masking the beam.

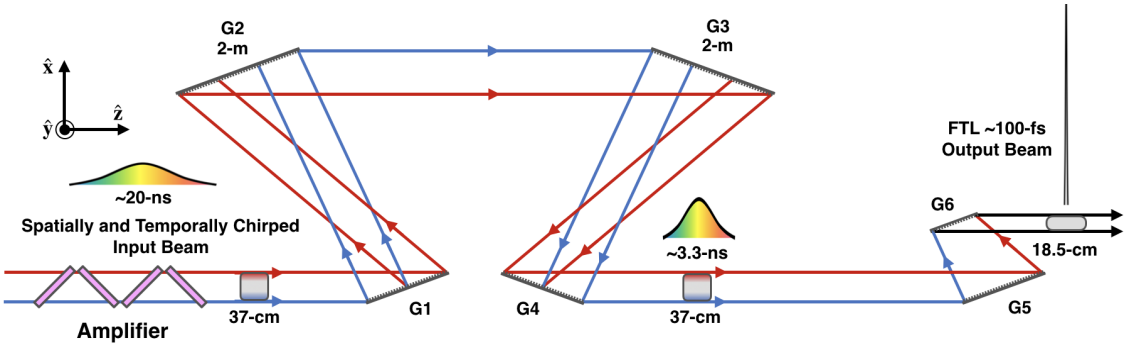

Figure 3.3: Schematic of the six-grating compressor for CPJBA designed to compress a 37 x 37 cm aperture simultaneously spatially and temporally chirped 20 ns pulse down to an 18.5 x 37 cm aperture 100 fs Fourier transform-limited pulse.

The modeled beam is an 8th-order super-Gaussian spatial distribution with a 37-cm diameter at 1% peak fluence. This is consistent with the main laser beam in NIF that has a 37.2-cm diameter at 0.1% peak fluence [47]. The spectral pulse, shown below in Fig. 3.4, is also an 8th-order super-Gaussian centered at 1060 nm with a FWHM of 30.2-nm, producing a sinc^2-like temporal pulse with a Fourier transform-limited FWHM of 100-fs. The red-most and blue-most spectral components are defined by the spectral components that constitute 1% of the peak spectral power. Cutting off the spectral distribution at these points has minimal effect on the temporal pulse distribution.

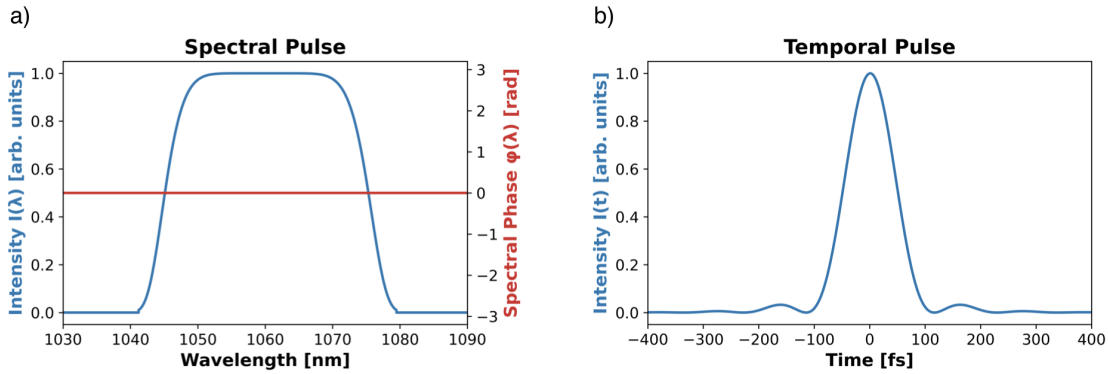

Figure 3.4: Output of the CPJBA six-grating compressor. a) 8th-order super-Gaussian spectral distribution of the pulse centered at 1060-nm with a FWHM of 30.2-nm and b) the Fourier transform-limited temporal pulse of the spectral distribution with a FWHM of 100-fs.

Given a beam aperture from a NIF-like amplifier of 37-cm x 37-cm and an AOI of 76.5 degrees gratings G1 and G4 need to be 1.6-m wide. With a maximum producible grating width of 2-m, grating pairs G1-G2 and G3-G4 can have a maximum separation, along the direction normal to the grating faces, of ∼1.914-m while not clipping any spectral content. The output beam from the six-grating compressor has a width of 18.5-cm in the direction of grating dispersion giving the final grating G6 width of 0.8-m. For full containment of the spectrum this allows for a maximum separation between G5 and G6 of ∼0.780-m in the direction normal to the grating faces. The full geometry is summarized below in Table 3.1. In this six-grating compressor set-up there is a total grating separation of 4.608-m. This

same grating design in a standard CPA scheme is not able to handle the spectral bandwidth required for a 100-fs pulse. As shown in Eq. 3.1, as the spectral bandwidth increases the maximum allowable grating separation decreases; for a pulse with the spectral and spatial properties outlined above, the grating separation of G1-G2 is small enough that the second grating will physically clip the incoming beam in a standard CPA arrangement.

Grating	X-Aperture	Y-Aperture	Norm. Separation	Transv. Separation
G1	1.6-m	0.4-m	-	-
G2	2.0-m	0.4-m	1.914-m	4.665-m
G3	2.0-m	0.4-m	-	-
G4	1.6-m	0.4-m	1.914-m	4.665-m
G5	1.6-m	0.4-m	-	-
G6	0.8-m	0.4-m	0.780-m	1.902-m

Table 3.1: Geometry of the six-grating compressor.

The arrangement shown in Fig. 3.3 still does not address the intensity damage problem on the final grating. To drop the fluence below the damage threshold of the gratings the pulse is split into 30 identical copies before entering the final grating pair. Correctly phasing together the 30 beams requires a beam splitter arrangement, shown below in Fig. 4., that imparts an equivalent amount of dispersion to each pulse copy by having each beamlet experience the same number of transmission events. After the final grating pairs, the identical beamlets are coherently combined using a tiled, parabolic mirror array. Similar to the construction of large aperture telescopes [59], this optical system allows for the construction of a large, low f-number focusing mirror composed of multiple smaller, moderate f-number mirror segments. Here, each beamlet is incident on an individual segment of the parabolic mirror, whose piston and tip-tilt is controlled by three piezo actuators. By producing identical beamlets from a single aperture, the task of phasing multiple beams together is considerably simpler than combining multiple, separate amplifier beam lines.

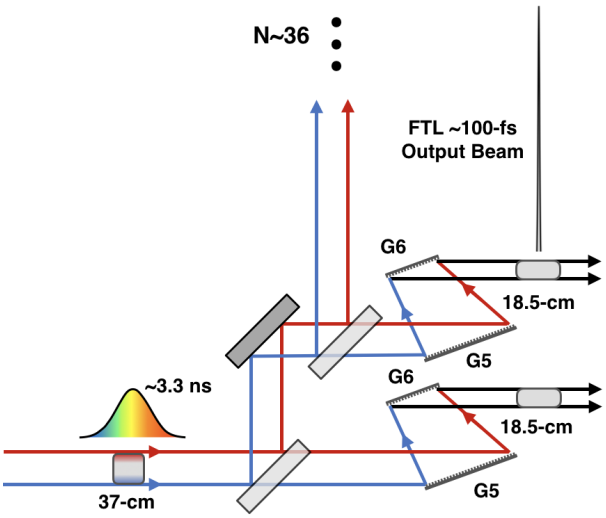

Figure 3.5: Unit cell of a dispersion balanced beam splitter arrangement that can be repeated to split the beam into N identical copies. Each beamlet undergoes one transmission event in a beam splitter to ensure equal dispersion for each copy.

3.3 Analysis of pulse spatio-spectral and spatio-temporal structure

To determine the ideal spatio-spectral and spatio-temporal structure of the pulse that can be compressed by the six-grating compressor to a ∼100-fs FTL pulse, we back-propagated the FTL pulse through the compressor and analyzed the beam-pulse structure at the input to the full six-grating compressor. This ray trace model was done with LightTrans' Virtual Lab Fusion [79]. In the ray tracing software an analysis plane records the spatio-spectral amplitude and phase of each frequency component in the pulse. With this we can create a 2D heat map of the pulse spatio-spectral structure to quantify the spatial chirp present in the beam, shown below in Fig. 3.6. Horizontal lineouts of the 2D map represent the spectral content at that transverse beam position (see Fig. 3.3 for the coordinate system). The asymmetry of the spectral content across the transverse beam center is a result of the diffracted angle of each beamlet, given by the grating diffraction equation, being nonlinear with respect to wavelength.

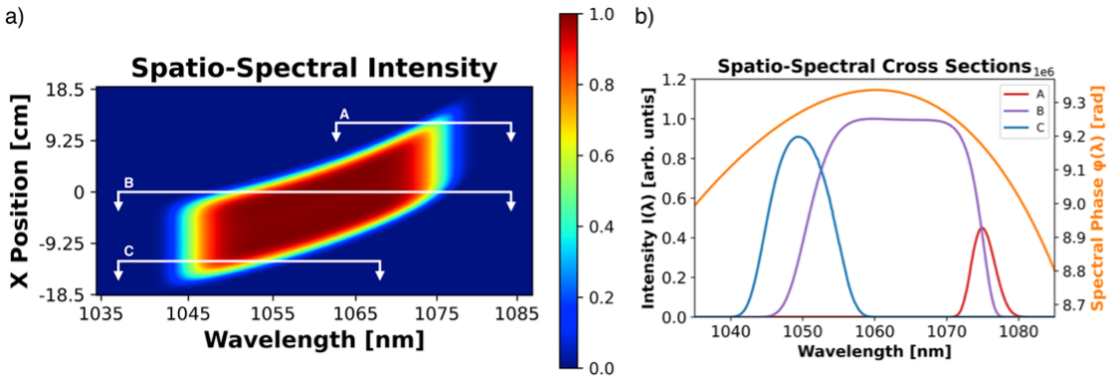

Figure 3.6: The spectral cross-section of the beam changes with position along one of the beam's transverse axes. (a) 2D heatmap of the spatio-spectral pulse that is compressed by the six-grating compressor and (b) the spectral content and phase of the pulse at various beam transverse positions: 12.5 cm (A), 0 cm (B), and -12.5 cm (C).

Performing a line-by-line Fourier transform across the transverse beam width on the spectral pulse ascertains the full spatio-temporal pulse structure. Due to the high spectral frequency resolution needed for the large stretch factors involved, the Fourier transform was performed by a post-processing Python script [80]. A form of this hybrid ray tracing and numerical analysis technique was used by Laboratory for Laser Energetics to analyze the pulse structure from a tiled grating pulse compressor [81]. Below, in Fig. 3.7, the horizontal lineouts in the 2D spatio-temporal heat map give the pulse duration at each transverse cross-section of the beam. The spatial chirp results in a non-uniform pulse duration distribution along the spatial transverse axis of the beam. The maximum pulse duration FWHM is 18.9-ns at x-position 1.5-cm. The edges of the beam, while having a shorter pulse duration, have reduced energy content keeping the intensity low.

3.3.1 Higher-order phase effects

Clearly seen in Fig. 3.7(a) is an asymmetric temporal pulse structure that is due to the appreciable amount of third-order dispersion (TOD) removed by the compressor system; this is a natural consequence of any grating-based compressor. The substantial TOD reduces the

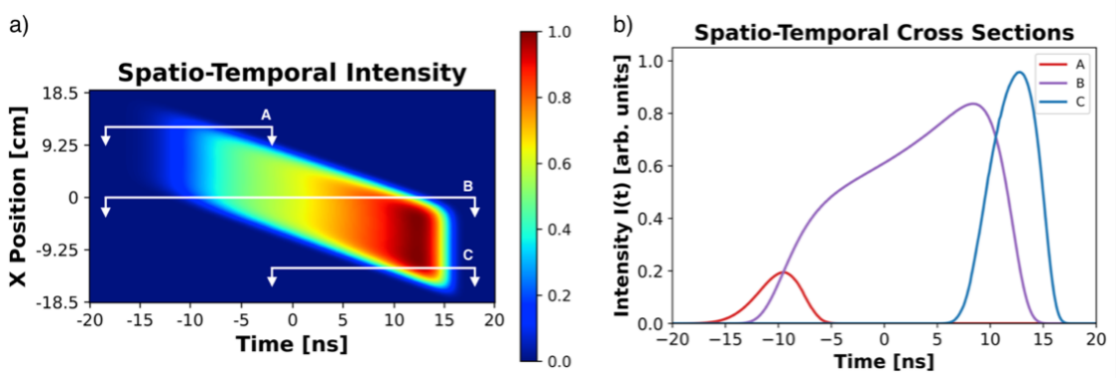

Figure 3.7: Due to the changing spectral content along the one of the beam's transverse axis the temporal cross-section changes as well. (a) 2D heat map of the spatio-temporal structure of the pulse intensity that is compressed by the six-grating compressor and (b) the temporal cross-sections of the pulse at beam transverse positions 12.5 cm (A), 0 cm (B), and -12.5 cm (C) with FWHM pulse durations of 6.0 ns, 18.2 ns, and 4.6 ns respectively.

effective pulse duration and can lead to increased B-integral accumulation in the amplification chain under full energy extraction conditions. This TOD effect should be minimized as much as possible to flatten the temporal cross-section and reduce the B-integral allowing for greater energy extraction from the amplifier.

The shortest possible FTL output pulse duration is desirable for building a high-peak-power laser. However, longer duration FTL output pulses may be useful for applications such as narrow bandwidth laser-Compton scattering and pumping OPCPA systems [44]. A longer FTL pulse duration equates to a smaller spectral bandwidth allowing for a larger grating separation for a fixed aperture grating pair. This modifies the spectral phase distribution that is removed by the compressor, which can be approximated as a Taylor series about the center frequency given by,

$$\phi(\omega) \approx \phi_0 + GD(\omega - \omega_0) + \frac{1}{2}GDD(\omega - \omega_0)^2 + \frac{1}{6}TOD(\omega - \omega_0)^3 + \cdots \tag{3.3}$$

Here, ϕ_0 is the total phase of the center frequency, ω_0 is the center frequency, GD is the group delay, GDD is the group delay dispersion, and TOD is the third order dispersion. This phase function is fit to the spectral phase output from LightTrans to determine the GDD

and TOD induced by the six-grating compressor. Table 3.2 details the maximum grating pair separation, the on-beam-center input pulse FWHM duration, as well as the GDD and TOD induced by the compressor configuration for various output FTL pulse durations.

TFL Pulse FWHM [fs]	Stretched Pulse FWHM [ns]	G1/G2-G3/G4 [m]	G5/G6 [m]	GDD [fs^2]	TOD [fs^3]
100	18.2	1.914	0.780 m	-4.65E+08	9.04E+09
200	20.6	4.178	1.704 m	-1.01E+09	2.03E+10
500	21.1	10.684	4.356 m	-2.57+09	5.01E+10
1000	20.7	21.365	8.715 m	-5.14+09	9.96E+10

Table 3.2: Geometry of the six-grating compressor.

While the TOD term increases linearly with pulse duration, its effect on a spectral component's phase decreases to the third power with an increase in pulse duration due to the decreased spectral bandwidth. Fig. 3.8, below, clearly shows this reduction of the TOD effect on the spatio-temporal intensity distribution as the pulse duration increases, which manifests itself as a temporal asymmetry.

An alternative route to modify the spatio-temporal distribution is to sculpt the spectral content of the pulse. Shown below in Fig. 3.9(b) is a modified spatio-temporal distribution resulting from a simple spectral sculpting, seen in Fig. 3.9(a). While the spectral sculpting has a precipitous effect on the spatio-temporal distribution, the effect on the FTL pulse duration and structure, plotted in Fig. 3.9(c) and (d), is minimal with the sculpted spectrum having a FTL FWHM of 100-fs. In this manner one can preserve the short duration FTL output pulse while removing any temporal spikes that would cause excessive B-integral accumulation in the amplifier. The sculpted spectrum in Fig. 3.9(a) is the full power spectrum of the pulse after it has been amplified and spatial chirp removed by the six-grating compressor.

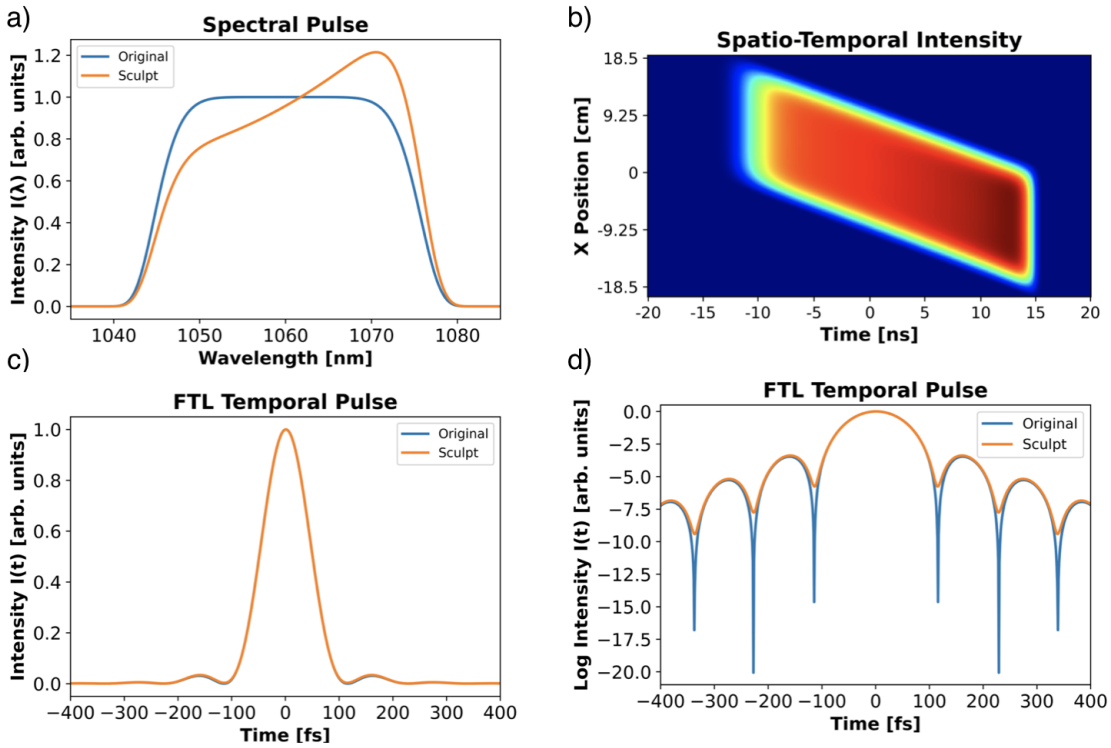

Figure 3.8: Spectrum of a sculpted pulse contrasted with the original non-sculpted spectrum. (b) The spatio-temporal profile of the sculpted pulse prior to entering the six-grating compressor. The resulting Fourier transform-limited temporal pulses of the sculpted and original spectrum (c) along with a log plot of the FTL temporal pulses (d).

Chapter 4

Amplification of spatially and temporally chirped beams

4.1 Modeling amplification of temporally and spatially chirped beams

CPJBA is unique in its amplification of a highly-temporally-stretched, spatially chirped beam. An amplification model capable of handling a custom spatio-temporal field was developed to demonstrate these effects. The amplification model is based on a numerical implementation of the Frantz-Nodvik solution, which describes the gain dynamics of a square shaped temporal pulse in an amplifier [64]. This solution is extended to temporal pulses of arbitrary shape by modeling them as a collection of discrete square pulses of width Δt and varying amplitude [82]. The square pulses are treated consecutively by the Frantz-Nodvik solution, Eq. (4.2), with each modifying the remaining population inversion and, thus, the gain that the subsequent experiences, Eq. (4.3). Due to the high temporal stretch factor, each unit of time in the pulse corresponds to a different wavelength with a different emission

cross section in Nd:APG-1. Thus, each of our square pulses in time will have a different small-signal gain and gain saturation. The group delay of each wavelength is calculated from the spectral phase of the pulse that is compressed by the six-grating compressor. This correlates each of the discrete square temporal pulses with the correct spectral wavelength. Due to the spatial chirp the gain effects need to be considered transversely across the beam as well. This is done by breaking the beam and amplifier medium into a transverse grid, with spacing Δx, and recording the beam energy and population inversion along this coordinate.

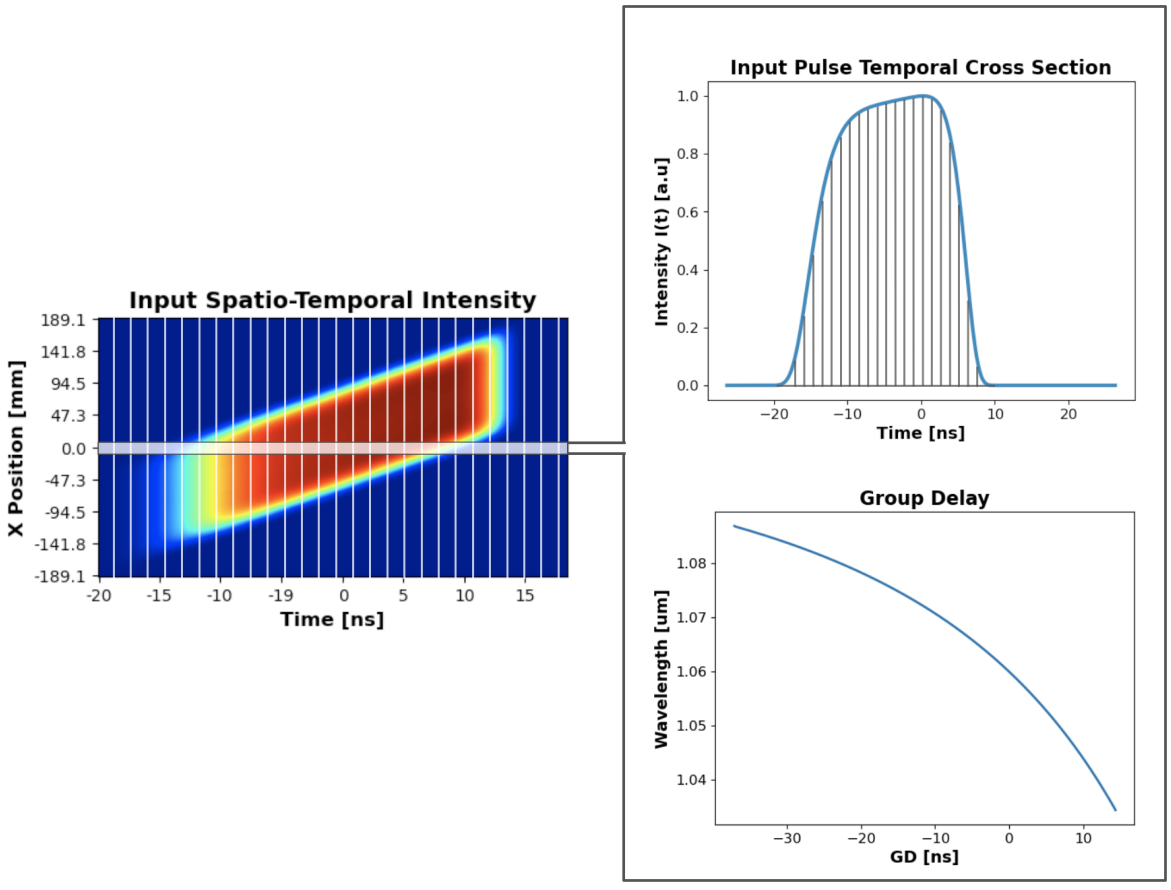

Figure 4.1: Example of a cross section of the spatio-temporal pulse taken at x=0 showing the temporal pulse broken into segments of width Δt along with the associated group delay that maps the time coordinate to a particular wavelength.

The amplification code iterates through the spatial dimension of the input pulse applying the discretized Frantz-Nodvik solution that is modified according to the population inversion in the amplifier at the corresponding x-position. We define the coupled gain and population

inversion equations with spatial dependence as,

$$E_{out}(x,t) = E_{in}(x,t)G(x,t) \tag{4.1}$$

$$E_{out} = E_{sat}\ln\{1 + [\exp(\frac{E_{in}(x,t)}{E_{sat}(t)}) - 1]\exp[N(x,t)\sigma(t)L]\} \tag{4.2}$$

$$N(x,t+1) = N(x,t) - [E_{out}(x,t) - E_{in}(x,t)]\frac{1}{L} \tag{4.3}$$

Here, $E_{out}(x,t)$ and $E_{in}(x,t)$ are the beam output and input energy respectively, $E_{sat}(t)$ is the saturation fluence of the pulse, $N(x,t)$ is the population inversion, $\sigma(t)$ is the emission cross section, and L is the length of the amplifier. As stated previously, since the emission cross section is wavelength dependent it varies in time due to the chirped pulse nature of the beam. This in turn causes a time dependence of the saturation fluence, which is defined as the photon energy divided by the emission cross section. In our simplified model we ignore amplified spontaneous emission, transient pumping effects, thermal gain effects, and phase distortion from the atomic phase shift in the amplifier.

From the LightTrans model of the six-grating compressor the analysis plane collected the 2D spatio-spectral amplitude that contains information about the spatial chirp, Fig. 3.6, as well as the spectral phase of the stretched pulse that can be compressed by the six-grating chirped beam compressor. As mentioned in Section 3.2, a post-processing script in Python produced the spatio-temporal field via a line-by-line Fourier transform. This spatio-temporal intensity grid has 200 points in the spatial dimension and 500 points in the temporal dimension. The amplifier was also broken up into a transverse grid of 200 points and initialized with a starting population inversion $N(x, t = 0)$. The cross section data for Nd:APG1 was digitized from G.R. Hays et al. [52]. At each x-position the amplification code works as follows: (i) an array the length of the time grid coordinate is generated from the x-position of the spatio-temporal grid, (ii) starting at the first index value of the array (corresponding to the earliest time t=0) the input fluence E_{in} is calculated from the array

value, with units W/cm^2, multiplied by the time grid width Δt, (iii) the saturation fluence at that time position, $E_{sat}[t]$, is calculated from the corresponding frequency and emission cross section for that time position mapped from the group delay (iv) the small-signal gain for this time position is calculated using the population inversion density in the amplifier at that spatial coordinate and the emission cross section for the current time position, (v) the new fluence of this time position is calculated from the original fluence and saturation fluence using the Frantz-Nodvik solution, (vi) the population inversion density of the spatial coordinate is modified according to the difference in the amplified and input fluence, (vii) the code then iterates to the next time array position and repeats.

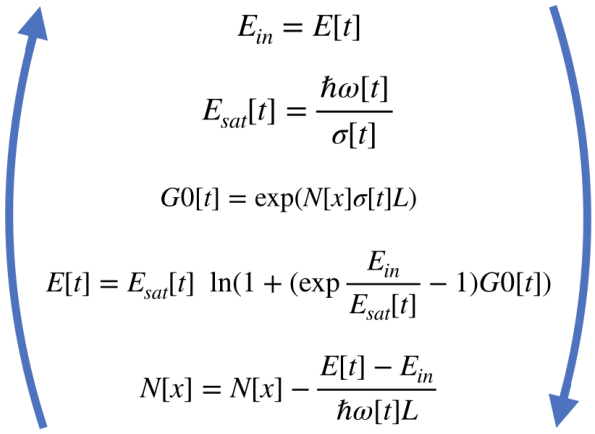

Figure 4.2: Diagram of the amplification code loop that occurs at each spatial position across the transverse dimension (x-position) of the spatio-temporal input pulse.

To calculate the B-integral, defined in Eq. (4.4), the total length, L, of the amplifier is divided into sections of length Δz. Here, the Δz length is ~1-cm. This is to capture the changing intensity of the pulse as it travels through the amplifier medium. At each section Δz of the amplifier the local peak intensity is used to generate that segments contribution to the B-integral,

$$B = \frac{2\pi}{\lambda} n_2 \int_0^L I(z)\, dz = \frac{2\pi}{\lambda} n_2 \sum_{z=0}^{z=n} I_{peak,z} \Delta z \tag{4.4}$$

As described in Section 2, the output pulse spectrum is an 8th-order super-Gaussian en-

velope, to avoid clipping on the gratings or amplifier, centered at 1060-nm with 30.2-nm FWHM—this will produce a 100-fs FWHM transform limited $sinc^2$ temporal pulse. Spatially, each beamlet emerging from the six-grating compressor is a rectilinear, 8th-order super-Gaussian with a width of 18.5-cm and height of 37-cm. A 2x spatial chirp, induced prior to the six-grating compressor and amplifier, produces a 37-cm x 37-cm beam, which is comparable to the aperture size of most high-energy Nd:glass lasers [48, 78]. The input pulse energy is set to 40-J to match the previous energetics study on high-energy, broadband Nd:Mixed-glass amplifiers [52]. The amplifier system is modeled after the architecture of a single NIF beam line with a four-passed main amplifier (MA) and double-passed power amplifier (PA)—the PA is passed through once before and once after the four passes on the MA [78]. All slabs are composed of Nd:APG-1, each 4-cm thick with an on-beam aperture of 37-cm x 37-cm and a Nd doping concentration of 4.22E20-ions/cm^3 [83]. Pulse amplification depends only on the total stored energy and is agnostic to the total path length in the amplifier insofar as energy is concerned. The total number of slabs will modify the amplified spontaneous emission (ASE) and B-integral [84, 85], while not affecting the amplified pulse structure. We will initially consider the "11-7" configuration—eleven MA slabs and seven PA slabs [78].

4.2 CPJBA amplification effects

To illustrate the CPJBA amplification effects, the spatio-temporal distribution shown in Fig. 3.7(a), with a total energy of 40-J, is sent into the amplifier. Using a flat initial gain distribution in the amplifiers, Fig. 4.4(a), with an initial stored energy of 22.7-kJ in the MA and 14.445-kJ in the PA for an even energy per slab for the 11-7 configuration, will amplify the chirped beam-pulse to 25-kJ with the resulting spatio-temporal distribution shown below in Fig. 4.3(a). This corresponds to a total stored energy of 37.145-kJ and an efficiency of

67.3%. The output exhibits significant pulse distortions from the desired amplified pulse due to a combination of gain narrowing and gain saturation. Both effects are ubiquitous to broadband, high-gain amplification; however, they have a unique presentation in CPJBA. Gain narrowing, a process where the spectral components at the peak of the emission cross section curve experience higher gain than the spectral wings [86], results in a lack of pulse content at the temporal edges of the amplified pulse in Fig. 4.3(a). This causes the FWHM pulse duration at the middle of the beam to be reduced from 20.6-ns to 9.3-ns as shown below in Fig. 4.3(c). Temporal pulse distortion due to gain saturation is a well-known phenomenon in CPA laser amplifiers [87, 88]. When operating near the saturation fluence of the gain media, the leading edge of the temporal pulse will deplete the population inversion of the amplifier before the trailing edge arrives, experiencing higher gain and distorting the temporal pulse shape.

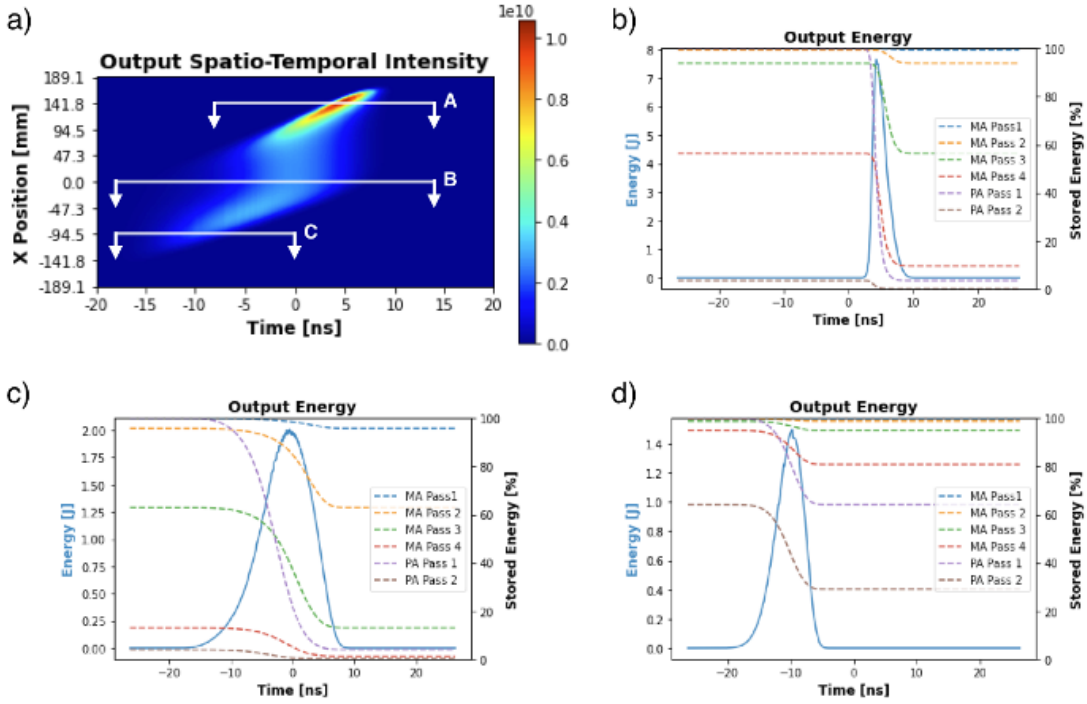

Figure 4.3: (a) Spatio-temporal intensity distribution in units of W/cm2 of the amplified 25-kJ output pulse (b) Cross section A at x=160-mm with a FWHM duration of 2.2-ns (c) Cross section B at x=0-mm with a FWHM duration of 9.3-ns (d) Cross section C at x=-95-mm with a FWHM of 5.5-ns. The dashed lines indicate the temporal evolution of the stored energy of both the Main and Power Amplifier slabs on each pass.

In CPJBA, the spatial chirp induces a spatial dependence on the temporal position of the leading edge. Now, the spectral components at the emission cross section peak are exposed to the full stored energy in the amplifier, and hence gain, before the spectral components with lower emission cross section can deplete it. Along with the spatial energy distribution of the pulse, this leads to a varying effective gain across the transverse profile of the beam producing the asymmetric amplified pulse energy fluence distribution seen below in Fig. 4.4(b). Since the spatial edges of the beam have a reduced FWHM pulse duration, an intensity hot spot develops on the leading-edge side of the beam corresponding to the temporal position of the 1053-nm component of the pulse spectrum (i.e., the emission cross section and gain maximum). This results in a large B-integral accumulation, shown below in Fig. 4.4(d), at the spatial position of the intensity hot spot with a peak of 17.75.

The temporal and spatial pulse distortion effects present in CPJBA due to amplification can be compensated by appropriately shaping both the input pulse and transverse gain distribution in the amplifier. This gain saturation effect is compensated by appropriately sculpting the spectrum of the input pulse to the amplifier, skewing the input power spectrum to the shorter wavelength components [88]. In the Nexawatt system, spectral sculpting can be accomplished in the broadband OPCPA stage. The temporal distribution of the spectrum in this highly stretched 20-ns pulse allows one control the gain of the different spectral components by modifying the temporal shape of the pump pulse [89, 90]. This is readily achieved with current multi-Joule, ns-duration narrowband lasers and low-capacitance (i.e., fast switching) electro-optic cells. While this technique can perform the bulk of the spectral shaping, with a single Pockels cell supporting >5000:1 extinction ratio, this will only permit a single spectral sculpting shape across the entire spatial extent of the beam. However, there are a number of 2D pulse shaping methods to fine tune the spatio-spectral distribution of the input pulse to the amplifier (i.e., a unique spectral sculpt profile at different transverse spatial positions on the beam) [91, 92]. These 2D pulse shapers take the traditional 4f pulse shaper, essentially a Martinez stretcher with $s_1 = s_2 = f$ and an amplitude modulator at

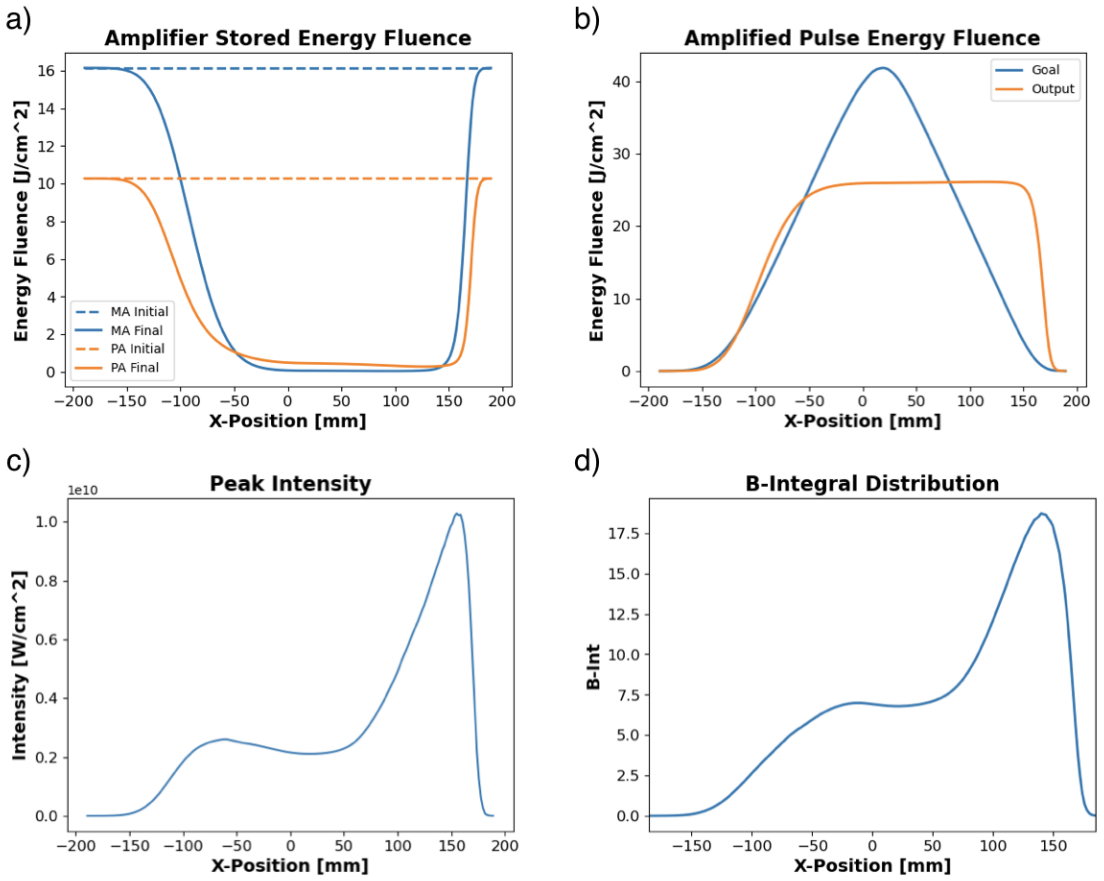

Figure 4.4: Spatial distribution of a) initial and final stored energy fluence in the MA and PA, b) the amplified pulse fluence comparing the base case input pulse output to the goal amplified pulse, c) peak intensity of the amplified output pulse, and d) the total accumulated B-integral during amplification.

the Fourier plane between the two lenses, and replace the 1D amplitude modulator with a 2D device such as a diffractive optical element (DOE) or digital micromirror device (DMD). This enables the spectral content of the pulse to be modulated along one of the transverse coordinates of the beam.

The spatial pulse distortions during amplification can be addressed by two different methods—spatial shaping the beam prior to amplification and spatially varying the gain within the amplifier. The Pre Amplifier Modules (PAMs) on NIF incorporate a programmable spatial shaper (PSS) that is composed of a system of specialty spatial light modulators, which allows for the blocking of portions of the low-fluence beam that correspond to the location of

damage sites that are present on the downstream optics [78]. This system has demonstrated an attenuation factor of OD 2 with mm-scale spatial resolution and extension to OD 5 is reasonable. In addition to the PSS, NIF also incorporates a static spatial mask prior to the main amplifier to account for the non-uniform small-signal spatial gain profile [93, 94]. The easiest way to modify the spatial gain profile in the amplifier slabs is to shape the spatial profile of the pump fluence. The flash lamp pumps on the main amplifier slabs of NIF utilize a carefully designed, multi-curved reflector to distribute the pump energy more evenly, producing a more spatially uniform small-signal gain [78]. For CPJBA, the desired spatial gain profile can be made nonuniform to compensate for the spatial pulse distortions. Moving to a diode pump source, as is common with current high-intensity Nd:glass lasers [50, 85], will allow for greater control over the spatial distribution of the gain profile.

4.3 Nexawatt amplification

Conveniently, the Frantz-Nodvik solution is reversible [78]. This allows one to specify the remaining stored energy in the amplifier and the desired amplified output pulse to obtain the ideal input pulse and initial stored energy. The inverse Frantz-Nodvik solution takes the form,

$$E_{in}(x,t) = \frac{E_{out}(x,t)}{G(x,t)} = E_{sat} \ln \{1 + [\exp(\frac{E_{out}(x,t)}{E_{sat}(t)}) - 1] \frac{1}{\exp[N(x,t)\sigma(t)L]}\} \tag{4.5}$$

$$N(x,t-1) = N(x,t) + [E_{in}(x,t) - E_{out}(x,t)] \frac{1}{L} \tag{4.6}$$

The desired output spatio-temporal intensity distribution, scaled to 25-kJ fin Fig. 4.5(b), is a fixed input, while the spatial distribution of the remaining stored energy in each amplifier section, post-amplification, is a free variable. Each supplied final energy distribution results in a unique, ideal spatio-temporal pulse input and initial stored energy distribution. Op-

timization is contingent on real-world design constraints, which are currently not material, and this section seeks, instead, to demonstrate the amplification dynamics.

We first consider the case of a flat final stored energy distribution, Fig. 4.5(d), with remaining energy split between the MA and PA at a ratio that produces approximately the same initial energy per slab in both the MA and PA for the "11-7" amplifier configuration. The total remaining energy determines the input pulse energy, a lower amount of remaining stored energy in the amplifier (i.e., more efficient energy extraction) requires a higher input pulse energy. Here it is set to 10.4-kJ to give an input pulse energy of 40-J, which is commensurate to previous studies on potential exawatt-class Nd:glass lasers [52]. Using this final stored energy distribution of the amplifier and back-propagating the desired amplified output pulse using the inverse Frantz-Nodvik solution produces the input pulse spatio-temporal distribution, Fig. 4.5(a), as well as the initial stored energy distribution in the amplifiers, shown below in Fig. 4.5(c). This input pulse, in combination with the initial stored energy distribution, will result in the amplified spatio-temporal output pulse distribution shown in Fig. 4.5(b). The initial stored energy distribution has a total energy of ∼36.76-kJ for an efficiency of 68.0%, and is free of any high-frequency spatial modulations allowing for gain shaping with a diode pump source. In addition to producing a nearly ideal amplified output pulse, this arrangement has a peak B-integral value of ∼3.5 with a relatively flat spatial distribution—well within the acceptable limits of large-aperture Nd:glass lasers. While the spatio-temporal distribution of this input pulse is quite different than pulse structures normally used during amplification, Fig. 4.6(a-g) below show how the pulse evolves during the various passes through the MA and PA culminating in the desired amplified output pulse spatio-temporal distribution.

One can control the input pulse spatio-temporal profile by modifying the remaining stored energy spatial distribution in the amplifier. Increasing the amount of remaining stored energy at a particular transverse position in the amplifier will decrease the necessary energy of the

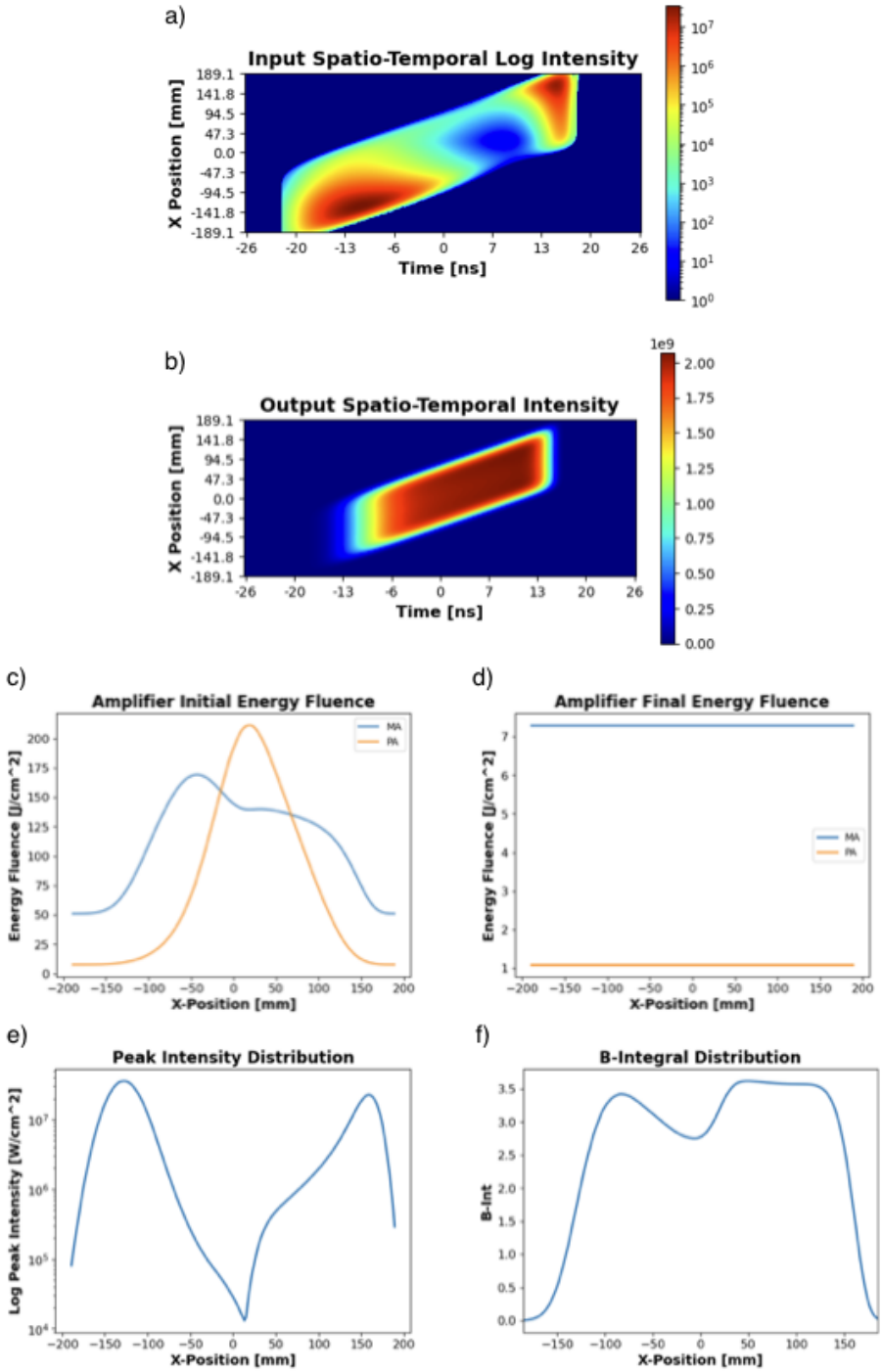

Figure 4.5: The first case of a flat distribution of remaining stored energy in the MA and PA. a) Log intensity of the 40-J input pulse spatio-temporal profile that produces b) the amplified 25-kJ output pulse spatio-temporal profile. The spatial distribution of c) the initial stored energy fluence in the MA and PA, d) the final stored energy fluence in the MA and PA after amplification, e) peak intensity of the input spatio-temporal pulse, and f) total B-integral accumulated during amplification.

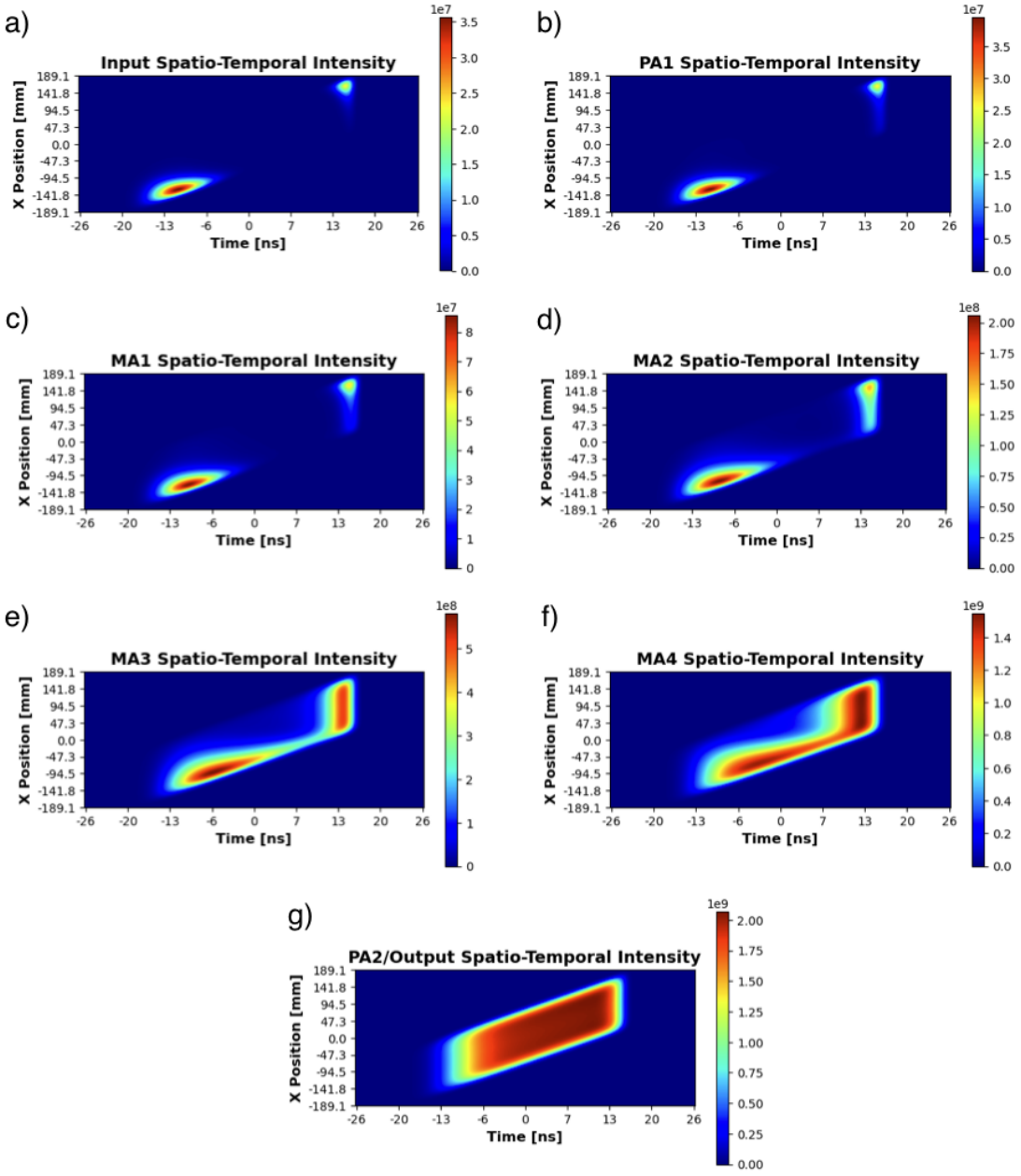

Figure 4.6: Evolution of the spatio-temporal pulse distribution during amplification given the input pulse seen in Fig. 4.5(a) and initial stored energy distribution in Fig. 4.5(c).

input pulse at the same location, lowering the pulse intensity there. This can enable an input spatio-temporal pulse profile with lessened sculpting requirements. To demonstrate, the inverse of the goal output pulse's spatial energy distribution, seen in Section 4.1 Fig. 4.4(b), as the remaining stored energy distribution, shown in Fig. 4.7(d). For an input pulse of 40-J and initial stored energy split evenly for the "11-7" configuration, a total

stored energy of ∼34.46-kJ is required equating to a 72.5% amplification efficiency—4.5% greater than the flat remaining stored energy case above. Increasing the remaining energy on the spatial edges of the amplifier and reducing the energy on center lowers the sculpting requirements on the pulse as seen in the input pulse spatio-temporal intensity distribution, Fig. 4.7(a), and the input pulse peak intensity spatial distribution, Fig. 4.7(e). While this arrangement has greater efficiency and reduced sculpting requirements, it does have a larger peak B-integral value of ∼5.

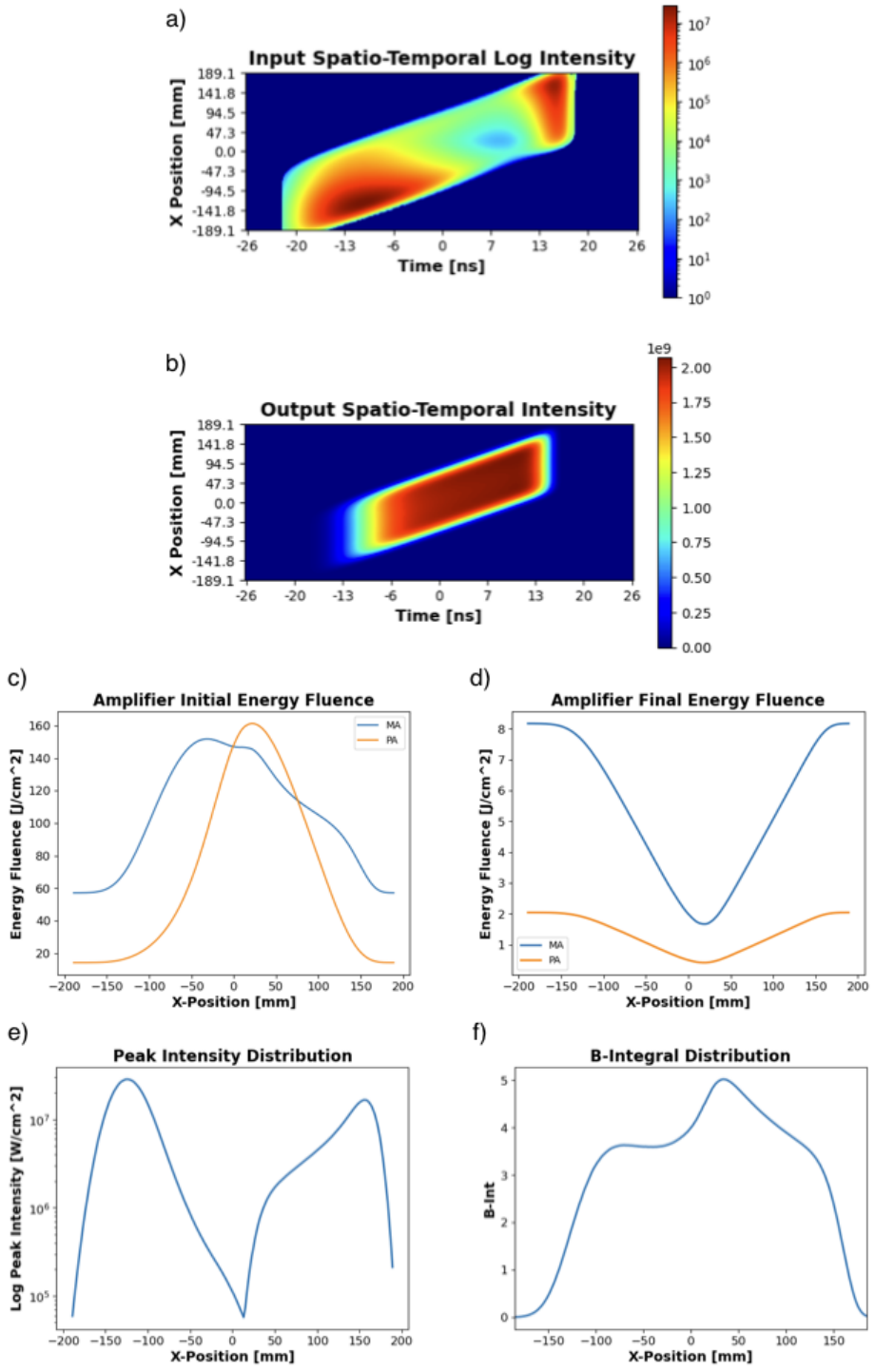

Figure 4.7: The second case of a modified profile of the remaining stored energy distribution in the MA and PA. a) Log intensity of the 40-J input pulse spatio-temporal profile that produces b) the amplified 25-kJ output pulse spatio-temporal profile. The spatial distribution of c) the initial stored energy fluence in the MA and PA, d) the final stored energy fluence in the MA and PA after amplification, e) peak intensity of the input spatio-temporal pulse, and f) total B-integral accumulated during amplification.

Chapter 5

Enabling technology for next generation ultrahigh-intensity lasers

5.1 Nexawatt system overview and technology needs

The Nexawatt (NIF Exawatt) system is based on a single-aperture of a modified NIF beamline that incorporates an OPCPA front-end and Nd:Mixed-Glass main amplifiers, similar to the Texas Petawatt and ELI-Aton lasers [24, 95]. Nd:Glass amplifiers have been traditionally considered "narrow-bandwidth" amplification mediums; however, when the amplifier is composed of mixed substrate glass it can support a much broader spectrum enabling high-energy, short-pulse amplification. In 2007, Hays et al. showed in a numerical study that an initial amplification stage of K-824 Nd:silicate glass slabs followed by a second amplifier composed of APG-1 Nd:phosphate glass slabs can have with total gain 104 while supporting an amplified bandwidth capable of producing ∼100-fs FTL pulses [52]. Using a 20-ns chirped beam-pulse to extract the full energy from a NIF-like beamline composed of Nd:Mixed-glass potentially results in, after diffraction losses, ∼20-kJ in a 100-fs FTL pulse—an 0.2-EW

peak-power laser. The general architecture of the full Nexawatt energetics chain is based off the conceptual schematic presented by Hays et al. [52].

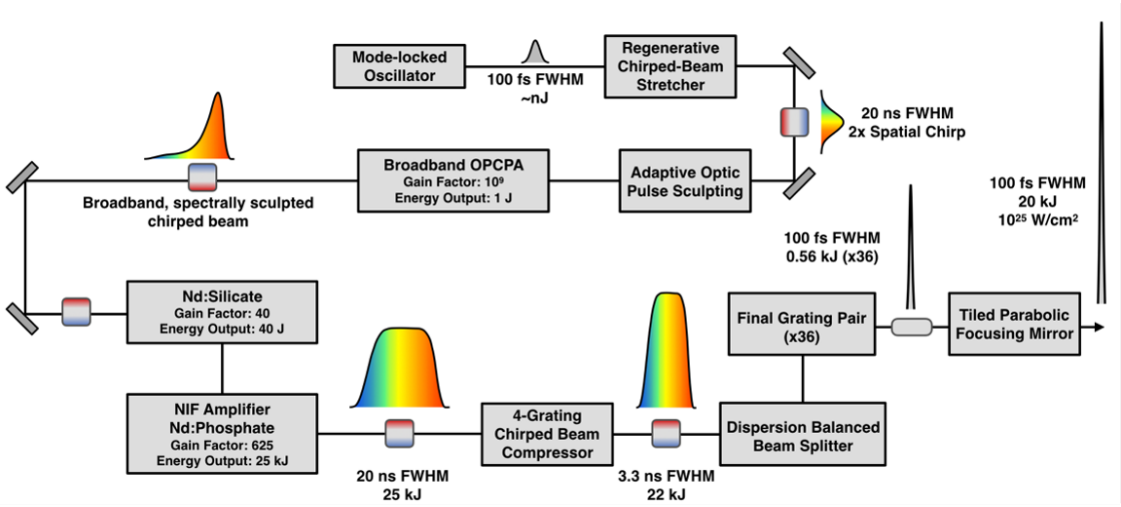

Figure 5.1: Flow chart diagram of the Nexawatt laser

The pulse originates from a Ti:Sapphire mode-locked oscillator as a ∼100-fs duration, ∼nJ pulse with a spectrum centered at 1060-nm. The pulse travels to a multi-pass regenerative stretcher where it is temporally stretched to ∼20-ns. From here, the beam is sent into a cylindrical telescope to expand the vertical dimension, creating a 2:1 aspect ratio, and then enters a single grating pair, composed of gratings identical to those in the compressor, that induces a 2x spatial chirp. The output of this is our chirped beam-pulse. Due to the unique gain effects present in CPJBA the spatio-spectral distribution of the pulse must be appropriately sculpted [91, 92]. To further deal with spatial gain effects and amplifier inhomogeneities an adaptive optic allows for a spatial mask to be applied to the beam, similar to the NIF frontend [93, 94]. A vast majority of the total system gain comes from a broadband OPCPA pre-amplifier, with a gain of 109, which also performs the bulk of the spectral sculpting on the highly stretched pulse by modulating the pump intensity in time [89, 90]. At this point the chirped beam-pulse has approximately 1-J of energy and is expanded to an aperture of 37-cm x 37-cm before entering the two separate large-aperture, NIF-like power amplifier stages—a Nd:Silicate stage followed by a Nd:Phosphate stage [52].

The now 20-ns, 25-kJ chirped beam-pulse travels through the six-grating compressor, split into 36 identical copies by a dispersion balanced beam splitter arrangement to 36 distributed final grating pairs, and emerges as 36, 18.5-cm by 37-cm aperture beamlets each with ∼556-J of energy compressed down to a 100-fs FWHM FTL pulse duration for a total power of 0.2-EW. The beamlets are phased together using a multi-mirror focusing array; both a tiled parabolic focusing mirror, similar to those used by large-aperture telescopes [59], and a dipole focusing system [57] have been discussed. The former, shown here, can focus to 10^{25} W/cm^2, while the latter has been previously simulated with an 0.2-EW laser to achieve 10^{26} W/cm^2 [57]. This is, respectively, two and three orders-of-magnitude greater than the current world record. This focused intensity would push ultrahigh-intensity lasers into the ultra-relativistic optics regime [96], and well within the QED plasma regime [97].

5.2 Multi-pass regenerative stretcher

To safely extract the full stored ∼26-kJ of energy from a single NIF power amplifier requires a stretched pulse with duration greater than 20-ns [47]. In practice, this stretch factor is difficult to achieve on few-pass stretchers as a nanosecond difference in group delay requires nanosecond size optics, which are meter-scale. Stretcher optics have stringent quality requirements, such as radius-of-curvature, surface flatness, roughness and so forth, to avoid wavefront aberrations propagating through the amplifier chain and maintain a high-level of temporal intensity contrast. These two factors combined present a large engineering and financial challenge. Instead, by inducing only a small amount of GDD per pass and performing a high number of passes until the desired GDD is acquired, one can use reasonably sized optics. However, losses from the gratings, as well as other optics, will compound on each pass. Having sub-nJ pulses after stretching places considerable burden on the downstream OPCPA amplifier. By placing the stretcher inside the cavity of a regenerative amplifier one

can create a high-pass stretcher that maintains, or amplifies, the pulse energy.

The major requirements of the regenerative stretcher for the Nexawatt system are: produce a stretched pulse of at least 20-ns, have a dispersion profile that is the conjugate of the compressor and total system material dispersion, and minimize the creation of pre- and post-pulses that can propagate through the system degrading the final temporal contrast. To date, two intracavity stretcher designs have been published. In 2017, Liebetrau et al. published an intracavity Offner-type stretcher producing a 3.9-ns, 100-μJ stretched pulse [80]. However, the line focus produced on a secondary telescope mirror of the stretcher, inherent to any Offner-type stretcher, limited the pulse energy to avoid optical damage and lead to degraded temporal intensity contrast in the ps-pedestal. At the convex mirror the beam is spatially chirped and focused to small size, which imparts a spectral phase noise on the pulse due to mirror imperfections and manifests as a ps-scale, slow rising edge on the pulse [98, 99]. In 2019, Su et al. presented an intracavity Martinez-type stretcher demonstrating 10-ns, 5-mJ stretched pulses [100]. This design utilized a simple hemispherical cavity that is susceptible to pulse overlap in the gain media. Pulse overlap creates a spectral interference leading to a modulation of the pulse phase and intensity generating a pre-pulse after compression [101, 102]. The regenerative stretcher presented here, shown below in Fig. 6.1, uses a Martinez stretcher inside an optical cavity that places the gain media in a unidirectional, single-pass ring to better isolate from pulse overlap and reduce the mode size in the crystal for more efficient pumping.

The pulse is coupled into, and out of, the regenerative stretcher by a thin-film polarizer (TFP) and Pockels cell where (PC) it then travels through a Martinez stretcher. After double passing the stretcher, the pulse polarization is rotated from p-polarization to s-polarization by a Faraday rotator (FR) and half-wave plate (HWP) to be reflected by a second TFP. Once reflected the pulse is rotated back to p-polarization by a HWP so it can pass lossless through a Brewster cut Ti:Sapphire crystal and back through the TFP. In this unidirectional, single-

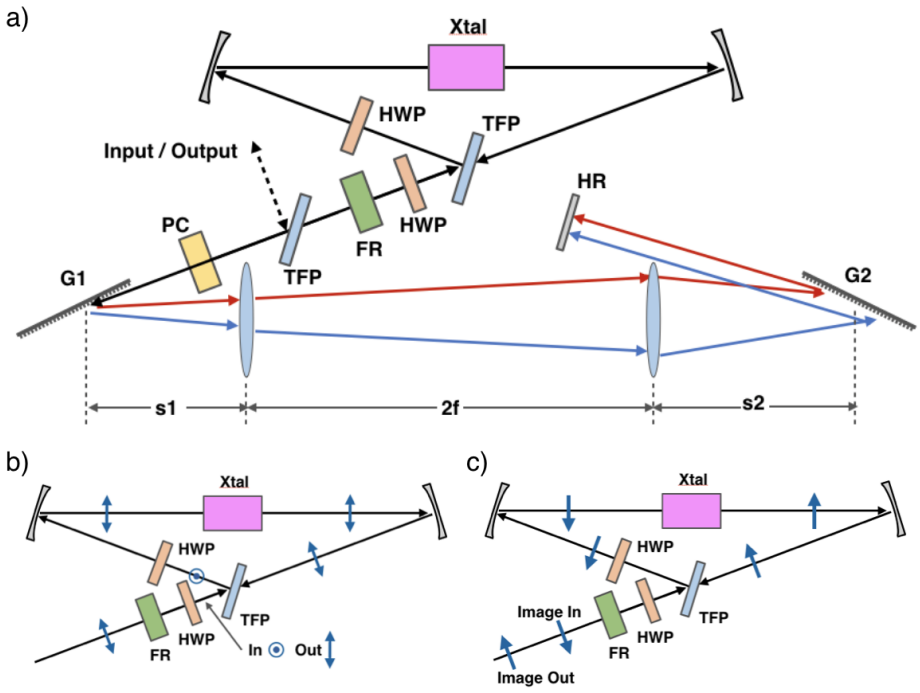

Figure 5.2: Schematic of the regenerative stretcher design

pass ring a one-to-one Keplerian telescope, formed by two 500-mm focal length concave mirrors at 4-degree AOI for astigmatism compensation in the 12-mm long Brewster cut crystal, focuses the pulse for amplification. The Martinez stretcher must have a length greater than 3 meters, for a double-pass length of 6 meters, to fully contain the 20-ns stretched pulse on one side of the Pockels cell. In this manuscript we have used 500-mm achromat lenses as the focusing elements in the Martinez stretcher for simplicity of the cavity design and dispersion analysis; however, in practice the stretcher should be built with concave, circular mirrors to avoid the aberrations that come with the use of lenses [70]. Starting from the flat HR mirror in the spectrally dispersed arm of the stretcher, a full round trip in the cavity, shown below in Fig. 6.2, will double-pass the stretcher while passing through the gain element only once.

This cavity is essentially a four-mirror z-fold or x-fold oscillator cavity where the two arms have been combined into one and only a single-pass of the gain medium is made per round-trip. The total round-trip ABCD ray transfer matrix of the regenerative stretcher determines

the stability limits of the cavity. Since matrix multiplication is associative, subsections of the total ABCD matrix can be grouped together. Define the distance from the end mirror (HR) to the second grating (G2) as d_1, the distance from the first grating (G1) to either curved mirror (CM1/2) as d_2, and the length of the Martinez stretcher, $2f - s_1 - s_2$, as L_{str}. Starting at the flat end mirror the total round-trip ABCD matrix is,

$$\mathbf{M}_{Total} = \mathbf{M}_{arm}\mathbf{M}_{xtal}\mathbf{M}_{arm} \tag{5.1}$$

$$\mathbf{M}_{arm} = \begin{bmatrix} -1 & L_{str} - d_1 - d_2 \\ 0 & -1 \end{bmatrix} \tag{5.2}$$

$$\mathbf{M}_{xtal} = \begin{bmatrix} 1 - \frac{\Lambda}{\eta} & \Lambda \\ \frac{\Lambda}{\eta^2} - \frac{2}{\eta} & 1 - \frac{\Lambda}{\eta} \end{bmatrix} \tag{5.3}$$

Here, both Λ and η have a different form in the tangential and sagittal plane. Namely,

$$\Lambda_{s,t} = 2d_3 + \frac{l_{xtal}}{n_{xtal}},\ 2d_3 + \frac{l_{xtal}}{n_{xtal}^3} \tag{5.4}$$

$$\eta_{s,t} = \frac{R}{2\cos\theta},\ \frac{R\cos\theta}{2} \tag{5.5}$$

where l_{xtal} is the length of the crystal, n_{xtal} is the crystal index of refraction, d_3 is the distance from the curved mirror to the crystal face, R is the curved mirror's radius of curvature, and θ is the AOI on the curved mirror. Like the four-mirror oscillator, stability of the cavity and collimation of the cavity mode in the stretcher arm can be obtained by tuning the separation of the two curved mirrors. Defining $\Lambda = 2\eta + \delta$ and using the cavity stability equation (2.29), the cavity stability can be defined in terms of a detuning parameter, δ, from a perfect telescope,

$$0 \leq \delta\left[\frac{1}{\eta} - \frac{L_{str} - d_1 - d_2}{\eta^2}\right] \leq 2 \tag{5.6}$$

Clearly, the cavity is stable when the detuning parameter is zero and for many small values

of δ as long as $(L_{str} - d_1 - d_2)/\eta \leq 1$. This is better viewed by recasting the cavity stability in terms of distances d_1 and d_2 allowed for some given detuning parameter and stretcher length,

$$L_{str} - \eta \leq d_1 + d_2 \leq (L_{str} - \eta) + \frac{2\eta^2}{\delta} \tag{5.7}$$

When δ is small, this cavity design supports a wide range of mirror spacings d_1 and d_2 making it relatively insensitive to changes in these mirror spacings. In the design presented here, d_1 is 764.5-mm, s_1 and s_2 equal 435.5-mm, d_2 is 1064.5-mm, and the detuning parameter δ is $\sim$14.4 in the sagittal plane and $\sim$14.7 in the tangential plane.

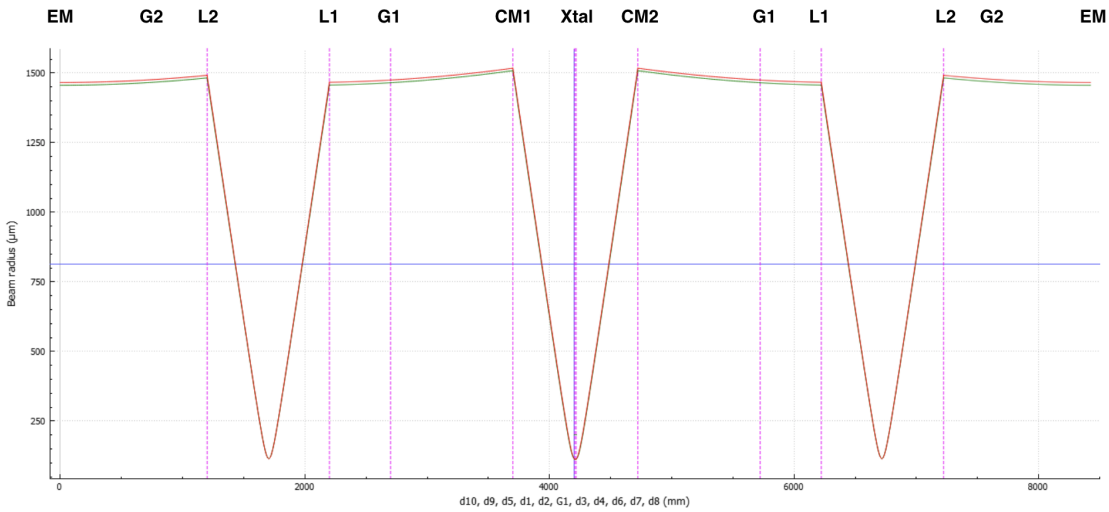

Figure 5.3: Cavity caustic of the regenerative stretcher design

The stretcher presented here is designed to generate approximately 1-ns of delay per round trip pass. The transmissive optics in a NIF-like beamline, along with the intracavity optical elements of the regenerative stretcher, impart additional material dispersion that cannot be compensated by an identical stretcher-compressor pair. This can largely be accounted for by modifying the groove density and AOI of the stretcher gratings [70, 103]. Table 5.1, below, lists the GDD and TOD contributions of each element in the regenerative stretcher, the six grating CPJBA compressor, and the reported material dispersion of a NIF beamline [104].

Furthermore, the 2x spatial chirp required for CPJBA is created by a parallel grating pair with the same design as the final compressor gratings, 1780-ln/mm groove density and 76.5-degree AOI, after the regenerative stretcher. The additional negative dispersion created by the grating pair can be compensated by over stretching the pulse. A parameter scan was performed on the regenerative stretcher grating groove density and AOI to determine the optimal configuration that balances all GDD in the system while minimizing the TOD contribution. This first-pass optimization suggests the use of 1760-ln/mm groove density gratings at a 71.85-degree AOI, which allows for full GDD compensation of the system with a residual TOD of -4.94E05-fs^3. This residual TOD would broaden the final 100-fs TFL output pulse to 102.6-fs. Through further optimization of the regenerative stretcher, such as modifications to the spherical mirrors in the stretcher [70], one can fully compensate the residual TOD; however, that analysis is beyond the scope of the paper as it requires accurate knowledge of the full system design. Using 500-mm focal length achromat lenses the 2f-2s length in the stretcher is 129.8-mm, which will stretch the pulse to 20-ns after 20 round-trip passes.

Item	Material	Length [mm]	GDD [fs^2]	TOD [fs^3]
PC	DKDP	16	4.6E+03	4.33E+04
FR	TGG	16	8.57E+04	5.26E+04
Lens	N-BAK4	9	2.45E+04	3.57E+04
-	N-SF10	4	3.17E+04	3.27E+04
Xtal	Al2O3	12	3.48E+03	7.72E+03
Compressor	-	-	-5.19E+08	1.01E+10
Grating Pair	-	-	-7.05E+05	1.37E+07
NIF Material	-	-	2.34E+05	1.20E+06
Stretcher	-	-	5.20E+08	-1.01E+10
Total	-	-	3.90E+01	-4.94E+05

Table 5.1: Tabulation of the GDD and TOD contribution of the regenerative stretcher intracavity components and rest of the Nexawatt laser chain for the full system dispersion.

5.3 Multi-beam focusing system

Prior to the final compressor grating pair the pulse must be split into multiple identical copies to lower the fluence of each beamlet below the damage threshold of the gratings. This can be accomplished with a cascading beam splitter arrangement, shown in Section 3.2 in Fig. 3.5, where each beamlet is transmitted through a beam splitter only once to ensure all copies experience same dispersion response. The ARC grating design has undergone extensive damage testing [55, 56]. For longevity of the grating, actual operational fluence should not occur at the damage threshold limit (DTL) but at a much lower fluence where damage is statistically unlikely. On ARC the operational fluence was set at the point where 10^{-4} fraction of the beam causes damage. Extrapolating the grating damage threshold trend shown in Fig. 10, we estimate that the multi-layer dielectric gratings can handle approximately 1-J/cm2 at 100-fs. With a final beamlet size of 18.5-cm x 37-cm each can have a maximum energy of ∼685-J to stay below the grating damage threshold. With an estimated grating efficiency of ∼97.5% the extracted ∼25.1-kJ will be reduced to ∼21.6-kJ after the sixth grating. Splitting the pulse into 36 beamlets the fluence on the final grating G6 will be ∼600-J and below the operational fluence limit.

Phasing the 36 identical beamlets together is carried out by an appropriate focusing arrangement. In 2014, Gonoskov et al. presented a technique called anomalous radiative trapping (ART) where multiple ultrahigh-intensity beams are focused together to approximate an electric dipole [57]. In this simulation they showed that a 200-PW laser split into multiple channels can reach a focused intensity greater than 10^{26} W/cm^2. While this setup would provide the theoretical maximum focused field intensity, it has yet to be experimentally demonstrated. Here we examine a more traditional focusing arrangement, shown below in Fig. 5.4, where a large-aperture parabolic mirror is created by tiling together multiple, smaller individual mirror segments. This technique has already been put into practice by the large-aperture telescope community [59]. The telescope tiled mirror segments have been

produced at meter-scale with clear apertures of ∼98% [105]. Each beamlet is focused by an individual mirror segment of modest f-number, that when tiled together produces a low f-number parabolic mirror. Phasing now becomes a three degree-of-freedom issue needing, in principle, ∼100-nm of accuracy for alignment instead of the five degree-of-freedom problem with 10-nm of accuracy needed for tiling multiple gratings together [37, 38, 39].

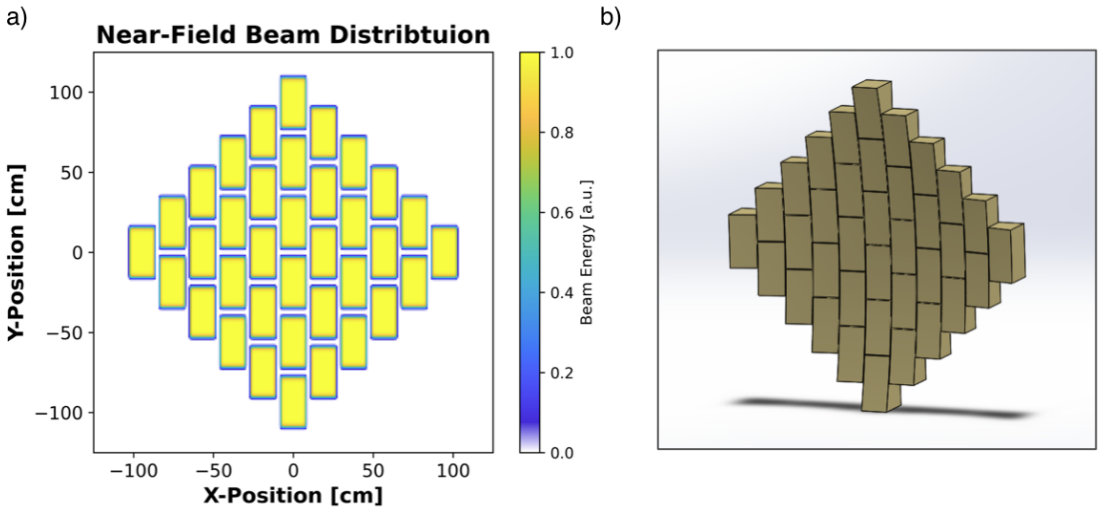

Figure 5.4: (a) Near field distribution of the 36 beamlets prior to focusing (b) Rendering of the tiled parabolic focusing mirror for Nexawatt.

A custom Python [80] script was written to evaluate the tiled parabolic mirror as a focusing system for the Nexawatt laser. The fields are defined before the focusing optic and propagated to the focus using Rayeligh-Sommerfeld propagation [106]. The Bluestein method [107] is used for calculating the numerical Fourier transforms which allows for arbitrarily sampled input and focal plane, relaxing the computational requirements for simulating very low f-number focusing systems. In this model the 36 mirror segments are spaced 5-mm apart, each with an aperture of 19-cm x 38.5-cm. The tiled parabolic mirror assembly is set to a focal length of 198.5-cm, giving an effective f-number of 0.95 in the horizontal dimension and 0.89 in the vertical dimension. The f-number of the individual segments are much more modest, with 10.6 in the horizontal dimension and 5.6 in the vertical dimension. This focusing system, with the input beam spatial profile shown in Fig. 5.4, produces the far-field distribution shown below in Fig. 5.5. The focal spot has a $1/e^2$ width of 3.41 um in both the

x-axis and y-axis, and a peak intensity exceeding 1x10^{25} W/cm^2—two orders of magnitude beyond the current record.

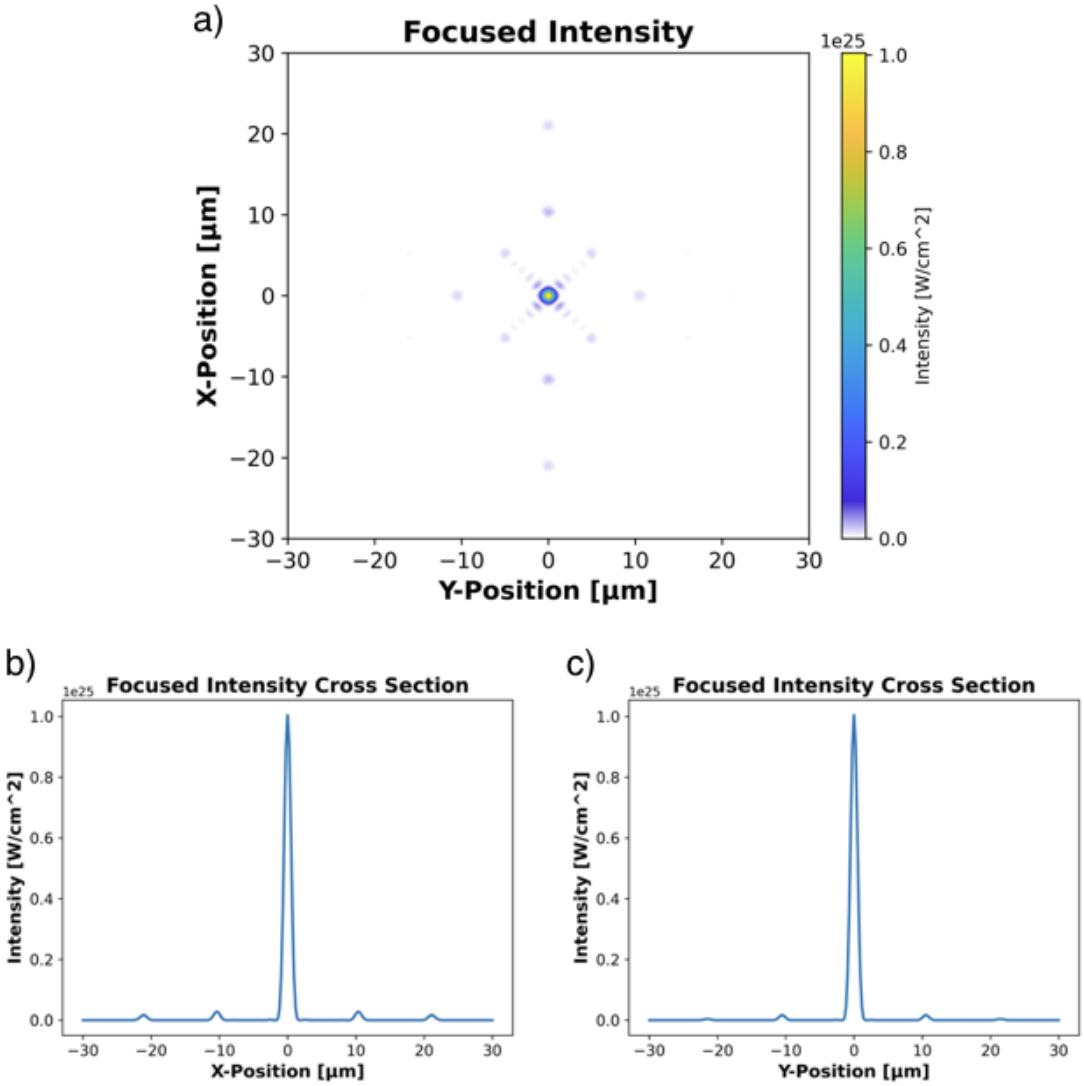

Figure 5.5: Beam intensity at the focus of the tiled on-axis parabolic mirror showing (a) far-field intensity distribution (b) cross-section at center in the X-direction (c) cross-section at center in the Y-direction.

5.3.1 Beam cophasing and sensitivity

In the tiled parabolic mirror array, each mirror segment will be positioned using three piezoelectric actuators on the rear allowing for adjustments to the tip, tilt, and piston. The

challenge of cophasing the individual segments together to create the desired, ideal mirror shape is identical to that for large-aperture telescopes. To address this issue multiple cophasing techniques have been developed and employed [108, 109, 110]. In particular, a technique called Fizeau Interferometric Cophasing of Segmented Mirrors (FICSM) has numerically shown the potential to cophase mirror segments with initial piston errors of 300 μm and tip-tilt error of 0.5 arcseconds to final state with a RMS wavefront error of 3.65 nm and a 0.99997 Strehl ratio for 4 μm light [110]. In an experimental demonstration, Cheetham et al. cophased 18 mirror segments to an RMS wavefront error of 25 nm and a Strehl ratio of 94% [111]. These cophasing procedures are considered in the active optics class and not the adaptive optics class, meaning they cannot quickly respond to misalignments. An error analysis on the tip, tilt, and piston of the tiled parabolic mirror arrangement has been performed to better understand the sensitivity for ultrahigh-intensity focusing.

Any random source of error will have a normal distribution. To simulate this, we generate a list of 36 different alignment errors from a Gaussian distribution, centered at zero, with a set error standard deviation. For the piston error this was done using a mirror displacement value, while for tip and tilt an angular error was used. Each of the 36 mirror segments is assigned a value from the error distribution in the ray trace model and the focused intensity is calculated. An example of an error distribution for a piston error with a standard deviation of 40-nm is shown below in Fig. 5.6(b). Each standard deviation value is repeated ten times (i.e. ten different actuator error lists per standard deviation) in the ray trace code, recording the peak focused intensity each time, to account for the statistical nature of the error. Below, Fig. 5.6(a) shows the reduction in focused intensity with increasing piston error distribution standard deviation. A standard deviation of 40-nm, with an average RMS error of 38.1-nm, resulted in an average focused intensity error of 5%.

The tip-tilt error was analyzed in a similar method, except an angular error on the order of μRad was used. Here, the tip corresponds to rotation about the x-axis of the mirror (i.e. the

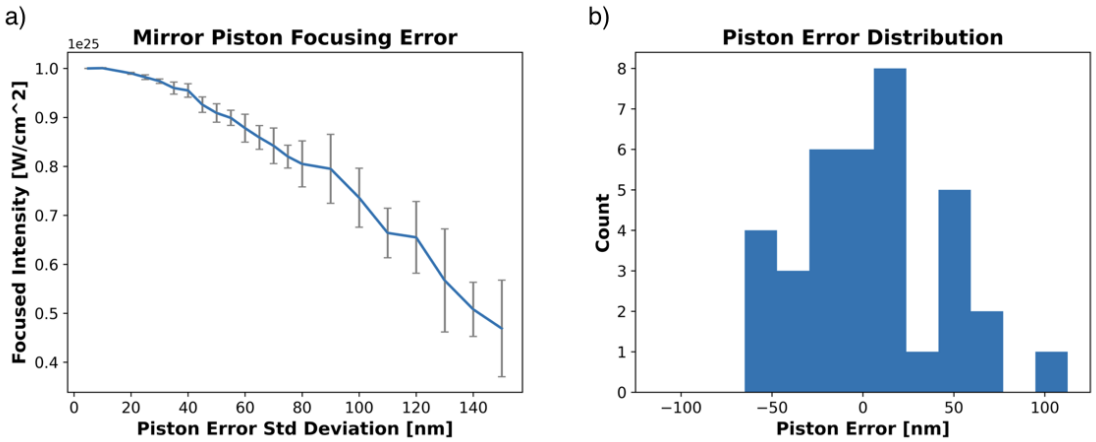

Figure 5.6: (a) Piston error affect on focused intensity. Error bars represent the standard deviation of the focused intensity for the 10 runs at a particular piston error standard deviation distribution. (b) Example of a randomly distributed piston actuator error for the 36 mirror segments with a 40-nm standard deviation.

longer dimension of the mirror is rotated) while tilt corresponds to rotation about the y-axis of the mirror (i.e. the shorter dimension of the mirror was rotated). For the tip error, an error standard deviation distribution of 0.4 μRad resulted in a 5% decrease in peak focused intensity, while for the tilt error this was 0.9 μRad. The difference between the two is due to the f-number difference for the different mirror axes. However, if the pointing error is caused by actuator displacements this result should be the same for the two axes since the actuator displacement for the horizontal tilt will produce twice the angular deviation of the tip due to the length difference to the pivot point.

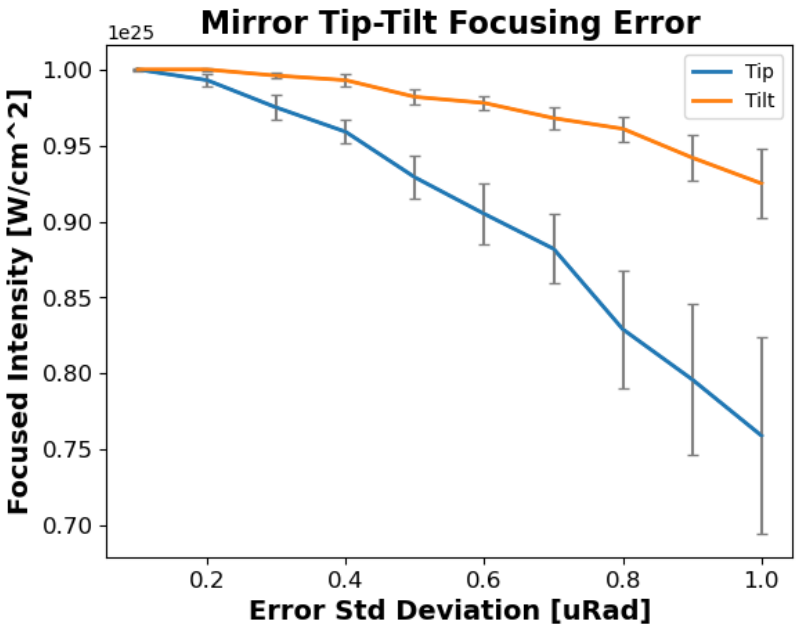

Figure 5.7: Tip-Tilt error affect on the focused intensity. Error bars represent the standard deviation of the focused intensity for the 10 runs at a particular tip or tilt error standard deviation distribution.

5.4 Ultra-broadband, amplitude neutral beam splitter

This section has been adapted from a version of record manuscript published in Optics Express with permission under Optica Publishing Group's Open Access Publishing Agreement.

K. D. Chesnut and C. P. J. Barty, "Method for producing identical spectral copies of ultra-broadband arbitrary light fields," Optics Express **32**(6), 9790-9799 (2024). https://doi.org/10.1364/OE.516966

5.4.1 Introduction

CPJBA applied to a NIF-like amplifier beamline requires precise sculpting of the spatio-spectral input pulse to the amplifier to obtain the desired amplified pulse distribution that can be compressed down to its 100-fs TFL limit without spatio-temporal couplings. Critical

to this is accurate measurement of the sculpted spatio-spectral pulse prior to amplification. The ability to create identical copies of a broadband optical source, whether coherent or low-coherence light, with a beam splitter is critical to many optical measurement applications such as Fourier transform spectroscopy [112] or any of the myriad of ultrafast pulse measurement techniques [113]. At large spectral widths, however, conventional metallic and multi-layer dielectric beam splitters exhibit high loss and/or large wavelength-dependent reflection and transmission. Currently, efficient ultra-broadband beam splitters are created using chirped multi-layer dielectric (MLD) coatings that also induce a phase response on the reflected pulse that is approximately equal to the phase response on the transmitted pulse due to material group delay dispersion (GDD) [114]. However, while the reflected and transmitted pulses are approximately similar, they are not identical. One method to ensure identical pulses is to have two MLD beam splitters and force each pulse copy to undergo one transmission and one reflection event [115]. While the two pulse copies produced in this way are identical, they are not exact replicas of the original input pulse unless the reflectivity or transmission does not vary as a function of frequency. Due to their discrete nature, MLD coatings also have a varying amplitude and dispersion response that is not easily described analytically. These variations, which are difficult to accurately quantify and compensate, are imparted onto the pulse copies distorting them from the original input pulse [116, 117, 118]. In this manuscript, we show that instead of using MLD coatings one can create an ultra-broadband beam splitter arrangement—with an exceptionally flat amplitude response within a Michelson interferometer setup—by orienting an uncoated optical flat at a precise angle-of-incidence (AOI), which we will call the Chesnut-Barty (CB) angle. At this angle, one can produce three, spectral copies of the original, two of which have identical spectral phase. In the following sections, the precise angle at which this maximally flat spectral amplitude response occurs for any material will be derived and the angle's material and polarization dependence will be presented.

5.4.2 Ultra-broadband Fresnel beam splitter arrangement

Configuration for minimal spectral amplitude distortion

When a light wave encounters the interface of two different dielectric media it is both reflected and refracted. For lossless media, the ratio at which the light wave's electric field is split into a reflected and transmitted portion is described by the Fresnel equations [119],

$$R_s(\theta,\lambda) = \left\{ \frac{n_1(\lambda)\cos(\theta) - n_2(\lambda)\sqrt{1-[\frac{n_1(\lambda}{n_2(\lambda)}\sin(\theta)^2]}}{n_1(\lambda)\cos(\theta) + n_2(\lambda)\sqrt{1-[\frac{n_1(\lambda)}{n_2(\lambda)}\sin(\theta)]^2}} \right\}^2 \tag{5.8}$$

$$T_s(\theta,\lambda) = 1 - R_s(\theta,\lambda) \tag{5.9}$$

$$R_p(\theta,\lambda) = \left\{ \frac{n_1(\lambda)\sqrt{1-[\frac{n_1(\lambda)}{n_2(\lambda)}\sin\theta]^2} - n_2(\lambda)\cos(\theta)}{n_1(\lambda)\sqrt{1-[\frac{n_1(\lambda)}{n_2(\lambda)}\sin\theta]^2} + n_2(\lambda)\cos(\theta)} \right\}^2 \tag{5.10}$$

$$T_p(\theta,\lambda) = 1 - R_p(\theta,\lambda) \tag{5.11}$$

Here, n_1 and n_2 are the index of refraction of air and the substrate respectively, θ is the AOI, λ is the wavelength, and R and T are the reflection and transmission intensity response, respectively, with subscript denoting the polarization. For simplicity, the polarization subscript will be omitted in the rest of the manuscript with the assumption that any process is purely in one linear polarization state. Fig. 5.8(a), below, shows how a single input beam undergoes a Fresnel event each time it encounters the material interface, eventually splitting into multiple output beams.

In the simplest spectrally uniform beam splitter arrangement, the full beam is incident on an optical flat at some AOI where a portion of the beam is reflected, beam A in Fig. 5.8(a), and the remainder is transmitted into the optic. The transmitted portion of the beam transits the optical flat where it then undergoes a second transmission event at the back interface of the optic, beam B in Fig. 5.8(a). For the two beams to be identical they must have the exact

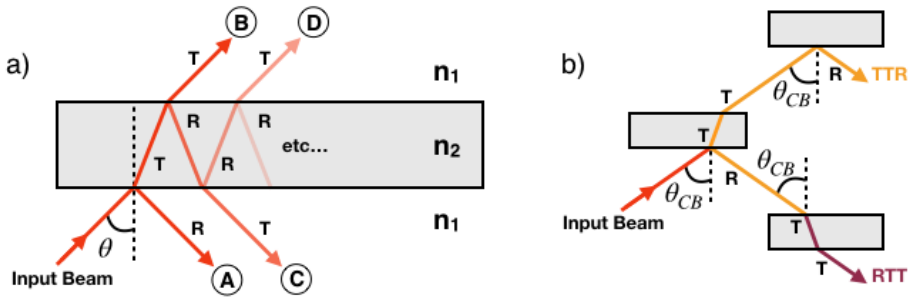

Figure 5.8: A) Diagram of successive Fresnel transmission (T) and reflection (R) events on an uncoated optical flat from a single input beam. b) Schematic of an ultra-broadband, spectrally flat beam splitter arrangement composed of three identical uncoated optical flats.

same number of transmission and reflection events. Thus, as shown above in Fig. 5.8(b), the full Fresnel beam splitter arrangement consists of three identical uncoated optical flats. This allows the portion that was reflected off the first optical flat, beam A in Fig. 5.8(a), to be transmitted through an identical optical flat, while the portion that was first transmitted, beam B in Fig. 5.8(a), is then made to reflect off a third optical flat—both secondary events occur at the exact same AOI as the first. Now, each separate portion has undergone one Fresnel reflection (R) and two Fresnel transmissions (T) through the optical flat and experiences the same total amplitude response albeit in different orders—RTT and TTR. There is a third beam, beam C in Fig. 5.8(a), that naturally undergoes two transmissions and one reflection, in a TRT order, but has twice the material dispersion from transiting the optical flat twice. Using Eq. (5.2) or Eq. (5.4) above, the wavelength and angle dependence of the product of one Fresnel reflection and two Fresnel transmissions can be rewritten as R(1-R)(1-R) or,

$$A(\theta, \lambda) = R(\theta, \lambda)^3 - 2R(\theta, \lambda)^2 + R(\theta, \lambda) \tag{5.12}$$

To find the optimal reflection and transmission ratio that minimizes this function about a particular central wavelength, we take the derivative of Eq. (5.12) with respect to wavelength and set it equal to zero. The result is a simple quadratic relation, Eq. (5.14), with two roots,

Eq. (5.15).

$$\frac{\partial A}{\partial \lambda} = \frac{\partial A}{\partial R}\frac{\partial R}{\partial n}\frac{dn}{d\lambda} \tag{5.13}$$

$$\frac{\partial A}{\partial \lambda} = 3R^2 - 4R + 1 = 0 \tag{5.14}$$

$$R = \frac{1}{3}, 1 \tag{5.15}$$

The first root suggests that a maximally flat local spectral response occurs when the reflectivity is one-third and transmission is two-thirds, equating to 14.8% of the original pulse energy in each spectral copy, while the second root implies zero transmission and is thus of no practical interest. The reflectivity amplitude can be determined from either Eq. (5.1) or Eq. (5.3), depending on the polarization, which are only functions of the index of refraction, described by the Sellmeier equation, and the incident angle. Thus, the task for any specific center wavelength and material is to find the angle at which R, in Eq. (5.1) or Eq. (5.3), equals one-third.

The variation of spectral amplitude response as a function of angle is illustrated in Fig. 5.9 below, which shows the RTT amplitude response of an S-polarized pulse (a) and P-polarized pulse (b) centered at 800-nm incident on an optical flat of fused silica at various AOIs. The CB angle occurs at 72.95 degrees for S-polarized light and 82.25 degrees for P-polarized light.

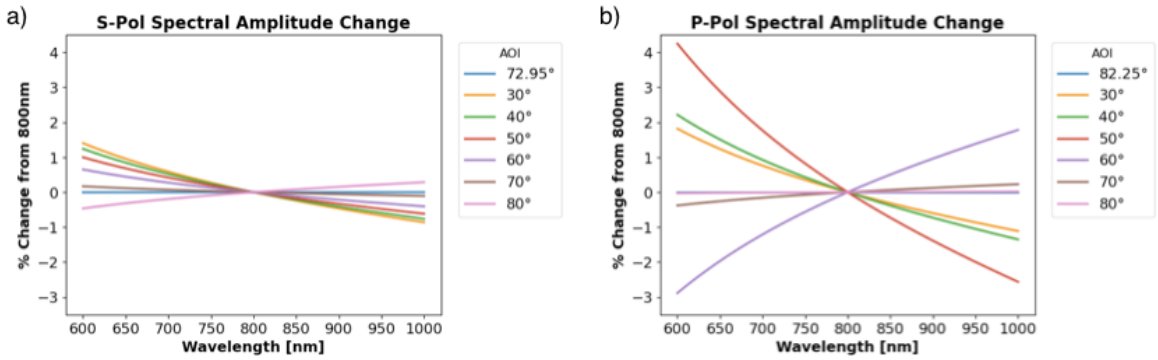

Figure 5.9: Spectral amplitude variation centered at 800 nm, for the RTT response of a) S-polarized and b) P-polarized light incident on an optical flat, composed of fused silica, for various AOIs.

The spectral flatness of the RTT amplitude response of the fused silica optical flat with P-polarized light at the CB angle is significantly more uniform than a commercial MLD beam splitter, undergoing a RT response for a balanced interferometer [115], seen below in Fig. 5.10. Here, we quantify spectral amplitude flatness as the standard deviation of the relative difference of the spectral amplitude response from the center wavelength,

$$\sigma = \sqrt{\frac{\sum_{i=1}^{N} [\frac{A(\lambda_i) - A(\lambda_i)}{A(\lambda_0)}]^2}{N-1}} \tag{5.16}$$

The spectral flatness standard deviations of the optical flat and the MLD beam splitter are 5.84E-8 and 1.60E-1 respectively, equating to over seven orders-of-magnitude increased flatness for the Fresnel beam splitter. Additionally, while each of the identical beam copies does experience material dispersion from the optical flat, the phase response is a smooth, quantifiable function that can be appropriately described by an analytical equation. In practice, one can compensate for the bulk of induced dispersion with an appropriate combination of prisms and/or gratings with the primary requirement of precise knowledge of residual dispersion terms—this is further expanded in a later section. In contrast, the dispersion ripples induced by an MLD coating cannot be fully compensated for [116, 117, 118].

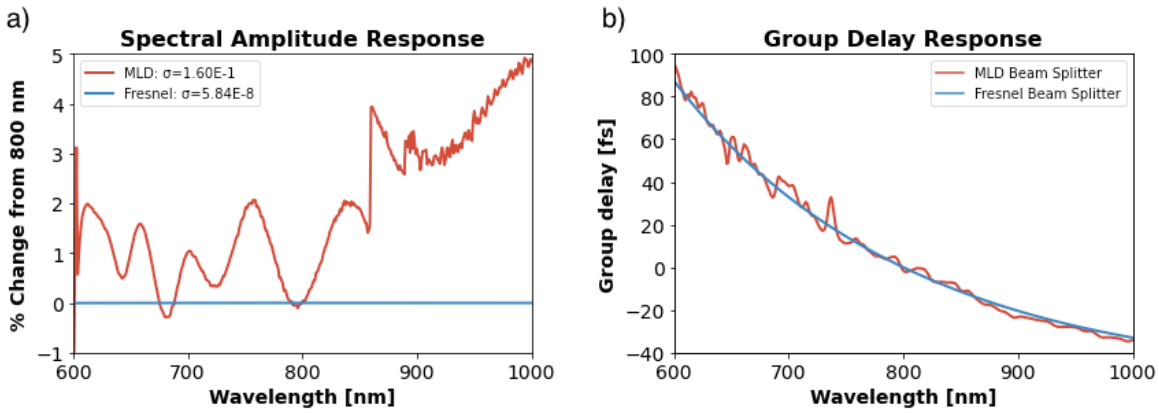

Figure 5.10: a) Amplitude and b) group delay from the RTT response of a 6 mm thick fused silica, Fresnel beam splitter with P-polarized light at the CB angle versus the RT response of a commercial 50:50 MLD beam splitter (ThorLabs p/n UFBS5050) [120].

Material and polarization dependencies

While the first derivative of the total amplitude response as a function of wavelength at the CB angle, θ_{CB}, is zero, and thus the variation of the local spectral amplitude response is minimized, there is still some residual variation of the spectral amplitude response that is material and polarization dependent. The material- and polarization-dependent curvature can be quantified by examining the second derivative of the total amplitude response with respect to wavelength at the CB angle.

$$\left(\frac{\partial^2 A}{\partial \lambda^2}\right) = \frac{\partial^2 A}{\partial \lambda \partial R}\frac{\partial R}{\partial n}\frac{dn}{d\lambda} + \frac{\partial A}{\partial R}\frac{\partial^2 R}{\partial \lambda \partial n}\frac{dn}{d\lambda} + \frac{\partial A}{\partial R}\frac{\partial R}{\partial n}\frac{d^2 n}{d\lambda^2} \tag{5.17}$$

At the CB angle the partial derivative of the amplitude with respect to Fresnel reflection is zero, as shown in Eq. (5.6) and Eq. (5.7), canceling the last two terms in Eq. (5.10). From Eq. (5.7) we find,

$$\frac{\partial^2 A}{\partial \lambda \partial R} = (6R - 4)\frac{\partial R}{\partial n}\frac{dn}{d\lambda} \tag{5.18}$$

Substituting Eq. (5.11) into Eq. (5.10) and noting that at the CB angle the Fresnel reflection amplitude, R, is one-third we find,

$$\left(\frac{\partial^2 A}{\partial \lambda^2}\right)_{\theta_{CB}} = \frac{\partial^2 A}{\partial \lambda \partial R}\frac{\partial R}{\partial n}\frac{dn}{d\lambda} = -2\left(\frac{\partial R}{\partial n}\right)^2\left(\frac{dn}{d\lambda}\right)^2 \tag{5.19}$$

Thus, we see that the curvature is a result of the change in Fresnel reflection amplitude due to a change of index of refraction and the change in index of refraction due to a change of wavelength.

Focusing first on the derivative of the index of refraction with respect to wavelength, also called the chromatic dispersion, less dispersive materials (i.e., materials with at flatter index of refraction curve) will produce less amplitude variation across the spectrum of interest.

Most optical materials have an absorption peak in the UV range, and as the spectrum approaches this peak the slope of the index of refraction curve increases. Thus, optical materials with absorption peaks further from the spectral range of interest will produce a flatter total amplitude response. Additionally, increasing the index of refraction reduces the CB angle; this effect is much more prominent for S-polarized light. At 800-nm, lithium fluoride has an index of refraction of 1.3890, fused silica of 1.4533, and SF11 of 1.7648, giving balanced amplitude angles of 74.46 degrees, 72.95 degrees, and 66.16 degrees respectively for S-polarized light [121]. Comparing these three different materials, below in Fig. 5.11, shows the significant difference in total amplitude response across 600-nm to 1000-nm. In the S-polarized case, LiF has a spectral amplitude standard deviation of 5.14E-6, fused silica of 1.01E-5, and SF11 of 5.59E-5. For P-polarization, the CB angles are 82.23 degrees, 82.25 degrees, and 82.78 degrees for LiF, fused silica, and SF11 respectively. Here, LiF has a spectral amplitude standard deviation of 1.69E-9, fused silica of 5.84E-8, and SF11 of 8.90E-6. The increased amplitude variance corresponds to the increased chromatic dispersion at 800-nm, with a chromatic dispersion of 1.09E-2 um-1 for LiF, -1.73E-2 um-1 for fused silica, and -5.77E-2 um-1 for SF11 [121].

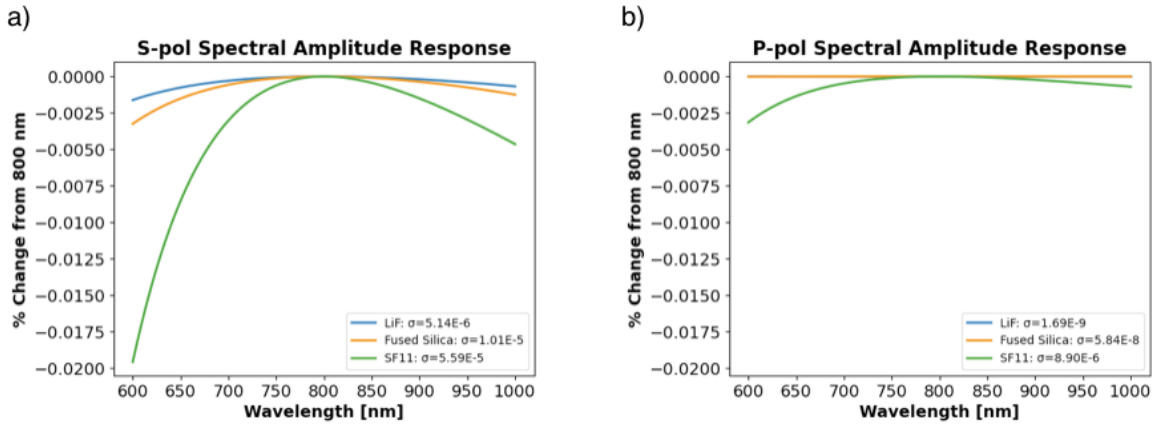

Figure 5.11: Spectral amplitude variation, centered at 800 nm, for three different materials each at their CB angle-of-incidence for a) S-polarized light and b) P-polarized light.

As stated above, the spectral amplitude response also depends on the polarization of the incident light due to the difference in the Fresnel reflection equations for S and P-polarized

light. The CB angle of S-polarized light has a much greater sensitivity to the material index of refraction than P-polarized light, allowing one to effectively tune the CB AOI by selecting a different optical material. However, S-polarized light has an increased spectral amplitude variation compared to P-polarized light, shown below in Fig. 5, with all else equal. This can be understood by examining the derivative of the Fresnel reflection responses, Eq. 1 and Eq. 3, with respect to the index of refraction. The functional form is complicated and not elucidating; however, evaluating the derivative at the index of refraction value for 800-nm light, and at the CB angle, in fused silica results in a value of -0.0348 for P-polarized light and 0.4669 for S-polarized light. The lower magnitude value for P-polarized light explains the lower spectral amplitude variation, compared to S-polarized light.

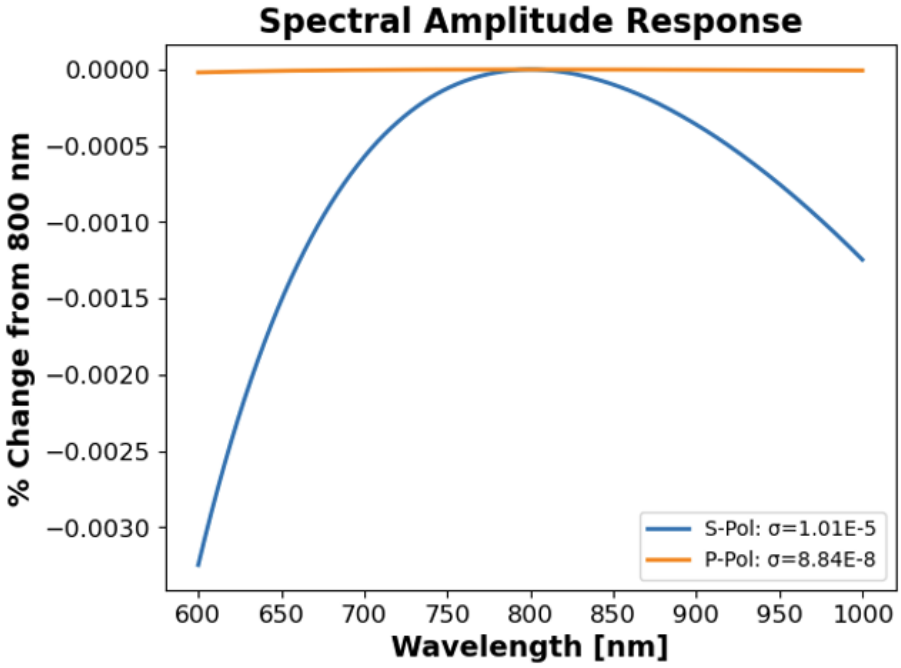

Figure 5.12: Spectral amplitude response of S-polarized and P-polarized light, centered at 800 nm, for fused silica Fresnel beam splitter set at their respective CB angles of 72.95 degrees and 82.25 degrees.

5.4.3 Interferometer with near uniform spectral response

Michelson interferometer design

The Fresnel beam splitter arrangement, shown above in Fig. 5.8(b), can be simplified to a single optical flat by incorporating retroreflectors in each of the two beam paths as seen below in Fig. 5.13. In doing so, one eliminates the primary error sources of optical flat thickness mismatch and AOI discrepancy between the primary and secondary Fresnel events. Furthermore, by varying the offset of the two paths one can configure the setup to act as either a beam splitter or Michelson interferometer.

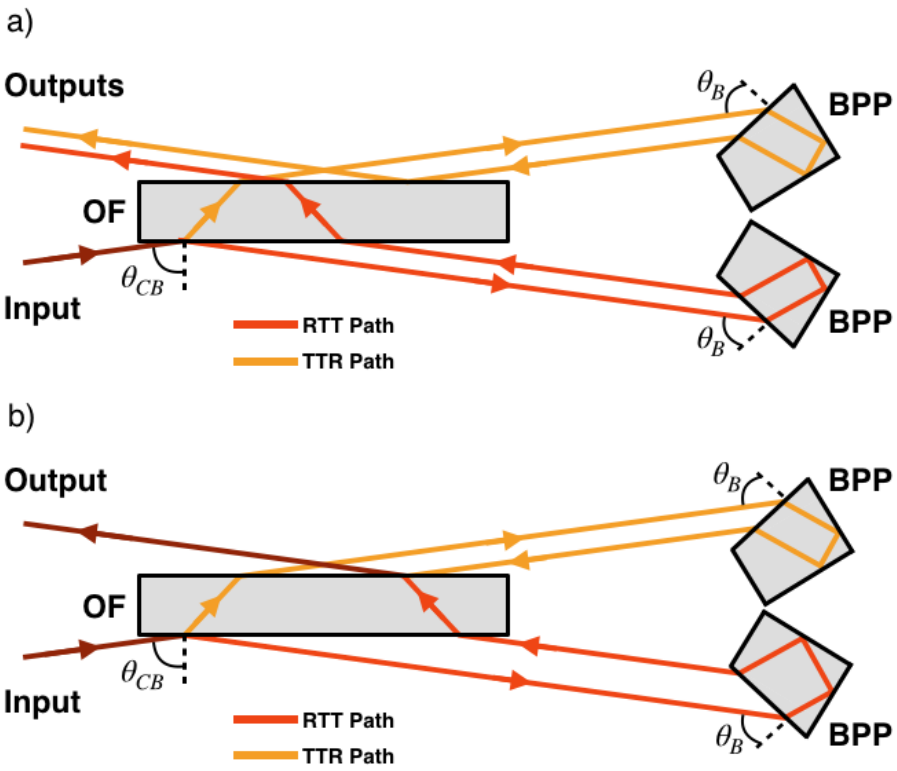

Figure 5.13: Fresnel beam splitter arrangement using a single optical flat (OF) and two Brewster's angle Porro prisms (BPP) operating in a) beam splitter and b) Michelson interferometer configurations.

To maintain the overall system spectral amplitude flatness, the retroreflectors should be total internal reflection (TIR) prisms as opposed to mirrors. TIR retroreflectors maintain

the same material path length while varying the return beam offset allowing the two beam paths to preserve equal dispersion, insofar as the two TIR retroreflectors are identical. In the p-polarization case, this can be accomplished using a Brewster's angle Porro prism (BPP)—a Pellin-Broca prism operated as a retroreflector with the incident light at Brewster's angle [122]. Here, the TIR retroreflectors induce only a Fresnel transmission response at Brewster's angle on each beam's spectral amplitude distribution as shown below in Fig. 5.14. The spectral flatness standard deviation of the Brewster's angle transmission is 2.27E-7, over a spectral range of 600-1000 nm, compared to the Fresnel beam splitter's of 5.84E-8 over the same spectral region. While this decreases the spectral amplitude flatness it is still over six orders of magnitude better than the commercial MLD beam splitter.

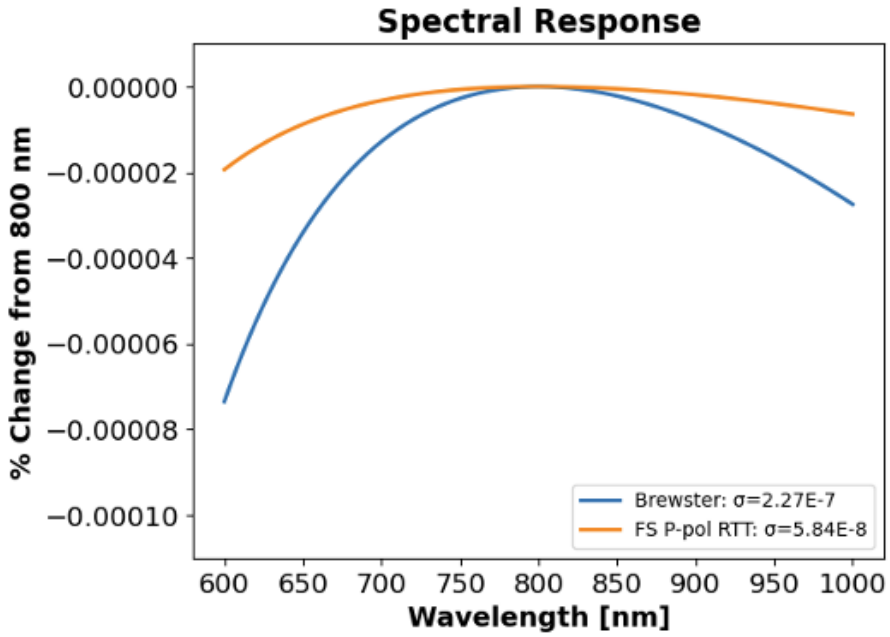

Figure 5.14: Spectral amplitude response of Brewster's angle transmission for 800 nm light through fused silica compared to the P-polarized RTT response of fused silica at the CB angle.

While the above has been for the simplest case of one reflection and two transmission events, this scheme can be extended to produce an increased number of identical pulses by including more Fresnel events. The next iteration produces fives copies of the beam by the following permutations: TTRR, RTTR, RTRT, TRTR, and RRTT. Following the same procedure as

before, the flattest amplitude distribution is given when the Fresnel reflection response is set to one-half the incident beam energy with each of the identical beam copy containing 6.25% of the original energy. In addition to lower energy per beam copy, the higher-level permutations require, in practice, a more complicated optical setup and a larger optical flat as the beam splitter. In 2019, a variation of this beam splitter concept was employed to achieve achromatic nulling in a Mach-Zender interferometer for absorption spectroscopy measurements [123]. This study used a combination of RTTTT and TTTRT Fresnel events at an angle near that for maximum efficiency, which happens to correspond to flattest spectral amplitude response as well. However, it required three separate uncoated optical flats in the experimental setup introducing an undesirable error source due to the variation in thickness. In contrast, the Michelson interferometer using the RTT and TTR Fresnel events, shown above in Fig. 5.13, is relatively simple and requires only a single uncoated optical flat beam splitter and two Brewster Porro prisms.

Residual pulse distortions

The Fresnel beam splitter arrangement produces two identical pulses that are near exact spectral copies of the input pulse with a known—to the accuracy of the measured physical dimensions of the optics—and fixed temporal distortion that in principle can be measured. For Fourier transform spectroscopy applications the dispersion of the system does not matter; however, it is a concern when using this design for several interferometric ultrafast pulse measurement applications [124, 125, 126]. The fundamental necessity here is not the complete compensation of all higher-order dispersion terms induced by the beam splitter arrangement, but the compensation of the bulk dispersion and precise knowledge of the residual higher-order terms to be numerically backed out of the pulse measurement output. With the Fresnel beam splitter arrangement this task is relatively simple as the material dispersion of the system can be analytically described and accurately measured. In contrast, this is more

difficult when using MLD coated optics due to the variable, non-analytic dispersion response and variation between coating runs.

Consider the Fresnel beam splitter arrangement shown in Fig 6. using an optical flat composed of fused silica and a 1-mm diameter, P-polarized input beam with spectrum centered at 800-nm. Here, the CB angle is 82.25-degrees. To separate the RTT beam from the TRT beam by two beam diameters requires the optical flat of at least 8-mm thickness. This thickness can be reduced, at the expense of added complexity, by including a spatial filter post-recombination to filter out the unwanted secondary beams [123]. The beam path in the BPPs is determined by construction; here we will consider typical values of an off-the-shelf model, but this can be further optimized. With a beam path in the fused silica BPPs of approximately 30-mm the total material path length for each beam copy is 40.9-mm equating to a GDD of 1479-fs^2 and a TOD of 1126-fs^3. These values are constant for any pulse measurement and can either be deconvolved from the measurement of pulses using the existing interferometer, or approximately compensated with Brewster prism pairs. For example, 1479-fs^2 of GDD can be completely compensated using a double pass two prism compressor composed of fused silica Brewster prisms separated by 777-mm with 1-mm of insertion on the first prism and 2-mm of insertion on the second prism. This would result in a pulse with a residual TOD of -636-fs^3.

Angular dispersion, in both the optical flat and BPP, will generate a spatial chirp on each of the two split pulses. The magnitude of the spatial chirp is dependent on material selection, dimensions of the optics, CB angle, center wavelength of pulse, and beam diameter. With the optics oriented as drawn in Fig. 5.13, the direction of the spatial chirp is reversed in the BPP compared to the OF. In principle, this setup can be designed so the spatial chirp in the two optics nearly cancel each other. Using the same physical arrangement as the temporal dispersion discussion, 600-nm light will be shifted by 37.3-μm from the center wavelength, a spatial chirp rate of $\sim$0.19-μm/nm, while the 1000-nm light is shifted 24.7-μm, a spatial

chirp rate of ∼0.12-μm/nm, with a majority of the spatial chirp coming from the BPP. This is well below the 1-μm/nm spatial chirp accuracy of a GENOUILLE pulse measurement system [127]. For a 1-mm diameter beam this results in an ellipticity of ∼94%. The spatial chirp is negligible for any interferometric application utilizing a single photodiode as the detector. As with the temporal dispersion, the spatial chirp is known to the accuracy of the physical dimensions of the optics used and can be numerically included in any pulse characterization algorithm.

5.4.4 Further applications

An ultra-broadband beam splitter arrangement, with spectral amplitude flatness over seven orders-of-magnitude more uniform than commercial MLD beam splitters, can be created by combining one Fresnel reflection and two Fresnel transmission events from an uncoated optical flat at the CB angle—the angle at which the one Fresnel reflection is one-third of the input beam energy—to produce three near identical pulse copies. Material selection of the optical flat and polarization state of the incoming beam are the primary variables that affect the spectral amplitude flatness and the AOI of the CB angle. While P-polarized light results in a flatter spectral response, S-polarized light allows for a greater amount of CB AOI tuning through material index of refraction selection. Here, the CB angle is inversely proportional to the material index of refraction and lower chromatic dispersion in the material results in a flatter spectral amplitude response for both polarization states. While methods to create two identical pulse pairs have existed [115], to date there has not been a way to create identical copies of the original ultra-broadband pulse.

This near-zero spectral distortion, ultra-broadband beam splitter arrangement enhances the accuracy of any Michelson interferometer optical measurement technique where the input source is also the signal to be measured. This pertains to Fourier transform spectroscopy

applications such as, but not limited to, astronomical spectroscopy [128] and atmospheric sensing [129]. For example, in stellar spectroscopy the depth of absorption line features are the primary input variables to numerical simulations that determine star temperature, chemical abundance, and atmospheric parameters; a comparative study of different codes found the absorption line depth error greater than 5% to produce unreliable results [130]. Modification to the measured spectrum will shift the relative ratio of absorption lines, as well as the absolute position of the absorption peaks and line width. This beam splitter arrangement has even greater benefit for ultrafast pulse measurement systems where knowledge of both the spectral amplitude and phase is important. Most ultrafast pulse measurement systems are essentially phase-retrieval schemes that, when combined with the spectral amplitude, allow one to calculate the profile of the temporal electric field [124, 125, 126]. If the pulse measurement system distorts the phase of the pulse it is measuring an incorrect temporal pulse profile and width will be output. This is critical for applications utilizing ultrashort pulse lasers that are sensitive to the pulse duration [131], temporal profile [132], and pulse chirp [133].

Chapter 6

Conclusion

In 2018 a report released by the National Academies of Sciences, Engineering, and Medicine titled *Opportunities in Intense Ultrafast Lasers: Reaching for the Brightest Light* [134], followed by a 2019 workshop by the U.S. Department of Energy sponsored a workshop called *Brightest Light Initiative* [135], highlighted the significant next-generation applications and science enabled by intense ultrafast lasers as well as the diminished U.S. preeminence in this field. In particular, these reports highlighted the need for the U.S. to go beyond current world leading laser systems with a user facility capable of multiple beamlines at 10-to-100 PW peak powers and co-located with a high-energy particle source. This dissertation introduces a new ultrahigh-intensity laser architecture, based on simultaneously spatially and temporally chirped beam-pulses, to go beyond the current ∼10-PW bottleneck of CPA-based laser systems and address some of the technology needs to achieve it. Contained here is the analysis of a technique called chirped pulse juxtaposed with beam amplification (CPJBA) [35], as applied to a single-amplifier NIF-like beamline, with the potential to produce an exawatt-class peak-power laser termed the Nexawatt.

The invention of CPA addressed the damage problem within the amplifier media for high-

intensity lasers. After decades of development, high-intensity CPA lasers are now limited in further peak-power increase beyond ∼10-PW by the final optic damage. A number of different methods have been put forward to address this new challenge, with almost all based on increasing the effective beam area either by larger optics or multiple beam apertures. The technique of CPJBA itself, examined in Section 3, has two goals: (i) enable the a high temporal pulse compression ratio by increasing the negative GDD induced by a fixed-aperture grating pair with the use of a chirped-beam compressor and (ii) circumvent the final optic damage problem for high-peak-power lasers by splitting the beam from a single-amplifier into multiple channels prior to recompression and cophasing the beams with a multi-mirror tiled focusing array. This technique was applied to a NIF-like amplifier beamline composed of Nd:mixed-glass that, having demonstrated extracted energy >25-kJ on NIF with a ∼20-ns stretched pulse and FTL pulse durations on the order of ∼100-fs at the Texas Petawatt and ELI-Aton, benefits from the two main purposes of CPJBA. In Section 4 the amplification of simultaneously spatially and temporally chirped beam-pulses in this NIF-like beamline was analyzed. This showed the unique pulse distortions that occur when amplifying chirped beam-pulses along with the necessary sculpting applied to both the spatio-temporal input pulse and spatial gain distribution in the amplifier. There are other amplifier systems that could potentially benefit from CPJBA as well. In particular, an OPCPA system pumped by a multi-ns Nd:glass laser may be able to produce an amplified beam with a 2x spatial chirp and the necessary bandwidth for ultrafast operation. Due to the different gain mechanism in OPCPA lasers this could possibly lessen the sculpting requirements on the input pulse.

There exist a number of technological needs beyond the amplification and compression of the chirped-beam pulse required to construct the Nexawatt system. The primary ones being the creation of a highly-temporally stretched pulse and a focusing arrangement that can phase multiple beams together. Design and analysis of these systems were put forward in Section 5. A novel version of a regenerative stretcher was presented to mitigate the sources of pre-pusle and ps-pedestal production of earlier versions while also allowing for more effi-

cient pumping [136, 100]. The core of this device is to perform a small amount of stretching over many passes in a Martinez stretcher. This design could be further enhanced by incorporating other intracavity elements that allow for the control of higher-order dispersion terms and sculpt the spectrum. This would extend its use to current 10-PW Ti:sapphire lasers that rely on Dazzlers to compensate the higher-order spectral phase and amplitude, pushing their FTL pulse duration below the current operating point of ∼20-fs. The issue of beam cophasing has largely been solved by the large-aperture telescope community [59]. A multi-segmented tiled parabolic mirror arrangement was presented with a custom Fourier propagation code showing a focused intensity $>10^{25}$ W/cm^2. Cophasing techniques such as Fizeau Interferometric Cophasing of Segmented Mirrors (FICSM) have been numerically and experimentally demonstrated to reduce wavefront errors to an RMS value on the order of several nm and Strehl ratios >∼95% [110, 111]. The multi-beam nature of CPJBA is ideal for other advanced focusing arrangements such as dipole focusing, which was simulated to produce a focused intensity $>10^{26}$ W/cm^2 when paired with a 200-PW laser split among 12 beams [57].

Another way to view the Nexawatt laser is as 36 separate ∼5.5-PW beamlines that can be coherently combined or arranged in a variety of focusing configurations. This flexibility in the far-field distribution should be required in any next-generation ultrahigh-intensity laser system of this scale to enable new experimental designs and applications. One can envision a subset of the 36 beams used to drive a high-energy particle source while the other subset generates a ultra-high intensity field for interaction. Recently, significant theoretical and modeling work has examined multi-beam, multi-source experiments as a way to study strong-field QED and probe light-matter interaction near the Schwinger limit [97, 137, 138]. Ambitious projects such as these require ambitious solutions; hopefully, some of the novel methods and technology for ultrahigh-intensity lasers discussed within this dissertation find their way to advance us closer to these goals.

Bibliography

[1] T. H. Maiman. Stimulated Optical Radiation in Ruby. *Nature*, 187(4736):493–494, 1960.

[2] F. J. McClung and R. W. Hellwarth. Giant Optical Pulsations from Ruby. *J. Appl. Phys.*, 33:828–829, 1962.

[3] L. E. Hargrove, Fork R. L., and M. A. Pollack. Locking of He-Ne Laser Modes Induced by Synchronous Intracavity Modulation. *Appl. Phys. Lett.*, 5(1):4–5, 1964.

[4] DiDomenico Jr. M. Small-Signal Analysis of Internal (Coupling-Type) Modulation of Lasers. *J. Appl. Phys.*, 35:2870–2876, 1964.

[5] A. Yariv. Internal modulation in multimode laser oscillators. *J. Appl. Phys.*, 36:388–391, 1965.

[6] H. W. Mocker and R. J. Collins. MODE COMPETITION AND SELF-LOCKING EFFECTS IN A Q-SWITCHED RUBY LASER. *Applied Physics Letters*, 7(10):270–273, 11 1965.

[7] P. A. Franken, A. E. Hill, C. W. Peters, and G. Weinreich. Generation of Optical Harmonics. *Phys. Rev. Lett.*, 7:118–119, Aug 1961.

[8] W. Kaiser and C. G. B. Garrett. Two-Photon Excitation in CaF_2: Eu^{2+}. *Phys. Rev. Lett.*, 7:229–231, Sep 1961.

[9] Donna Strickland and Gerard Mourou. Compression of amplified chirped optical pulses. *Optics Communications*, 56(3):219–221, 1985.

[10] C. P. J. Barty, C. L. Gordon, and B. E. Lemoff. Multiterawatt 30-fs Ti:sapphire laser system. *Opt. Lett.*, 19(18):1442–1444, Sep 1994.

[11] A. Sullivan, H. Hamster, H. C. Kapteyn, S. Gordon, W. White, H. Nathel, R. J. Blair, and R. W. Falcone. Multiterawatt, 100-fs laser. *Opt. Lett.*, 16(18):1406–1408, Sep 1991.

[12] A. McPherson, G. Gibson, H. Jara, U. Johann, T. S. Luk, I. A. McIntyre, K. Boyer, and C. K. Rhodes. Studies of multiphoton production of vacuum-ultraviolet radiation in the rare gases. *J. Opt. Soc. Am. B*, 4(4):595–601, Apr 1987.

[13] M Ferray, A L'Huillier, X F Li, L A Lompre, G Mainfray, and C Manus. Multiple-harmonic conversion of 1064 nm radiation in rare gases. *Journal of Physics B: Atomic, Molecular and Optical Physics*, 21(3):L31, feb 1988.

[14] C. W. Siders, S. P. Le Blanc, D. Fisher, T. Tajima, M. C. Downer, A. Babine, A. Stepanov, and A. Sergeev. Laser wakefield excitation and measurement by femtosecond longitudinal interferometry. *Phys. Rev. Lett.*, 76:3570–3573, May 1996.

[15] M. D. Perry, D. Pennington, B. C. Stuart, G. Tietbohl, J. A. Britten, C. Brown, S. Herman, B. Golick, M. Kartz, J. Miller, H. T. Powell, M. Vergino, and V. Yanovsky. Petawatt laser pulses. *Opt. Lett.*, 24(3):160–162, Feb 1999.

[16] M. W. L. Seggebruch, H. H. Effarah, E. Nelson, and C. P. J Barty. ICUIL World Map. `https://www.icuil.org/activities/laser-labs.html`, 2020.

[17] F. Lureau, G. Matras, O. Chalus, C. Derycke, T. Morbieu, C. Radier, O. Casagrande, S. Laux, S. Ricaud, G. Rey, A. Pellegrina, C. Richard, L. Boudjemaa, C. Simon-Boisson, A. Baleanu, R. Banici, A. Gradinariu, C. Caldararu, B. De Boisdeffre, P. Ghenuche, A. Naziru, G. Kolliopoulos, L. Neagu, R. Dabu, I. Dancus, and D. Ursescu. High-energy hybrid femtosecond laser system demonstrating 2 × 10 PW capability. *High Power Laser Science and Engineering*, 8, 2020.

[18] J. H. Sung, H. W. Lee, J. Y. Yoo, J. W. Yoon, C. W. Lee, J. M. Yang, Y. J. Son, Y. H. Jang, S. K. Lee, and C. H. Nam. 4.2 PW, 20 fs Ti:sapphire laser at 0.1 Hz. *Opt Lett*, 42(11):2058–2061, 2017.

[19] Z. Gan, L. Yu, S. Li, C. Wang, X. Liang, Y. Liu, W. Li, Z. Guo, Z. Fan, X. Yuan, L. Xu, Z. Liu, Y. Xu, J. Lu, H. Lu, D. Yin, Y. Leng, R. Li, and Z. Xu. 200 J high efficiency Ti:sapphire chirped pulse amplifier pumped by temporal dual-pulse. *Opt Express*, 25(5):5169–5178, 2017.

[20] H. Azechi, K. Mima, Y. Fujimoto, S. Fujioka, H. Homma, M. Isobe, A. Iwamoto, T. Jitsuno, T. Johzaki, R. Kodama, M. Koga, K. Kondo, J. Kawanaka, T. Mito, N. Miyanaga, O. Motojima, M. Murakami, H. Nagatomo, K. Nagai, M. Nakai, H. Nakamura, T. Nakamura, T. Nakazato, Y. Nakao, K. Nishihara, H. Nishimura, T. Norimatsu, T. Ozaki, H. Sakagami, Y. Sakawa, N. Sarukura, K. Shigemori, T. Shimizu, H. Shiraga, A. Sunahara, T. Taguchi, K.A. Tanaka, and K. Tsubakimoto. Plasma physics and laser development for the Fast-Ignition Realization Experiment (FIREX) Project. *Nuclear Fusion*, 49(10):104024, sep 2009.

[21] J. W. Yoon, Y. G. Kim, I. W. Choi, J. H. Sung, H. W. Lee, S. K. Lee, and C. H. Nam. Realization of laser intensity over 10^{23} W/cm^2. *Optica*, 8(5), 2021.

[22] A. Di Piazza, L. Willingale, and J. D. Zuegel. Multi-petawatt Physics Prioritization (MP3) Workshop Report, 2022.

[23] W. Li, Z. Gan, L. Yu, C. Wang, Y. Liu, Z. Guo, L. Xu, M. Xu, Y. Hang, Y. Xu, J. Wang, P. Huang, H. Cao, B. Yao, X. Zhang, L. Chen, Y. Tang, S. Li, X. Liu, S. Li,

M. He, D. Yin, X. Liang, Y. Leng, R. Li, and Z. Xu. 339 J high-energy Ti:sapphire chirped-pulse amplifier for 10 PW laser facility. *Opt Lett*, 43(22):5681–5684, 2018.

[24] B. Rus, P. Bakule, D. Kramer, J. Naylon, J. Thoma, J.T. Green, R. Antipenkov, M. Fibrich, J. Novák, F. Batysta, T. Mazanec, M. A. Drouin, K. Kasl, R. Baše, D. Peceli, L. Koubíková, P. Trojek, R. Boge, J. C. Lagron, Å. Vyhlídka, J. Weiss, J. Cupal, J. Hřebíček, P. Hříbek, M. Durák, J. Polan, M. Košelja, G. Korn, M. Horáček, J. Horáček, B. Himmel, T. Havlíček, A. Honsa, P. Korouš, M. Laub, C. Haefner, A. Bayramian, T. Spinka, C. Marshall, G. Johnson, S. Telford, J. Horner, B. Deri, T. Metzger, M. Schultze, P. Mason, K. Ertel, A. Lintern, J. Greenhalgh, C. Edwards, C. Hernandez-Gomez, J. Collier, T. Ditmire, E. Gaul, M. Martinez, C. Frederickson, D. Hammond, C. Malato, W. White, and J. Houžvička. ELI-Beamlines: development of next generation short-pulse laser systems. In Georg Korn and Luis O. Silva, editors, *Research Using Extreme Light: Entering New Frontiers with Petawatt-Class Lasers II*, volume 9515 of *Society of Photo-Optical Instrumentation Engineers (SPIE) Conference Series*, page 95150F, May 2015.

[25] C. Hernandez-Gomez, S. P. Blake, O. Chekhlov, R. J. Clarke, A. M. Dunne, M. Galimberti, S. Hancock, R. Heathcote, P. Holligan, A. Lyachev, P. Matousek, I. O. Musgrave, D. Neely, P. A. Norreys, I. Ross, Y. Tang, T. B. Winstone, B. E. Wyborn, and J. Collier. The Vulcan 10 PW project. *Journal of Physics: Conference Series*, 244(3):032006, aug 2010.

[26] D.N. Papadopoulos, J.P. Zou, C. Le Blanc, G. Cheriaux, P. Georges, F. Druon, G. Mennerat, P. Ramirez, L. Martin, A. Freneaux, and et al. The Apollon 10 PW laser: experimental and theoretical investigation of the temporal characteristics. *High Power Laser Science and Engineering*, 4:e34, 2016.

[27] J. Bromage, S. W. Bahk, M. Bedzyk, I. A. Begishev, S. Bucht, C. Dorrer, C. Feng, C. Jeon, C. Mileham, R. G. Roides, K. Shaughnessy, III Shoup, M. J., M. Spilatro, B. Webb, D. Weiner, and J. D. Zuegel. MTW-OPAL: a technology development platform for ultra-intense optical parametric chirped-pulse amplification systems. *High Power Laser Science and Engineering*, 9:e63, January 2021.

[28] C. N. Danson, C. Haefner, J. Bromage, T. Butcher, J.-C. F. Chanteloup, E. A. Chowdhury, A. Galvanauskas, L. A. Gizzi, J. Hein, D. I. Hillier, N. W. Hopps, Y. Kato, E. A. Khazanov, R. Kodama, G. Korn, R. Li, Y. Li, J. Limpert, J. Ma, C. H. Nam, D. Neely, D. Papadopoulos, R. R. Penman, L. Qian, J. J. Rocca, A. A. Shaykin, C. W. Siders, C. Spindloe, S. Szatmári, R. M. G. M. Trines, J. Zhu, P. Zhu, and J. D. Zuegel. Petawatt and exawatt class lasers worldwide. *High Power Laser Science and Engineering*, 7, 2019.

[29] G. A. Mourou, K. Georg, W. Sander, and J. L. Collier. ELI Whitebook. *THOSS Media*, 2011.

[30] A. V. Bashinov, A. A. Gonoskov, A. V. Kim, G. Mourou, and A. M. Sergeev. New horizons for extreme light physics with mega-science project XCELS. *Eur. Phys. J. ST*, 223(6):1105–1112, 2014.

[31] T. J. Kessler, J. Bunkenburg, H. Huang, A. Kozlov, and D. D. Meyerhofer. Demonstration of coherent addition of multiple gratings for high-energy chirped-pulse-amplified lasers. *Opt. Lett.*, 29(6):635–637, Mar 2004.

[32] Z. Li, S. Li, C. Wang, Y. Xu, F. Wu, Y. Li, and Y. Leng. Stable and near fourier-transform-limit 30fs pulse compression with a tiled grating compressor scheme. *Opt Express*, 23(26):33386–95, 2015.

[33] M. S. Hur, B. Ersfeld, H. Lee, H. Kim, K. Roh, Y. Lee, H. S. Song, M. Kumar, S. Yoffe, D. A. Jaroszynski, and H. Suk. Laser pulse compression by a density gradient plasma for exawatt to zettawatt lasers. *Nature Photonics*, 17(12):1074–1079, 2023.

[34] C. P. J. Barty. Optical chirped beam amplification and propagation. *U.S. Patent 6804045 B2*, 2004.

[35] C. P. J. Barty. The Nexawatt: A strategy for exawatt peak power lasers based on NIF and NIF-like beam lines. *Journal of Physics: Conference Series*, 717(1):012086, May 2016.

[36] T. Blasiak and S. Zheleznyak. History and construction of large mosaic diffraction gratings. In Allen M. Larar and Martin G. Mlynczak, editors, *Optical Spectroscopic Techniques, Remote Sensing, and Instrumentation for Atmospheric and Space Research IV*, volume 4485, pages 370 – 377. International Society for Optics and Photonics, SPIE, 2002.

[37] M. Cong, X. Qi, J. Xu, C. Qiao, X. Mi, X. Li, H. Yu, S. Zhahng, H. Yu, and Bayanheshig. Analysis and removal of five-dimensional mosaicking errors in mosaic grating. *Opt Express*, 27(3):1968–1980, 2019.

[38] G. Yang, X. Qi, X. Mi, S. Zhang, H. Yu, H. Yu, X. Li, and S. Yang. Numerical calculation of the mosaic error between mosaic gratings. *Appl Opt*, 59(13):4048–4054, 2020.

[39] A. Cotel, M. Castaing, P. Pichon, and C. Le Blanc. Phased-array grating compression for high-energy chirped pulse amplification lasers. *Opt. Express*, 15(5):2742–2752, Mar 2007.

[40] F. G. Patterson, J. Bonlie, D. Price, and B. White. Suppression of parasitic lasing in large-aperture Ti:sapphire laser amplifiers. *Opt. Lett.*, 24(14):963–965, Jul 1999.

[41] K. Ertel, C. Hooker, S. J. Hawkes, B. T. Parry, and J. L. Collier. Ase suppression in a high energy titanium sapphire amplifier. *Opt. Express*, 16(11):8039–8049, May 2008.

[42] S. Laux, F. Lureau, C. Radier, O. Chalus, F. Caradec, O. Casagrande, E. Pourtal, C. Simon-Boisson, F. Soyer, and P. Lebarny. Suppression of parasitic lasing in high energy, high repetition rate Ti:sapphire laser amplifiers. *Opt. Lett.*, 37(11):1913–1915, Jun 2012.

[43] Y. Liu, K. Liu, Z. Li, Y. Leng, and R. Li. Coherently tiled Ti:sapphire laser amplification: a way to break the 10 petawatt limit on current ultraintense lasers. *Advanced Photonics Nexus*, 2(06), 2023.

[44] Z. Li, Y. Kato, and J. Kawanaka. Simulating an ultra-broadband concept for exawatt-class lasers. *Sci Rep*, 11(1):151, 2021.

[45] J. Soures, S. Kumpan, and J. Hoose. High power Nd:glass laser for fusion applications. *Appl. Opt.*, 13(9):2081–2094, Sep 1974.

[46] J. Campbell and T. Suratwala. Nd-doped phosphate glasses for high-energy/high-peak-power lasers. *Journal of Non-Crystalline Solids*, 263:318–341, 03 2000.

[47] C. A. Haynam, P. J. Wegner, J. M. Auerbach, M. W. Bowers, S. N. Dixit, G. V. Erbert, G. M. Heestand, M. A. Henesian, M. R. Hermann, K. S. Jancaitis, K. R. Manes, C. D. Marshall, N. C. Mehta, J. Menapace, E. Moses, J. R. Murray, M. C. Nostrand, C. D. Orth, R. Patterson, R. A. Sacks, M. J. Shaw, M. Spaeth, S. B. Sutton, W. H. Williams, C. C. Widmayer, R. K. White, S. T. Yang, and B. M. Van Wonterghem. National ignition facility laser performance status. *Appl. Opt.*, 46(16):3276–3303, Jun 2007.

[48] J. Neauport, J. P. Airiau, N. Beck, N. Belon, E. Bordenave, S. Bouillet, M. Chanal, C. Chappuis, H. Coic, R. Courchinoux, V. Denis, F. Gaudfrin, K. Gaudfrin, P. Gendeau, L. Heymans, X. Julien, C. Lacombe, M. Lamy, D. Lebeaux, M. Luttmann, P. Modelin, A. Perrin, X. Ribeyre, C. Rouyer, F. Tournemenne, D. Valla, and S. Vermersch. Laser megajoule performance status. *Appl Opt*, 63(16):4447–4464, 2024.

[49] N. Jourdain, U. Chaulagain, M. Havlík, D. Kramer, D. Kumar, I. Majerová, V. T. Tikhonchuk, G. Korn, and S. Weber. The L4n laser beamline of the P3-installation: Towards high-repetition rate high-energy density physics at ELI-beamlines. *Matter and Radiation at Extremes*, 6(1), 2021.

[50] B. Reagan, M. Albrecht, D. Alessi, M. Ammons, S. Banerjee, C. Barillas, F. Batysta, B. Buckley, A. Chemali, E. Clark, E. Davila, R. Deri, K. Eseltine, B. Fishler, S. Fulkerson, J. Galbraith, T. Galvin, A. Gonzales, V. Gopal, and N. Wong. High repetition rate, high energy petawatt laser for the matter in extreme conditions upgrade. In *Proc. of SPIE*, page 17, 03 2023.

[51] B. Wonterghem, S. Burkhart, C. Haynam, K. Manes, C. Marshall, J. Murray, M. Spaeth, D. Speck, S. Sutton, and P. Wegner. National Ignition Facility commissioning and performance. *Proc SPIE*, 01 2004.

[52] G. R. Hays, E. W. Gaul, M. D. Martinez, and T. Ditmire. Broad-spectrum neodymium-doped laser glasses for high-energy chirped-pulse amplification. *Appl. Opt.*, 46(21):4813–4819, Jul 2007.

[53] E. B. Treacy. Optical pulse compression with diffraction gratings. *IEEE Journal of Quantum Electronics*, 5:454–458, 1969.

[54] J. Britten, W. Molander, A. Komashko, and C. Barty. Multilayer dielectric gratings for petawatt-class laser systems. *Proceedings of SPIE - The International Society for Optical Engineering*, 06 2004.

[55] J. A. Britten. Diffraction gratings for high-intensity laser applicatoins. *LLNL-BOOK-401125*, 2008.

[56] D. A. Alessi, C. W. Carr, R. P. Hackel, R. A. Negres, K. Stanion, J. E. Fair, D. A. Cross, J. Nissen, R. Luthi, G. Guss, J. A. Britten, W. H. Gourdin, and C. Haefner. Picosecond laser damage performance assessment of multilayer dielectric gratings in vacuum. *Opt Express*, 23(12):15532–44, 2015.

[57] A. Gonoskov, A. Bashinov, I. Gonoskov, C. Harvey, A. Ilderton, A. Kim, M. Marklund, G. Mourou, and A. Sergeev. Anomalous radiative trapping in laser fields of extreme intensity. *Phys Rev Lett*, 113(1):014801, 2014.

[58] E. C. Nelson. Multi-beam focusing. *TBD*, 2024.

[59] I. Trumper, P. Hallibert, J. W. Arenberg, H. Kunieda, O. Guyon, H. P. Stahl, and D. W. Kim. Optics technology for large-aperture space telescopes: From fabrication to final acceptance tests. *Advances in Optics and Photonics*, 10(3), 2018.

[60] A.E. Siegman. *Lasers*. University Science Books, 1986.

[61] J-C Diels and W. Rudolph. *Ultrashort Laser Pulse Phenomena*. Elsevier, 2006.

[62] F. Dominec. Laser resonator stability. `https://commons.wikimedia.org/wiki/File:Laser_resonator_stability.svg`, 2007.

[63] W. Koechner. *Solid-State Laser Engineering*. Springer, 2006.

[64] L. M. Frantz and J. S. Nodvik. Theory of Pulse Propagation in a Laser Amplifier. *Journal of Applied Physics*, 34(8):2346–2349, 08 1963.

[65] U. Keller. *Ultrafast Lasers: A Comprehensive Introduction to Fundamental Principles with Practical Applications*. Springer, 2021.

[66] R. Trebino. *Frequency-Resolved Optical Gating: The Measurement of Ultrashort Laser Pulses*. Springer, 2002.

[67] Xun Gu, Selcuk Akturk, and Rick Trebino. Spatial chirp in ultrafast optics. *Optics Communications*, 242:599–604, 12 2004.

[68] S. D. Brorson and H. A. Haus. Diffraction gratings and geometrical optics. *J. Opt. Soc. Am. B*, 5(2):247–248, Feb 1988.

[69] O. Martinez. 3000 times grating compressor with positive group velocity dispersion: Application to fiber compensation in 1.3-1.6 µm region. *IEEE Journal of Quantum Electronics*, 23(1):59–64, 1987.

[70] B. E. Lemoff and C. P. J. Barty. Quintic-phase-limited, spatially uniform expansion and recompression of ultrashort optical pulses. *Opt. Lett.*, 18(19):1651–1653, Oct 1993.

[71] G. Cheriaux, B. Walker, L. F. Dimauro, P. Rousseau, F. Salin, and J. P. Chambaret. Aberration-free stretcher design for ultrashort-pulse amplification. *Optics Letters*, 21(6):414–416, March 1996.

[72] C.P.J. Barty, M. Key, J. Britten, R. Beach, G. Beer, C. Brown, S. Bryan, J. Caird, T. Carlson, J. Crane, J. Dawson, A.C. Erlandson, D. Fittinghoff, M. Hermann, C. Hoaglan, A. Iyer, L. Jones, I. Jovanovic, A. Komashko, O. Landen, Z. Liao, W. Molander, S. Mitchell, E. Moses, N. Nielsen, H-H. Nguyen, J. Nissen, S. Payne, D. Pennington, L. Risinger, M. Rushford, K. Skulina, M. Spaeth, B. Stuart, G. Tietbohl, and B. Wattellier. An overview of LLNL high-energy short-pulse technology for advanced radiography of laser fusion experiments. *Nuclear Fusion*, 44(12):S266, nov 2004.

[73] T. Erdogan. Conversation on grating size. *Conversation*, 2022.

[74] Y. Han, Z. Li, Y. Zhang, F. Kong, H. Cao, Y. Jin, Y. Leng, R. Li, and J. Shao. 400nm ultra-broadband gratings for near-single-cycle 100 petawatt lasers. *Nat Commun*, 14(1):3632, 2023.

[75] W. Simmons, J. Hunt, and W. Warren. Light propagation through large laser systems. *IEEE Journal of Quantum Electronics*, 17(9):1727–1744, 1981.

[76] C. C. Widmayer, J. M. Auerbach, R. B. Ehrlich, M. A. Henesian, J. T. Hunt, J. K. Lawson, D. Milam, P. A. Renard, D. R. Speck, P. J. Wegner, T. L. Weiland, W. H. Williams, C. R. Wolfe, , and B. M. Van Wonterghem. Producing National Ignition Facility (NIF)-Quality Beams on the Nova and Beamlet Lasers. *Fusion Technology*, 30(3P2A):464–470, 1996.

[77] B. M. Van Wonterghem, J. R. Murray, J. H. Campbell, D. R. Speck, C. E. Barker, I. C. Smith, D. F. Browning, and W. C. Behrendt. Performance of a prototype for a large-aperture multipass Nd:glass laser for inertial confinement fusion. *Appl. Opt.*, 36(21):4932–4953, Jul 1997.

[78] M. L. Spaeth, K. R. Manes, D. H. Kalantar, P. E. Miller, J. E. Heebner, E. S. Bliss, D. R. Spec, T. G. Parham, P. K. Whitman, P. J. Wegner, P. A. Baisden, J. A. Menapace, M. W. Bowers, S. J. Cohen, T. I. Suratwala, J. M. Di Nicola, M. A. Newton, J. J. Adams, J. B. Trenholme, R. G. Finucane, R. E. Bonanno, D. C. Rardin, P. A. Arnold, S. N. Dixit, G. V. Erbert, A. C. Erlandson, J. E. Fair, E. Feigenbaum, W. H. Gourdin, R. A. Hawley, J. Honig, R. K. House, K. S. Jancaitis, K. N. LaFortune, D. W. Larson, B. J. Le Galloudec, J. D. Lindl, B. J. MacGowan, C. D. Marshall, K. P. McCandless, R. W. McCracken, R. C. Montesanti, E. I. Moses, M. C. Nostrand, J. A. Pryatel, V. S. Roberts, S. B. Rodriguez, A. W. Rowe, R. A. Sacks, J. T. Salmon, M. J. Shaw, S. Sommer, C. J. Stolz, G. L. Tietbohl, C. C. Widmayer, and R. Zacharias. Description of the NIF Laser. *Fusion Science and Technology*, 69(1):25–145, 2016.

[79] LightTrans GmbH. Wyrowski VirtualLab Fusion: Technology Whitepapers. `https://www.lighttrans.com/resources/downloads.html`, 2021.

[80] G. Van Rossum and F. L. Drake Jr. *Python reference manual*. Centrum voor Wiskunde en Informatica Amsterdam, 1995.

[81] B. Webb, M. J. Guardalben, C. Dorrer, S. Bucht, and J. Bromage. Simulation of grating compressor misalignment tolerances and mitigation strategies for chirped-pulse-amplification systems of varying bandwidths and beam sizes. *Appl. Opt.*, 58(2):234–243, 2019.

[82] J. Jeong, S. Cho, S. Hwang, B. Lee, and T. J. Yu. Modeling and analysis of high-power Ti:sapphire laser amplifiers – a Review. *Applied Sciences*, 9(12), 2019.

[83] T. Suratwala, J. Campbell, P. Miller, C. Thorsness, M. Riley, P. Ehrmann, and R. Steele. Phosphate laser glass for NIF: Production status, slab selection and recent technical advances. *Proc SPIE*, 5341, 05 2004.

[84] S. W. Haney, W. H. Williams, R. A. Sacks, C. D. Orth, J. M. Auerbach, J. K. Lawson, M. A. Henesian, K. S. Jancaitis, P. A. Renard, and J. B. Trenholme. Optimized NIF laser system based on ICF target requirements. In Michel L. Andre, editor, *Solid State Lasers for Application to Inertial Confinement Fusion: Second Annual International Conference*, volume 3047 of *Society of Photo-Optical Instrumentation Engineers (SPIE) Conference Series*, pages 546–559, December 1997.

[85] J. Caird, V. Agrawal, A. Bayramian, R. Beach, J. Britten, D. Chen, R. Cross, C. Ebbers, A. Erlandson, M. Feit, B. Freitas, C. Ghosh, C. Haefner, D. Homoelle, T. Ladran, J. Latkowski, W. Molander, J. Murray, S. Rubenchik, K. Schaffers, C. Siders, E. Stappaerts, S. Sutton, S. Telford, J. Trenholme, and C. Barty. Nd:Glass Laser Design for Laser ICF Fission Energy (LIFE). *Fusion Science and Technology*, 56(2):607–617, August 2009.

[86] D. F. Hotz. Gain narrowing in a laser amplifier. *Appl. Opt.*, 4(5):527–530, May 1965.

[87] A. Y. Cabezas, G. L. McAllister, and W. K. Ng. Gain Saturation in Neodymium: Glass Laser Amplifiers. *Journal of Applied Physics*, 38(9):3487–3491, 08 1967.

[88] D. N. Schimpf, C. Ruchert, D. Nodop, J. Limpert, A. Tünnermann, and F. Salin. Compensation of pulse-distortion in saturated laser amplifiers. *Opt. Express*, 16(22):17637–17646, Oct 2008.

[89] F. Batysta, R. Antipenkov, T. Borger, A. Kissinger, J. T. Green, R. Kananavicius, G. Cheriaux, D. Hidinger, J. Kolenda, E. Gaul, B. Rus, and T. Ditmire. Spectral pulse shaping of a 5 Hz, multi-joule, broadband optical parametric chirped pulse amplification frontend for a 10 PW laser system. *Opt Lett*, 43(16):3866–3869, 2018.

[90] H. W. Lee, Y. G. Kim, J. Y. Yoo, J. W. Yoon, J. M. Yang, H. Lim, C. H. Nam, J. H. Sung, and S. K. Lee. Spectral shaping of an OPCPA preamplifier for a sub-20-fs multi-PW laser. *Opt Express*, 26(19):24775–24783, 2018.

[91] S. Korman, E. Bahar, U. Arieli, and H. Suchowski. Spatio-temporal ultrafast pulse shaping at the femtosecond-nanometer scale. *Opt Lett*, 47(17):4279–4282, 2022.

[92] Qiwen Zhan. Spatiotemporal sculpturing of light: a tutorial. *Advances in Optics and Photonics*, 16(2), 2024.

[93] J. Heebner, M. Borden, P. Miller, S. Hunter, K. Christensen, M. Scanlan, C. Haynam, P. Wegner, M. Hermann, G. Brunton, E. Tse, A. Awwal, N. Wong, L. Seppala, M. Franks, E. Marley, K. Williams, T. Budge, M. Henesian, and J-M Dinicola. Programmable Beam Spatial Shaping System for the National Ignition Facility. *Proc SPIE*, 7916:11–, 02 2011.

[94] J. E. Heebner, Jr. Acree, R. L., D. A. Alessi, A. I. Barnes, M. W. Bowers, D. F. Browning, T. S. Budge, S. Burns, L. S. Chang, K. S. Christensen, J. K. Crane, M. Dailey, G. V. Erbert, M. Fischer, M. Flegel, B. P. Golick, J. M. Halpin, M. Y. Hamamoto, M. R. Hermann, V. J. Hernandez, J. Honig, J. A. Jarboe, D. H. Kalantar, V. K. Kanz, K. M. Knittel, J. R. Lusk, W. A. Molander, V. R. Pacheu, M. Paul, L. J. Pelz, M. A. Prantil, M. C. Rushford, N. Schenkel, R. J. Sigurdsson, T. M. Spinka, M. G. Taranowski, P. J. Wegner, K. C. Wilhelmsen, J. Nan Wong, and S. T. Yang. Injection laser system for Advanced Radiographic Capability using chirped pulse amplification on the National Ignition Facility. *Appl. Opt.*, 58(31):8501–8510, 2019.

[95] E. W. Gaul, M. Martinez, J. Blakeney, A. Jochmann, M. Ringuette, D. Hammond, T. Borger, R. Escamilla, S. Douglas, W. Henderson, G. Dyer, A. Erlandson, R. Cross, J. Caird, C. Ebbers, and T. Ditmire. Demonstration of a 1.1 petawatt laser based on a hybrid optical parametric chirped pulse amplification/mixed Nd:glass amplifier. *Appl. Opt.*, 49(9):1676–1681, Mar 2010.

[96] G. Mourou. Nobel Lecture: Extreme light physics and application. *Reviews of Modern Physics*, 91(3), 2019.

[97] Kenan Qu and Nathaniel J. Fisch. Creating and detecting observable QED plasmas through beam-driven cascade. *Physics of Plasmas*, 31(6):062102, 06 2024.

[98] X. Lu, H. Zhang, J. Li, and Y. Leng. Reducing temporal pedestal in a ti:sapphire chirped-pulse amplification system by using a stretcher based on two concave mirrors. *Opt Lett*, 46(21):5320–5323, 2021.

[99] Simon Roeder, Yannik Zobus, Christian Brabetz, and Vincent Bagnoud. How the laser beam size conditions the temporal contrast in pulse stretchers of chirped-pulse amplification lasers. *High Power Laser Science and Engineering*, 10, 2022.

[100] H. Su, Y. Peng, Y. Li, X. Lu, J. Chen, P. Wang, X. Lv, B. Shao, and Y. Leng. Multipass active stretcher with large chirp for high-flux ultra-intense lasers. *Opt. Lett.*, 44(8):1980–1983, 2019.

[101] N.V. Didenko, A.V. Konyashchenko, A.P. Lutsenko, and S.Yu. Tenyakov. Contrast degradation in a chirped-pulse amplifier due to generation of prepulses by postpulses. *Opt. Express*, 16(5):3178–3190, Mar 2008.

[102] H. Kiriyama, Y. Miyasaka, A. Sagisaka, K. Ogura, M. Nishiuchi, A. S. Pirozhkov, Y. Fukuda, M. Kando, and K. Kondo. Experimental investigation on the temporal contrast of pre-pulses by post-pulses in a petawatt laser facility. *Opt Lett*, 45(5):1100–1103, 2020.

[103] S. Kane and J. Squier. Fourth-order-dispersion limitations of aberration-free chirped-pulse amplification systems. *J. Opt. Soc. Am. B*, 14(5):1237–1244, May 1997.

[104] W. H. Williams, J. K. Crane, D. A. Alessi, C. D. Boley, M. W. Bowers, A. D. Conder, J. G. Di Nicola, P. Di Nicola, C. Haefner, J. M. Halpin, M. Y. Hamamoto, J. E. Heebner, M. R. Hermann, S. I. Herriot, D. C. Homoelle, D. H. Kalantar, T. E. Lanier, K. N. LaFortune, J. K. Lawson, R. R. Lowe-Webb, F. X. Morrissey, H. Nguyen, C. D. Orth, L. J. Pelz, M. A. Prantil, M. C. Rushford, R. A. Sacks, J. T. Salmon, L. G. Seppala, M. J. Shaw, R. J. Sigurdsson, P. J. Wegner, C. C. Widmayer, S. T. Yang, and T. L. Zobrist. Spatio-temporal focal spot characterization and modeling of the NIF ARC kilojoule picosecond laser. *Appl. Opt.*, 60(8):2288–2303, 2021.

[105] H. M. Martin, R. G. Allen, J. H. Burge, J. M. Davis, W. B. Davison, M. Johns, D. W. Kim, J. S. Kingsley, K. Law, R. D. Lutz, P. A. Strittmatter, P. Su, M. T. Tuell, S. C. West, and P. Zhou. Production of primary mirror segments for the Giant Magellan Telescope. In Ramón Navarro, Colin R. Cunningham, and Allison A. Barto, editors, *Advances in Optical and Mechanical Technologies for Telescopes and Instrumentation*, volume 9151 of *Society of Photo-Optical Instrumentation Engineers (SPIE) Conference Series*, page 91510J, Jul 2014.

[106] D.G. Voelz. *Computational Fourier Optics: A MATLAB Tutorial*. SPIE, 2011.

[107] Y. Hu, Z. Wang, X. Wang, S. Ji, C. Zhang, J. Li, W. Zhu, D. Wu, and J. Chu. Efficient full-path optical calculation of scalar and vector diffraction using the Bluestein method. *Light: Science & Applications*, 9(1):119, Dec 2020.

[108] G. Chanan, M. Troy, and E. Sirko. Phase Discontinuity Sensing: A Method for Phasing Segmented Mirrors in the Infrared. *Applied Optics*, 38(4):704–713, Feb 1999.

[109] G. Chanan, M. Troy, I. Surdej, G. Gutt, and Jr. Roberts, L. C. Fresnel phasing of segmented mirror telescopes. *Applied Optics*, 50(33):6283, Nov 2011.

[110] A. C. Cheetham, P. G. Tuthill, A. Sivaramakrishnan, and J. P. Lloyd. Fizeau interferometric cophasing of segmented mirrors. *Optics Express*, 20(28):29457, Dec 2012.

[111] A. Cheetham, N. Cvetojevic, B. Norris, A. Sivaramakrishnan, and P. Tuthill. Fizeau interferometric cophasing of segmented mirrors: experimental validation. *Optics Express*, 22(11):12924, Jun 2014.

[112] R. J. Bell. *Introductory Fourier Transform Spectroscopy*. Academic PRess Inc., 1972.

[113] R. Trebino, R. Jafari, S. A. Akturk, P. Bowlan, Z. Guang, P. Zhu, E. Escoto, and G. Steinmeyer. Highly reliable measurement of ultrashort laser pulses. *Journal of Applied Physics*, 128(17), 2020.

[114] J. Kim, Jonathan R. Birge, V. Sharma, J. G. Fujimoto, F. X. Kärtner, V. Scheuer, and G. Angelow. Ultrabroadband beam splitter with matched group-delay dispersion. *Opt. Lett.*, 30(12):1569–1571, Jun 2005.

[115] C. P. J. Barty, B. E. Lemoff, and C. L. Gordon III. Generation, measurement, and amplification of 20-fs high-peak-power pulses from a regeneratively initiated, self-mode-locked Ti:sapphire laser. In Timothy R. Gosnell, Antoinette J. Taylor, Keith A. Nelson, and Michael C. Downer, editors, *Ultrafast Pulse Generation and Spectroscopy*, volume 1861, pages 6 – 30. International Society for Optics and Photonics, SPIE, 1993.

[116] G. Steinmeyer. Dispersion oscillations in ultrafast phase-correction devices. *IEEE Journal of Quantum Electronics*, 39(8):1027–1034, 2003.

[117] G. Steinmeyer. Femtosecond dispersion compensation with multilayer coatings: toward the optical octave. *Appl. Opt.*, 45(7):1484–1490, Mar 2006.

[118] T. A. Laurence, D. A. Alessi, E. Feigenbaum, R. A. Negres, S. R. Qiu, C. W. Siders, T. M. Spinka, and C. J. Stolz. Mirrors for petawatt lasers: Design principles, limitations, and solutions. *Journal of Applied Physics*, 128(7), 2020.

[119] E. Hecht. *Optics 5th Ed.* Pearson Publishing Inc., 2015.

[120] ThorLabs. Ultrafast beamsplitter ufb5050 raw data. `https://www.thorlabs.com/images/tabimages/UFB505002_data.xlsx`, 2023.

[121] M. N. Polyanskiv. Refractive index database. `https://refractiveindex.info`, 2023.

[122] H. Moosmüller. Brewster's Angle Porro Prism: A Different Use for a Pellin-Broca Prism. *Appl. Opt.*, 37(34):8140–8141, Dec 1998.

[123] T. Buberl, P. Sulzer, A. Leitenstorfer, F. Krausz, and I. Pupeza. Broadband interferometric subtraction of optical fields. *Opt. Express*, 27(3):2432–2443, 2019.

[124] J.-C. M. Diels, J. J. Fontaine, I. C. McMichael, and F. Simoni. Control and measurement of ultrashort pulse shapes (in amplitude and phase) with femtosecond accuracy. *Appl. Opt.*, 24(9):1270–1282, May 1985.

[125] D.J. Kane and R. Trebino. Characterization of arbitrary femtosecond pulses using frequency-resolved optical gating. *IEEE Journal of Quantum Electronics*, 29(2):571–579, 1993.

[126] C. Iaconis and I. A. Walmsley. Spectral phase interferometry for direct electric-field reconstruction of ultrashort optical pulses. *Opt. Lett.*, 23(10):792–794, May 1998.

[127] Swamp Optics. Near-ir genouilles. `https://www.swampoptics.com/assest/brochure-near-ir-genouilles-2020-01.pdf.`, 2020.

[128] S. T. Ridgway and J. W. Brault. Astronomical Fourier Transform Spectroscopy Revisited. *Ann. Rev. of Astro. and Astrophys.*, 22:291–317, January 1984.

[129] J. Mink Z. Bacsik and G. Keresztury. FTIR Spectroscopy of the Atmosphere. I. Principles and Methods. *Applied Spectroscopy Reviews*, 39(3):295–363, 2004.

[130] S. Blanco-Cuaresma. Modern stellar spectroscopy caveats. *Monthly Notices of the Royal Astronomical Society*, 486(2):2075–2101, 2019.

[131] A. Das, A. Wang, O. Uteza, and D. Grojo. Pulse-duration dependence of laser-induced modifications inside silicon. *Opt. Express*, 28(18):26623–26635, Aug 2020.

[132] M. D. Perry, T. Ditmire, and B. C. Stuart. Self-phase modulation in chirped-pulse amplification. *Opt. Lett.*, 19(24):2149–2151, Dec 1994.

[133] A. Jain and D. N. Gupta. Optimization of electron bunch quality using a chirped laser pulse in laser wakefield acceleration. *Phys. Rev. Accel. Beams*, 24:111302, Nov 2021.

[134] National Academies of Sciences Engineering and Medicine. *Opportunities in Intense Ultrafast Lasers: Reaching for the Brightest Light*. The National Academies Press, Washington, DC, 2018.

[135] R. Falcone, F. Albert, F. Beg, S. Glenzer, T. Ditmire, T. Spinka, and J. Zuegel. Workshop Report: Brightest Light Initiative (March 27-29 2019, OSA Headquarters, Washington, D.C.). *arXiv e-prints*, page arXiv:2002.09712, Feb 2020.

[136] H. Liebetrau, M. Hornung, S. Keppler, M. Hellwing, A. Kessler, F. Schorcht, J. Hein, and M. C. Kaluza. Intracavity stretcher for chirped-pulse amplification in high-power laser systems. *Opt. Lett.*, 42(2):326–329, 2017.

[137] J. Magnusson, A. Gonoskov, M. Marklund, T. Zh Esirkepov, J. K. Koga, K. Kondo, M. Kando, S. V. Bulanov, G. Korn, C. G. R. Geddes, C. B. Schroeder, E. Esarey, and S. S. Bulanov. Multiple colliding laser pulses as a basis for studying high-field high-energy physics. *Physical Review A*, 100(6), 2019.

[138] N. Zaïm, A. Sainte-Marie, L. Fedeli, P. Bartoli, A. Huebl, A. Leblanc, J.-L. Vay, and H. Vincenti. Light-Matter Interaction near the Schwinger Limit Using Tightly Focused Doppler-Boosted Lasers. *Phys. Rev. Lett.*, 132(17):175002, Apr 2024.

Appendix A

Derivation of Linearly-Chirped Gaussian Pulse

Fourier Transform of a Linearly-Chirped Gaussian Pulse

David J. Gibson

March 17, 2006

A linearly-chirped electric field has a frequency that changes linearly with time

$$\omega(t) = \omega_0 + \frac{d\omega}{dt}t = \omega_0 + bt$$

A Gaussian pulse with a frequency chirp can therefore be represented by

$$E(t) = E_0 e^{-at^2} e^{-i\omega(t)t} = E_0 e^{-at^2 - i(\omega_0 + bt)t} = E_0 e^{-(a+ib)t^2 - i\omega_0 t}$$

with a corresponding intensity of

$$I(t) = E(t)E^*(t) = \left(E_0 e^{-(a+ib)t^2 - i\omega_0 t}\right)\left(E_0 e^{-(a-ib)t^2 + i\omega_0 t}\right) = E_0^2 e^{-2at^2}$$

To find the spectrum of this pulse we take the Fourier transform, defined as

$$\tilde{f}(\omega) = \mathcal{F}[f(t)] \equiv \frac{1}{\sqrt{2\pi}} \int_{-\infty}^{\infty} f(t) e^{i\omega t}\, dt$$

Plugging in the electric field above,

$$\begin{aligned}\tilde{E}(\omega) &= \frac{1}{\sqrt{2\pi}} \int_{-\infty}^{\infty} E_0 e^{-(a+ib)t^2 - i\omega_0 t} e^{i\omega t}\, dt \\ &= \frac{1}{\sqrt{2\pi}} \int_{-\infty}^{\infty} E_0 e^{-[(a+ib)t^2 - i(\omega-\omega_0)t]}\, dt\end{aligned}$$

To solve this integral, we can complete the square in the argument of the exponent:

$$(\alpha t + \beta)^2 = \alpha^2 t^2 + 2\alpha\beta t + \beta^2 = (a+ib)t^2 - i(\omega - \omega_0)t + \beta^2$$

Since the is to be true for all t, we can equate the coefficients

$$\begin{aligned}\alpha^2 = a + ib \rightarrow \alpha &= \sqrt{a+ib} \\ 2\alpha\beta = -i(\omega - \omega_0) \rightarrow \beta &= -\frac{i(\omega-\omega_0)}{2\alpha} = -\frac{i(\omega-\omega_0)}{2\sqrt{a+ib}}\end{aligned}$$

and then rewrite the integrand

$$\begin{aligned}\tilde{E}(\omega) &= \frac{1}{\sqrt{2\pi}} \int_{-\infty}^{\infty} E_0 e^{-[(a+ib)t^2 - i(\omega-\omega_0)t + \beta^2 - \beta^2]}\, dt \\ &= \frac{1}{\sqrt{2\pi}} \int_{-\infty}^{\infty} E_0 e^{-\left[(a+ib)t^2 - i(\omega-\omega_0)t + (-\frac{i(\omega-\omega_0)}{2\sqrt{a+ib}})^2 - (-\frac{i(\omega-\omega_0)}{2\sqrt{a+ib}})^2\right]}\, dt \\ &= \frac{1}{\sqrt{2\pi}} \int_{-\infty}^{\infty} E_0 e^{-\left(\sqrt{a+ib}\,t - \frac{i(\omega-\omega_0)}{2\sqrt{a+ib}}\right)^2} e^{\frac{-(\omega-\omega_0)^2}{4(a+ib)}}\, dt \\ &= \frac{1}{\sqrt{2\pi}} E_0 e^{\frac{-(\omega-\omega_0)^2}{4(a+ib)}} \int_{-\infty}^{\infty} e^{-\left(\sqrt{a+ib}\,t - \frac{i(\omega-\omega_0)}{2\sqrt{a+ib}}\right)^2}\, dt\end{aligned}$$

Now, we change variables

$$u \equiv \sqrt{a+ib}\,t - \frac{i(\omega-\omega_0)}{2\sqrt{a+ib}}$$
$$\frac{du}{dt} = \sqrt{a+ib}$$

So we have

$$\tilde{E}(\omega) = \frac{1}{\sqrt{2\pi}} E_0 e^{\frac{-(\omega-\omega_0)^2}{4(a+ib)}} \int_{-\infty-\Im[\frac{i(\omega-\omega_0)}{2\sqrt{a+ib}}]}^{\infty-\Im[\frac{i(\omega-\omega_0)}{2\sqrt{a+ib}}]} e^{-u^2}\,\frac{du}{\sqrt{a+ib}}$$

which is a complex integral over the line $\Im[u] = -\Re\left[\frac{(\omega-\omega_0)}{2\sqrt{a+ib}}\right]$. Because the integrand, e^{-u^2}, is everywhere analytic, we can use Cauchy's Theorem to move the integral to the real axis. Cauchy's Theorem states that the integral of a complex function that is analytic in the domain D over the piecewise-smooth closed contour C in D is 0:

$$\oint_c f(z)\,dz = 0$$

so in our case, tracing out a box,

$$\oint_c e^{-u^2}\,du = \int_{-p}^{p} e^{-u^2}\,du + \int_{p}^{p+iq} e^{-u^2}\,du + \int_{p+iq}^{-p+iq} e^{-u^2}\,du + \int_{-p+iq}^{-p} e^{-u^2}\,du = 0$$

Looking at the integrals over the line $\Re[u] = p$, we can make the substitution

$$u = p + ix$$
$$\frac{du}{dx} = i$$

and so the integral becomes

$$\int_{p}^{p+iq} e^{-u^2}\,du = \int_0^q ie^{-(p+ix)^2}\,dx = i\int_0^q e^{-p^2}e^{-2ipx}e^{x^2}\,dx$$

taking the limit as p goes to infinity of the integrand,

$$\lim_{p\to\infty} e^{-p^2}e^{-2ipx}e^{x^2} = 0$$

because the second and third terms are finite, and the first term goes to zero. Because the integrand goes to zero, we know

$$\lim_{p\to\infty}\int_{p}^{p+iq} e^{-u^2}\,du = 0$$

with a similar result for the line $\Re[u] = -p$. Now our contour integral becomes

$$\begin{aligned} 0 &= \lim_{p\to\infty}\left(\int_{-p}^{p} e^{-u^2}\,du + \int_{p}^{p+iq} e^{-u^2}\,du + \int_{p+iq}^{-p+iq} e^{-u^2}\,du + \int_{-p+iq}^{-p} e^{-u^2}\,du\right) \\ &= \int_{-\infty}^{\infty} e^{-u^2}\,du + \int_{\infty+iq}^{-\infty+iq} e^{-u^2}\,du \\ \int_{-\infty}^{\infty} e^{-u^2}\,du &= \int_{-\infty+iq}^{\infty+iq} e^{-u^2}\,du \end{aligned}$$

and so we can rewrite our electric field spectrum as an integral on the real axis

$$\tilde{E}(\omega) = \frac{1}{\sqrt{2\pi}\sqrt{a+ib}} E_0 e^{\frac{-(\omega-\omega_0)^2}{4(a+ib)}} \int_{-\infty}^{\infty} e^{-u^2}\,du$$

What remains now is to evaluate the integral. We start with

$$\begin{aligned}\int_{-\infty}^{\infty} e^{-x^2}\,dx &= \sqrt{\int_{-\infty}^{\infty} e^{-x^2}\,dx \int_{-\infty}^{\infty} e^{-x^2}\,dx} \\ &= \sqrt{\int_{-\infty}^{\infty} e^{-x^2}\,dx \int_{-\infty}^{\infty} e^{-y^2}\,dy} \\ &= \sqrt{\int_{-\infty}^{\infty}\int_{-\infty}^{\infty} e^{-(x^2+y^2)}\,dx\,dy}\end{aligned}$$

and change to polar coordinates (r, θ)

$$\begin{aligned}\int_{-\infty}^{\infty} e^{-x^2}\,dx &= \sqrt{\int_0^{2\pi}\int_0^{\infty} e^{-r^2} r\,dr\,d\theta} \\ &= \sqrt{2\pi \int_0^{\infty} e^{-r^2} r\,dr} \\ &= \sqrt{2\pi\,\frac{e^{-r^2}}{-2}\Big|_0^{\infty}} = \sqrt{2\pi\left(\frac{1}{2}\right)} \\ &= \sqrt{\pi}\end{aligned}$$

And so finally the electric field spectrum is

$$\tilde{E}(\omega) = \frac{1}{\sqrt{2}\sqrt{a+ib}} E_0 e^{\frac{-(\omega-\omega_0)^2}{4(a+ib)}}$$

and the spectral intensity is

$$\begin{aligned}I(\omega) = \tilde{E}(\omega)\tilde{E}^*(\omega) &= \left(\frac{1}{\sqrt{2}\sqrt{a+ib}} E_0 e^{\frac{-(\omega-\omega_0)^2}{4(a+ib)}}\right)\left(\frac{1}{\sqrt{2}\sqrt{a-ib}} E_0 e^{\frac{-(\omega-\omega_0)^2}{4(a-ib)}}\right) \\ &= \frac{1}{2\sqrt{a^2+b^2}} E_0^2 e^{\frac{-(\omega-\omega_0)^2}{4(a+ib)} + \frac{-(\omega-\omega_0)^2}{4(a-ib)}} \\ &= \frac{1}{2\sqrt{a^2+b^2}} E_0^2 e^{\frac{-a(\omega-\omega_0)^2}{2(a^2+b^2)}}\end{aligned}$$

We can write the FWHM pulse length and spectrum for these Gaussian intensities:

$$e^{-\rho\,\frac{\Delta x}{2}^2} = \frac{1}{2} \rightarrow \Delta x = 2\sqrt{\frac{\ln 2}{\rho}}$$

and for our gaussians

$$\rho_{time} = 2a \qquad\qquad \rho_{freq} = \frac{a}{2(a^2+b^2)}$$

and therefore

$$\Delta t_{FWHM} = \sqrt{\frac{2\ln 2}{a}} \qquad \Delta\omega_{FWHM} = 2\sqrt{2\ln 2}\sqrt{a\left[1+\left(\tfrac{b}{a}\right)^2\right]} \qquad \Delta\nu_{FWHM} = \frac{\sqrt{2\ln 2}}{\pi}\sqrt{a\left[1+\left(\tfrac{b}{a}\right)^2\right]}$$